



# 6G

Next G Alliance Report:  
**Channel Measurements and  
Modeling for Joint/Integrated  
Communication and Sensing,  
as well as 7-24 GHz  
Communication**

As a leading technology and solutions development organization, the Alliance for Telecommunications Industry Solutions (ATIS) brings together the top global ICT companies to advance the industry's business priorities. ATIS' 150 member companies are currently working to address network reliability, 5G, robocall mitigation, smart cities, artificial intelligence (AI)-enabled networks, distributed ledger/blockchain technology, cybersecurity, IoT, emergency services, quality of service, billing support, operations and much more. These priorities follow a fast-track development lifecycle from design and innovation through standards, specifications, requirements, business use cases, software toolkits, open-source solutions, and interoperability testing.

ATIS is accredited by the American National Standards Institute (ANSI). ATIS is the North American Organizational Partner for the 3rd Generation Partnership Project (3GPP), a founding Partner of the oneM2M global initiative, a member of the International Telecommunication Union (ITU), as well as a member of the Inter-American Telecommunication Commission (CITEL).

For more information, visit [www.atis.org](http://www.atis.org). Follow ATIS on [Twitter](#) and on [LinkedIn](#).

The ATIS 'Next G Alliance' is an initiative to advance North American wireless technology leadership over the next decade through private-sector-led efforts. With a strong emphasis on technology commercialization, the work will encompass the full lifecycle of research and development, manufacturing, standardization, and market readiness.

TABLE  
OF  
CONTENTS

	<b>Executive Summary</b>	<b>5</b>
<b>1.</b>	<b>Introduction</b>	<b>7</b>
1.1.	New Use Cases	7
1.2.	Novel Spectrum for 6G	8
<b>2.</b>	<b>Background on Existing Channel Models</b>	<b>9</b>
2.1.	3GPP TR 38.901	9
2.2.	COST 2100	10
2.3.	IEEE 802.11 and Sensing Models	11
2.4.	Ray Tracing Channel Models	11
2.5.	Channel Model Requirements from Sensing Perspective	11
2.6.	What Has Worked in 3GPP Models	12
2.7.	What May Be Missing	12
<b>3.</b>	<b>Communication Channel in New Bands:</b>	<b>16</b>
3.1.	Communication Channel Model at 7 to 24 GHz	16
3.1.1.	Description of Channel Sounding Systems	16
3.1.1.1.	Keysight Channel Sounder System Description	16
3.1.1.2.	Anritsu Channel Sounder System Description	18
3.1.1.3.	AT&T Channel Sounder System Description	19
3.1.2.	Penetration Loss Measurements for Various Materials	20
3.1.3.	Indoor Measurements	22
3.1.3.1.	Measurement in the Smart Production Lab	22
3.1.3.2.	Measurement in the Production Factory	24
3.1.3.3.	Indoor Office Measurements at 15 GHz	27
3.1.4.	Outdoor Measurements	27
3.1.4.1.	University Campus Courtyard	27
3.1.4.2.	Industry Campus	28
3.1.5.	Directional Measurements	29
3.1.6.	Channel Model for Path Gain and Delay Spread, in Comparison to Existing Models of 38.901	30
3.1.6.1.	Path Gain and its Frequency Dependence in a Factory	30
3.1.6.2.	RMS Delay Spread in a Factory	34
3.1.6.3.	Courtyard Path Gain	35
3.1.6.4.	RMS Delay Spread in a Courtyard	37
3.1.6.5.	Conclusions	38
3.1.7.	Analysis and Channel Modeling for Indoor Office Environment at 15 GHz	38
3.2.	Communication Channel Model for D-Band & Above	43

TABLE  
OF  
CONTENTS

<b>4.</b>	<b>Target Modeling</b>	<b>44</b>
4.1.	Channel Measurements	45
4.1.1.	NIST Channel Sounder	45
4.1.2.	AT&T Channel Sounder	46
4.1.3.	Measurement Campaigns	48
4.2.	Target Models	50
4.2.1.	Geometry of Target Links	51
4.2.2.	Single-ray Model	52
4.2.2.1.	Fading Single-ray Target Model	55
4.2.3.	Stochastic Cluster Model	56
4.2.3.1.	Model Parameters for Stochastic Cluster Target Model	58
4.2.4.	Quasi-Deterministic Cluster Model	62
4.2.4.1.	Deterministic Model Component	62
4.2.4.2.	Stochastic Model Component	63
4.2.4.3.	Quasi-Deterministic Target Channel Realization	64
4.2.5.	AT&T Target Measurements and RCS Models	66
4.3.	Measurement of a Pedestrian Target	71
<b>5.</b>	<b>Background Clutter</b>	<b>77</b>
5.1.	Indoor Monostatic Background Clutter	77
5.1.1.	Environment Definition	77
5.1.2.	Measurement Description	77
5.1.3.	Average Backscattered Power	78
5.1.4.	Observed Azimuth Variation Statistics	81
5.1.5.	Clutter Backscatter Model	83
5.1.6.	Delay-Azimuth Clutter Backscatter Model	84
5.2.	Other Environments and Sensing Arrangements	86
<b>6.</b>	<b>Sensing Channel Model Enhancements</b>	<b>87</b>
6.1.	Sensing Target Models	87
6.1.1.	Option 1 – Single-Point Single-Ray Model	87
6.1.2.	Option 2 – Single-Point Multiple-Ray Model	87
6.1.3.	Option 3 – Multiple-Point Model	87
6.2.	Sensing Environment Models	87
<b>7.</b>	<b>Conclusions</b>	<b>88</b>
<b>8</b>	<b>Acronyms &amp; Abbreviations</b>	<b>89</b>
<b>9</b>	<b>References</b>	<b>91</b>

**Overview, Objectives, and Key Deliverables**

This report's objective is to study communication channels and Joint Communication and Sensing (JCAS)/Integrated Sensing and Communication (ISAC) channel models covering mid-bands, mmWave, and sub-THz spectrum bands. The study highlights modifications to channel models developed in the 3GPP TR 38.901 [2] for 7-24 GHz based on new measurements. The new modifications also would be used to develop new channel models between 100 GHz – 300 GHz based on new measurements when they become available.

New mid-band spectrum between 7 and 24 GHz has been considered to play a key role in 6G deployment. In principle, the 3GPP channel model specified in the TR 38.901 covers the frequency range from 0.7 GHz to 100 GHz. However, the majority of measurements used to validate these models were conducted for FR1 and FR2 because not much was available for 7-24 GHz. Therefore, there is a need to vigorously examine how different the 7-24 GHz band propagation channel modeling compares to FR1 (cellular) and FR2 (mmWave) bands based on new measurements and how the TR 38.901 channel model needs to be modified or enhanced based on these measurements.

JCAS/ISAC is one of the key new features for 6G where existing telecommunication infrastructure is also used for RF sensing without requiring an active transmission from the targets to be sensed. Recently, interest has begun to develop on the reuse of communications infrastructure to perform wireless sensing in a variety of novel use cases and scenarios (e.g., 3GPP TR 22.837 SA1 use case [1]). These use cases may offer promising opportunities for 3GPP at scale, but the 3GPP Radio Access Network (RAN) currently lacks the tools to adequately assess the performance of possible solutions for these use cases. Channel models will also depend on the target use cases and environment for sensing.

Such radio wave-based sensing, either in monostatic or bi-static settings, requires proper channel modeling to evaluate and benchmark sensing performance. Note that channel modeling for quasi-monostatic settings, where the Transmitter (Tx) and Receiver (Rx) antennas are slightly separated but still appear to be at the same location as viewed from the target, shall be processed in the same way as in monostatic settings. Channel modeling for wireless communications has so far focused solely on communication aspects. For example, the channel model developed by RAN1 for NR in TR 38.901 was designed with the goal of assessing mobile communications performance, but it lacks several features that would be necessary to assess systems performing communications and sensing operations jointly. TR 38.901 [2] characterizes the radio propagation channel primarily as correlated clusters of multipath components between the gNodeB (gNB) and its target UE. The primary use of this channel model is to characterize the effect of signal propagation on link quality between the gNB and the UE. In sensing applications, however, it is necessary to further characterize these clusters with consideration to their link quality in identifying a target that lies somewhere between the Tx and the Rx. Therefore, new efforts on JCAS/ISAC modeling are needed.

In early 2023, the NGA's 6G National Roadmap Working Group (6G NRWG) created a "small group" to conduct a set of measurement campaigns covering frequencies from 2.5 GHz through 30 GHz for both indoor (e.g., smart production lab, office with corridor, conference room, cafeteria, etc.) and outdoor (e.g., courtyard, etc.). Communication channel behavior in the 7-24 GHz band was examined based on new measurements to assess accuracy of the existing standard propagation model. Based on measurements in factory and outside courtyard conducted by Keysight and Anritsu in the current report, it is found that the measured channels (indoor factory and short range outdoor, <100 m) are consistent with the TR 38.901 propagation model recommendations. Thus change might be unnecessary for these channels. Conclusions about other channel models are pending based on more measurements from member companies.

Sensing channel models are developed to allow simulation of detection and characterization of target signals in the presence of clutter. Target types include humans, vehicles, drones, and robot arms. Both monostatic and bi-static sensing measurements have been reported. Scattered power is given by the radar equation. Target Radar Cross-Section (RCS) is described statistically, with parameters extracted from measurements for human and vehicle targets.



Additional parameters such as target delay and angle spreads were also deduced from measurements to allow high-resolution simulation needed for target behavior characterization, such as human gesture recognition. Based on sensing use cases, target models with different complexity (sing-ray, single-point multiple-ray, or multiple-point) could be adopted. A statistical model for clutter backscatter is developed for monostatic sensing indoors, with parameters deduced from measurements, to allow simulation of target detection, localization, and characterization in the presence of clutter.

These measurements and modeling are intended to provide a better empirical basis for 3GPP development of both sensing and communication propagation channels as part of their ongoing studies in Rel-19.

# 1 INTRODUCTION

## NEW USE CASES AND NEW SPECTRUM FOR 6G

### 1.1. New Use Cases

6G will be no exception to the intent of each new generation of high-mobility wireless communications to enable enhanced or novel use cases in social, government, and industrial contexts. Although anticipating the “killer app” has been a futile exercise for each new generation, a practical exploration of what 6G can enable is underway. The Next G Alliance’s *6G Roadmap for Vertical Industries* [28] provides a clear summary of possibilities in the areas of Agriculture, Transportation, Entertainment, Healthcare, Education, Industrial, Mining, Public Safety, and Smart Cities. The NGA also presented nine use cases at the 3GPP SA1 workshop held May 8-9, 2024, in Rotterdam [17] Using mobile radio for simultaneous sensing and communications provides JCAS (also known as ISAC) which adds a dimension to enhanced and novel use cases across this range.

With no attempt to be comprehensive, it is best to consider the possibilities of JCAS with only the following examples:

- > **Automated Vehicles:** Most Advanced Driver Assistance Systems (ADAS) systems have a range of sophisticated sensors using LIDAR, RADAR, video, etc. Enabling the ubiquitous cellular connection adds multiple sensing facets both from the gNB and from the vehicles. The possibility of using wavelengths from 0.5m (600 MHz) to perhaps as short as 2 mm (150 GHz) expands the possibilities of sensing the environment from object detection to perhaps object identification, given different reflection and absorption of materials across this spectrum. To fully utilize this, it is necessary to have the information from the communications system be “fused” with that of the other sensors in the vehicle to plug information gaps in the environment.
- > **Healthcare:** Many apps leverage sensors already built into smartphones and wearables. These include blood sugar measurement, breath analysis, retinal scans, body temperature, pulse, and physical behavior. Again, the range of spectrum listed above has the potential of adding radio-based sensing on top of the IR-, visual-, and accelerometer-based sensing already available. New radio technologies and additional spectra in communications will expand the health care use cases through a mix of location- and material-based sensing.
- > **Entertainment:** It is perhaps easy to foresee the more ubiquitous use of XR capabilities in entertainment with the smartphone form factor evolving to something looking more like goggles or even spectacles. Leveraging the range of spectrum described above for shorter distances to determine the precise location of the user and fellow users and to sense gestures and body language will change the face of mobile gaming.
- > **Smart Industry:** The environment awareness brought by JCAS can be utilized for range of use cases in the context of automated and smart industry, ranging from high-accuracy positioning and tracking of targets/vehicles in a factory hall [1, UC 5.32], trajectory tracing, and collision avoidance between Automated Guided Vehicles (AGVs)/Autonomous Mobile Robots (AMRs) with human or non-human targets [1, UC 5.32].

- > **Smart City:** The almost ubiquitous presence of cellular deployment in the cities can facilitate valuable sensing use cases, improving public safety and situational awareness, particularly in densely populated areas. This includes, among others, intrusion detection in a restricted public area (e.g., by a UAV, animal, human [1, 5.13, 5.22]), road safety (road intrusion or anomaly detection [1, UCs 5.2]), traffic monitoring (e.g., [1, UC 5.14]), environment monitoring (e.g., rainfall monitoring [1, UC. 5.2]), crowd density monitoring, etc.

More detailed use cases discussion can be found in Section 4 of the *Distributed Sensing and Communications* white paper [29].

## 1.2. Novel Spectrum for 6G

Every new generation of wireless technology uses the spectrum introduced for and used by the previous generation. 6G will therefore leverage 5G spectrum, which ranges from 450 MHz up to as high as 71 GHz. This means that some form of additional sensing could be applied to any of the bands already specified by 3GPP. Given that RF sensing in cellular communications for applications other than enabling/improving the communications link itself is a novel concept, studies are under way across this spectrum. The analysis and understanding of these radio channels is mature for those already used in 3GPP-based systems. But it is interesting to note that the channel models for some of these bands for the sake of sensing have had less analysis than those for communications. Thus there is a question about whether the standardized models are adequate for adding more sensing applications to these bands.

More important are parts of the spectrum that heretofore have, for all practical purposes, been unused for terrestrial mobile communications. Of the more popular under consideration for 6G are the following:

- > 7.125-24.25 GHz (often referred to as “upper midband”)
- > 110-330 GHz sometimes divided into subsections of 110-170 GHz, 140-220 GHz, and 220-330 GHz (all being a subset of “subTHz”)

Technical and policy considerations regarding these bands are explored at length in the Next G Alliance’s *6G Spectrum Considerations* report [30].

A full understanding of the radio channels related to sensing is perhaps lacking in some frequencies used in 5G today. Nevertheless, it is important to consider that channel measurements and modeling for the sake of neither communications nor JCAS has been done in any comprehensive manner for the novel frequency ranges described above. Standardized models for parts of the 7-24 GHz range have been extrapolated from research done on lower frequencies (e.g., 3GPP TR 38.901), but experimental data and analysis are lacking.

# 2 BACKGROUND ON EXISTING CHANNEL MODELS

Several different channel models are used in the evaluation of communication systems. These channel models can be broadly classified into deterministic and stochastic. Map-based hybrid models are composed of a deterministic component (usually generated by the Ray Tracing (RT) method when a digital map of the environment is available) and a stochastic component. This is useful if system performance is desired to be evaluated or predicted with the use of digital maps to account for the impacts from environmental structures and materials. 3GPP TR 38.901 [2] has developed both a stochastic channel model and a map-based hybrid channel model for communication system performance for frequency bands over the range of 0.5-100 GHz. In addition to 3GPP modeling work, other channel models such as from the Mobile and Wireless Communications Enablers for the Twenty-Two Information Society (METIS), Millimetre-Wave Evolution for Backhaul and Access (MiWEBA), ITU-R M, COST2100, IEEE 802.11, and NYU WIRELESS are also available.

The RT methods are based on the geometrical theory of diffraction, the uniform theory of diffraction, and the field intensity superposition principle. The RT method's shortcomings include challenges in accuracy (especially in the mixture of diffraction and diffusion), a need for accurate description of the scattering environment, and potentially high computation complexity. In addition, there is no canonical implementation of a ray tracer. Different implementations will therefore not give the exact same result necessary for a faithful evaluation across multiple interested parties.

With respect to sensing, the important distinction is need for geometrical channel models. For sensing, the channel needs an underlying geometry because it is the geometry, or parts of it, that needs to be sensed. Geometrical channel models are generally deterministic given a geometry, but can be made stochastic by, for example, adding random gains (e.g., Swerling target models to describe the fluctuations in radar cross-section), direction of arrival and departures, or by super-positioning a stochastic model such as the 3GPP TR 38.901 on top of a geometric model.

## 2.1. 3GPP TR 38.901

3GPP specified channel models for communication link simulations in 3GPP TR 38.901 [2]. TR 38.901 has a geometry-based stochastic channel model that provides large degree of freedom for modelling different deployments and use cases. The channel model is parameterized for six key scenarios: rural macrocell, urban microcell street canyon, urban macrocell, indoor mixed office, indoor open office, and indoor factory.

The 3GPP 38.901 channel model is suitable for frequencies from 0.5 GHz to 100 GHz and can be used for both link level and system level simulations. It models radio propagation aspects such as blocking and atmospheric attenuation. The supported bandwidth is at most 10% of the center frequency, up to 2 GHz. Mobility of either one or both link ends is supported with options for spatial consistency. Additionally, the model supports large antenna arrays based on far field

assumption and a stationary channel over the size of the array. A spatial consistency procedure, as described in Section 7.6.3.2 [2] for macro-scale mobility, can be applied to ensure that the random variables generated in a drop-based simulator are spatially consistent (i.e., correlated if close to each other).

Section 7.5 of [2] describes the stepwise procedure for generating channels between Base Stations (BSs) and UEs in a set of parameterized scenarios: Urban Macro, Urban Micro, Rural Macro, Indoor Office, and Indoor Factory. Section 7.6 provides a set of optional modeling components. The geometric positions of the BSs, the UEs, and optionally a set of blockers can be provided; everything else is handled via stochastic models and procedures. The 38.901 channel model, developed for communications, is inherently bistatic (BS-UE).

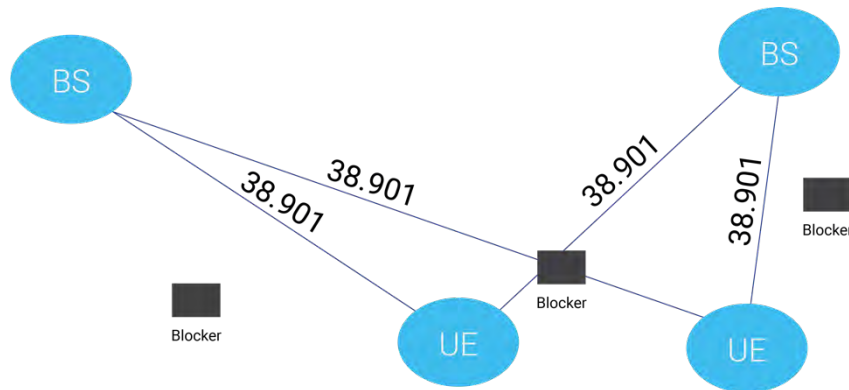


Figure 2.1: Geometrically Positioned Components (BSs, UEs, and optional blockers) in the 38.901 Channel Model. Note that only Line-of-Sight (LOS) paths are shown here, but 38.901 channel model also includes stochastically generated multipath components from different clusters modeling the MIMO channel.

## 2.2. COST 2100

The COST 2100 channel model [27] is a cluster-based channel model developed for the analysis of the communication performance of multi-user MIMO systems. The channel model contains three types of clusters:

- > Single-bounce clusters are parameterized in terms of geometrically coherent xyz coordinates, which enables them to model objects with given locations. These clusters also have an associated diameter, which gives the angular spread, and depth, which gives the delay spread.
- > Local clusters are centered around the Tx or the Rx and enable the modelling of a LOS signal that has a non-zero angular spread and non-zero delay spread. For example, this could model a case where a nearby obstacle such as the body or a car blocks the direct signal, but local scattering still gives a path that resembles a LOS path.
- > Twin clusters are the same type of clusters found in 3GPP TR 38.901 [2].

The single-bounce clusters and the twin clusters have an associated visibility region. The cluster is active and contributes to the channel only when the mobile station (Tx or Rx) is in the associated visibility region. To avoid abrupt changes in the channel when the mobile station moves into a visibility region or out of one, there is a visibility region gain that smoothly varies between zero and one as the mobile station moves in or out of the visibility region.

Clutter can be modelled by placing the different types of clusters in a random way or according to a given setup, where the coordinates of the single-bounce clusters would coincide with objects that cause clutter.

The model does not model Doppler shifts due to movement in the environment, only that due to movement of the Tx or Rx. Nor does it model blockage, nor scattering properties of objects, other than through the visibility regions.

### **2.3. IEEE 802.11 and Sensing Models**

The channel models proposed for Wireless Local Area Networks (WLAN) Sensing systems in sub-7 GHz and 60 GHz bands, where the main use case is detection of moving targets, rely on ray tracing to take into account non-stationarity characteristics of the propagation channel arising from the moving targets [6]. The channel model allows for generating a channel realization that includes spatial, temporal, and amplitude characteristics of all rays in that realization. The spatial characteristics of rays include azimuth and elevation angles for both a Tx and a Rx.

To model the clutter impact and irregular movements of the targets, a Data Driven Hybrid Channel (DDHC) model is also proposed in [6]. This model uses ray tracing to model the target-related rays, and an autoregressive statistical method is used to model the target-unrelated rays. The target-unrelated rays are defined as the rays reflected from fixed objects and perturbed scatterers, and the target-related rays are defined as the rays reflected from the moving targets. By using the real dataset collected from experiments, the fine-tuned DDHC Model can be obtained to better approximate the real channel model in a specific scenario.

### **2.4. Ray Tracing Channel Models**

Some ray-tracing-based channel models have been suggested for sensing evaluations. In [3], National Institute of Standards and Technology (NIST) presents a ray-tracing based model that is termed as a quasi-deterministic ray-tracing channel. The quasi-deterministic channel is a mix of rays obtained from ray tracing of specular reflections and rays obtained from a point scatterer model. In [4], the Opal simulator that makes use of the NVIDIA Optix RT Engine is presented, which is a simplified ray-tracing model that only considers specular reflections.

The source-code of these ray-tracing channels is openly available online, as opposed to proprietary ray tracers. Another openly accessible ray tracer is available at [5], where ray tracing can be performed using a common software on a server for all registered users.

### **2.5. Channel Model Requirements from Sensing Perspective**

From a sensing point of view, the channel model should allow capturing of features that can enable the JCAS system to distinguish different objects. These features may include:

- > The object's scattering properties.
- > The time delay in signal reception due to the position of the object relative to the Tx and Rx.
- > The Doppler shift created by the radial velocity of the object.
- > Scintillation due to movement in parts of the target.

In addition, most use-cases also require the modelling of clutter, which is unwanted echoes created by the surrounding environment. In many applications, especially in multistate sensing scenarios, blockage of signal paths and LOS probabilities are important to model to account for outages in a set of sensing nodes.

Specular reflections on, for example, walls and the ground might also be important to model because specular reflections tend to be among the strongest signal paths in the channel. Specular reflections on physical walls with actual geometric positions should be modelled, for example, when analyzing radio based Simultaneous Localization and Mapping (SLAM) algorithms. A priori knowledge of the environment might also enable the use of reflections to sense objects in Non-Line-of-Sight (NLOS). Furthermore, ghost targets (i.e., reflections of actual targets) might be necessary to consider in some use cases.

Finally, the channel model should maintain the JCAS nature and should allow capture of the impact of sensing on communication KPIs such as coverage, capacity, user experience statistics, energy efficiency, etc.

## **2.6. What Has Worked in 3GPP Models**

The channel modeling methodologies of 3GPP are well accepted for both link- and system-level simulation of various use cases and deployment scenarios. Both simpler stochastic channel models and more complicated map-based modeling are available. Other than an acceptable level of model accuracy, facilitating an efficient convergence and decision-making on the evaluation of different technologies, within various study items, it provides a successful balance between model accuracy and computational and evaluation complexity. The proposed fast-fading stochastic models treat different aspects of the channel as approximation or non-deterministic, though stochastically consistent models generate a sufficient generalization capability to adjust the channel scenarios to different deployment conditions (e.g., Indoor factory (InF), Indoor office, Urban deployments). It is expected that the same paradigm will continue in view of the expected channel modeling enhancements for sensing, to deliver sufficient model accuracy and consistency for the expected/selected sensing use cases, while delivering a tradeoff between model accuracy, computational complexity, and generalization capability.

## **2.7. What May Be Missing**

The 3GPP channel model is designed for gNB-to-UE communication links and thus lacks the sensing target model aspects. In addition, the channel modeling for sensing targets is dependent on the sensing mode (e.g., monostatic or bistatic).

A drawback with the 3GPP channel model is that there is no geometrical relationship between angle-of-departure and angle-of-arrival for multi-path components (i.e., there is no differentiation between single-bounce and multi-bounce propagation). For communication link evaluations, this is not an issue, but for sensing and mapping use cases, the location of the reflecting object is important. Finally, the model is parameterized for a set of communication scenarios and only links between BSs and UEs are modelled. Hence, monostatic or BS-BS bistatic channels are not modeled, making it unsuitable for some sensing scenarios.

The target modeling requirements are generally dependent on underlying performance requirements and particular use cases. Further study may also be needed to cover the paradigm of immersive reality use case where the performance requirements are higher.

The particular missing elements of TR 38.901 can be further observed in view of the potential sensing UCs, and the corresponding channel modeling requirements, against the current state of TR 38.901. In particular, the following aspects can be identified:

- > **Various sensing scenarios support:** Depending on the device that transmits and/or receives sensing signal, mono-static sensing and bi-static sensing scenarios are considered. For mono-static sensing, mono-static gNB sensing and mono-static UE sensing need to be supported. For bi-static sensing, bi-static gNB-to-UE (or UE-to-gNB) sensing, bi-static UE-to-UE sensing and bi-static gNB-to-gNB sensing need to be supported. For these sensing scenarios, Large-Scale Parameters (LSPs) and Small-Scale Parameters (SSPs) are additionally defined for sensing channel generation. Depending on the type of target to be sensed and the use case, the altitude, RCS, LSP/SSP generation method, etc., of the target or device may be different.
- > **LOS/NLOS state determination for sensing channel:** In most radar-based sensing channel modeling, it is assumed that a target exists (i.e., the channel between the target and the sensing device is LOS state). This may be sufficient for evaluating only sensing performance, but to evaluate performance from a system perspective and evaluate integrated sensing and communication performance, an actual channel model, including NLOS between the sensing device and target is needed. The existing distance-dependent LOS/NLOS state decision probability model may be reused (in this case, the distance between the Tx device and the Rx device should be replaced with the distance between the sensing device and the target). Alternatively, based on measurement or channel sounding, we may discuss new models for sensing LOS/NLOS state determination. Additionally, parameters such as delay spread, angular spread, shadowing factor, Pathloss (PL), etc. may be determined differently depending on the LOS/NLOS state.
- > **LSPs for sensing channel:** Delay spread, angular spread, shadowing factor, PL, and Ricean K factor (K) can differ from those of the communication channel. Figure 3.35 shows an example of different angular spread/distribution in communication and sensing channels. In a communication channel, the BS and the UE have different antenna heights. Thus it is desirable to use different angular distributions for Angle of Arrival (AoA) and Angle of Departure (AoD). However, in the case of mono-static sensing, because the Tx and Rx are co-located and their antenna height are the same, the AoA and AoD should have the same distribution.
- > **SSPs for sensing channel:**
  - o **Cluster/Ray modeling for sensing channel:** Deterministic or semi-deterministic Ray/cluster Modeling can be considered. Delay, gain, and echo angle for a direct path toward a sensing target are determined based on the physical location of a sensing target. Delays, gains, and angles for indirect paths toward the sensing target are generated based on a statistical manner based on measurement or sounding results. If the target is located very close to the sensing device, the near-field effect can also be considered. This may be seen as generating channels that include a single bounce toward/from the target and channels that have multi-bounces toward/from the target. If the sensing target creates one or more clusters and multiple rays exist within the one or more clusters, one of the

rays corresponds to a direct path and the rest of the rays correspond to indirect paths. Based on them, a multipath channel can be generated for a sensing target. There is also a need to discuss how to generate the delay and angle of the target-unrelated channel. The channels generated by the surrounding environment or clutter can be distinguished from channels generated by targets. There is a need to further discuss how we can generate clusters/rays generation for mono-static sensing and bi-static sensing. When implementing a cluster for a sensing object, we need to discuss whether to generate a cluster for the sensing object in addition to the existing communication clusters or assign one or more clusters from the generated clusters for communication with the sensing object.

- **Effect of mobility:** The device mobility is already modeled in communication channel modeling, but target mobility also needs to be considered.
- > **RCS consideration:** RCS needs to be characterized for the relevant sensing targets/scenarios.
  - Different sensing targets including human, vehicles, AGV/AMR (smart factory), and human health signals (respiration/heartbeat channel signatures) may have different RCS values.
  - The channel modeling shall support different related deployment scenarios (e.g., RCS characterization for various Tx/Rx position with respect to the sensing target).
- > **Cross-Polarization Ratio (XPR) for sensing channel:**
  - In mono-static sensing, even if the channel between the sensing device and the target is LOS, the channel itself should be modeled for reflected wave. Note that in a communication channel, an infinite XPR value is used for the LOS path (i.e., a diagonal matrix is used for an X-pol channel generation). But in a sensing channel, an XPR value of infinity should not be used for the direct path toward the sensing target, and the mean and variance of XPR may be different from those of communication channel.
  - For bi-static sensing, we may be able to reuse XPR values for communication channels.
- > **Consistency:** Some use cases may require spatial/temporal consistency modeling. For example, let us assume a case where multiple devices cooperate to sense a single target. If the sensing channels of the two devices are generated independently, the cooperative sensing performance may be incorrectly estimated. If two devices are physically close together or a device or a target moves in limited space, their channel generation may also correlate. It is necessary to discuss how we can make a correlation in LSPs and/or SSPs generation between spatial/temporal displacements.
- > **Support of different frequency bands,** for which the modeling is not available in TR22.837 or only available for communication channels:
  - (Sub-)THz band (>100GHz)
  - Verification in FR3 (7-24GHz)

Based on the above discussions, Figure 2.3 illustrates the limitations and example modifications of 38.901 model for sensing.

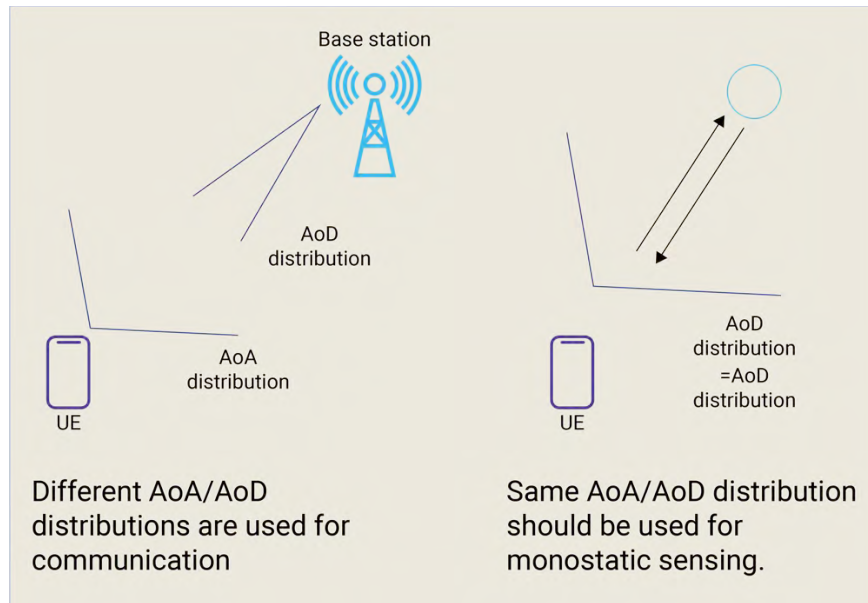


Figure 2.2: Different AoA/AoD Distribution for Communication and Sensing

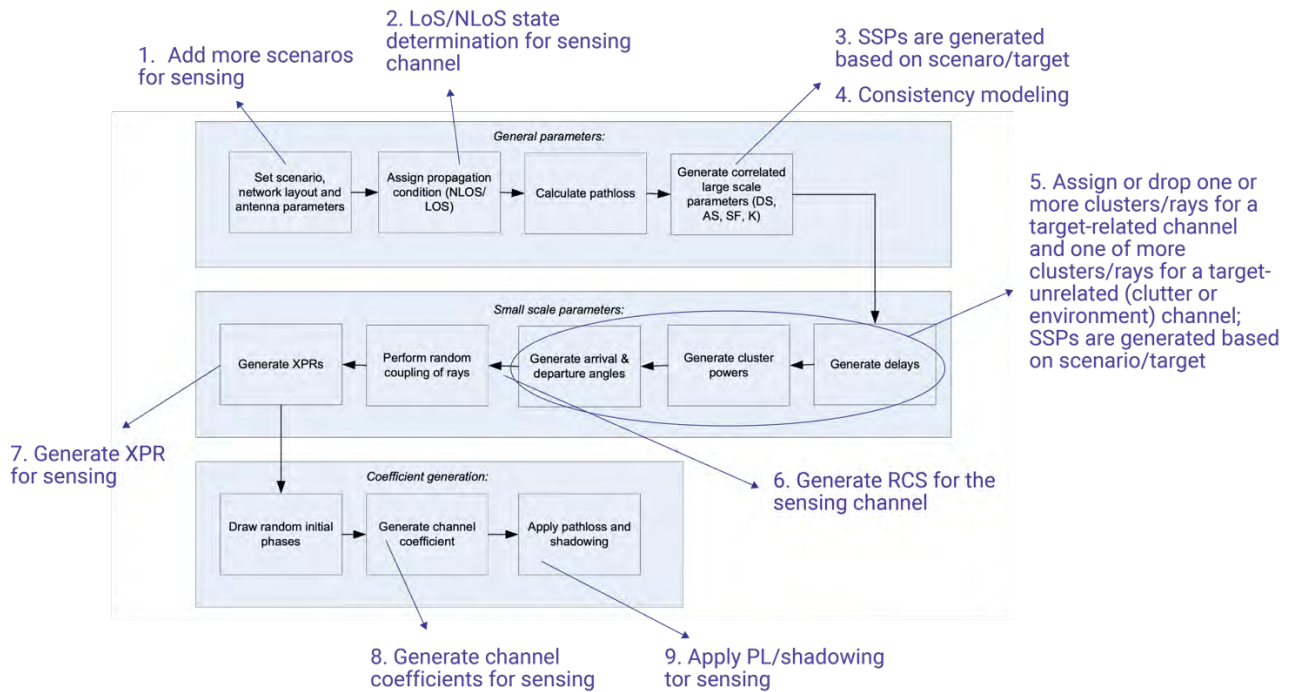


Figure 2.3: Limitations and Example Modifications of TR 38.901 Model for Sensing

# 3 COMMUNICATION CHANNEL IN NEW BANDS:

## 3.1. Communication Channel Model at 7 to 24 GHz

The measurements were collected by Keysight, Anritsu, and AT&T and serve as the basis for channel modeling and recommendations.

### 3.1.1. Description of Channel Sounding Systems

#### 3.1.1.1. Keysight Channel Sounder System Description

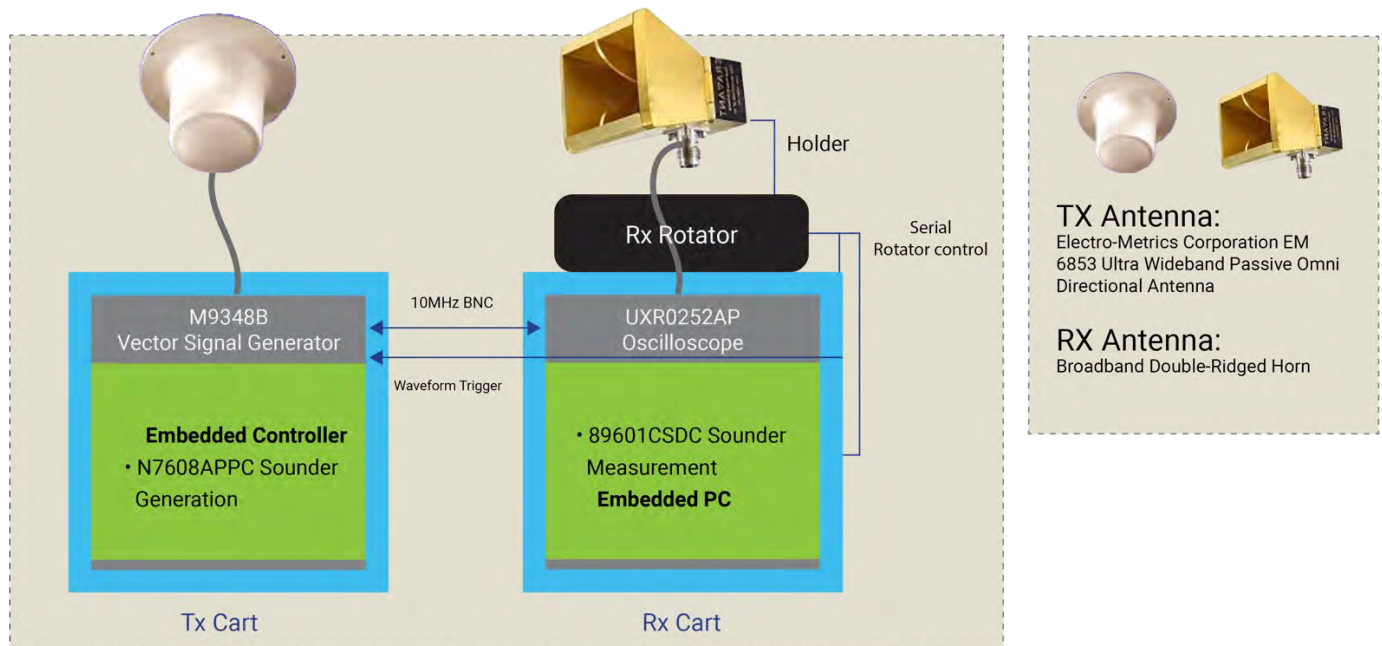


Figure 3.1: Keysight's Sounder Setup

- > Frequencies approved by FCC: 6.75-7.25 GHz, 10-10.5 GHz, 12.75-13.25 GHz
- > Measurement of conference rooms, Keysight cafeteria, and factory floor
- > Calibration was done by normalizing loss at 1m distance

#### Measurement setup

- > Tx antenna frequency range: 300 MHz-40 GHz omnidirectional
- > Rx antenna frequency range: 6-53 GHz
- > M9484B vector signal generator
  - 44 GHz frequency range

- 2 GHz modulation bandwidth
- > UXR0252A oscilloscope
  - 2 channels
  - 256 Gs/s sample rate
  - 100 GHz bandwidth
- > 89600 Vector Signal Analysis (VSA) channel sounding measurement software
  - VSA recording file generated for each rotation of the Rx antenna
    - Data is measured in one-degree steps, triggered to provide absolute propagation time measurements
    - Rx elevation angles from -30 to +30 in 10-degree steps
  - 89600 recording file post processed to generate Channel Impulse Responses (CIR) at each measurement point. Data generated:
    - CIR data: .csv file for all measurements in one recording file
    - VSA spectrogram trace file containing all points in one file (shown in trace B at right)
    - Plots of peak impulse power vs Rx azimuth angle and distance to peak impulse power vs Rx Azimuth
  - CIR data shared with Next G Alliance.
    - Recording files and other data files retained by Keysight but not shared as they require Keysight software to use

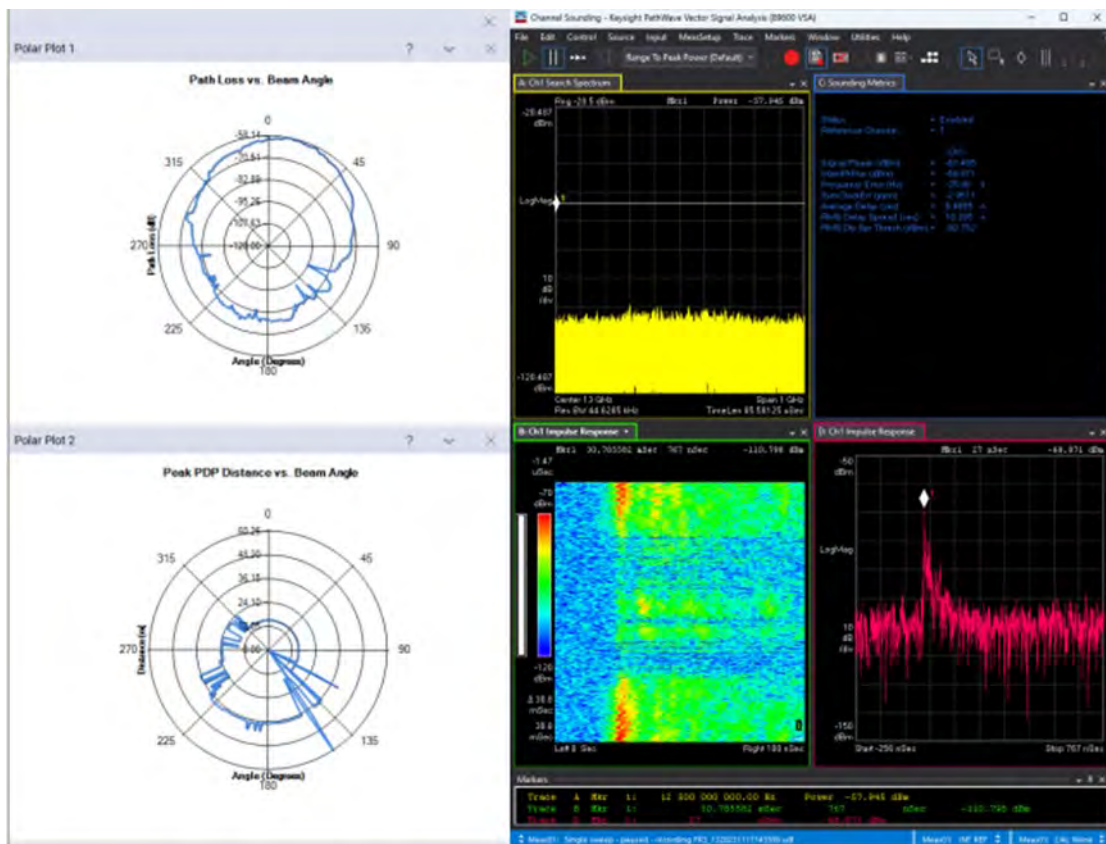


Figure 3.2: Example Channel Impulse Response from Keysight's Sounder

### 3.1.1.2. Anritsu Channel Sounder System Description

This activity was performed using a Vector Network Analyzer (VNA)-based channel sounder. A novel technique here was using a portable and distributed-port VNA (ME7868A) to recover accurate path and phase information. Traditional VNA have Tx and Rx combined in single unit and need RF coax cables running from VNA ports to the antenna, thereby inducing high transmission loss and phase incoherency.

The Anritsu channel sounder consists of distributed VNA using patented technology whereby the VNA's Tx and Rx ports can be separated up to hundreds of meters and still have a high dynamic range. There is no downconversion needed, and phase coherence and accurate magnitude are maintained over large distances, temperatures, and movement. This setup provides absolute time of flight path delay information.

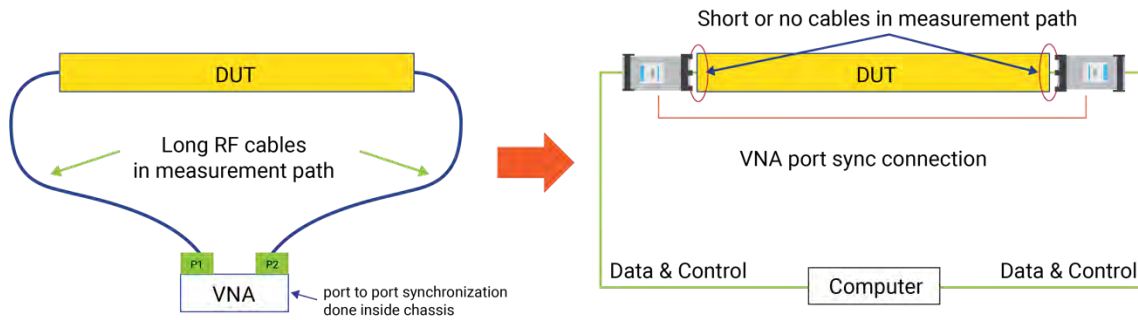


Figure 3.3: Anritsu's Sounder Setup

The Tx and Rx ports can be separated by hundreds of meters. Because of its portability, the two parts of the VNA channel sounder can be separately mounted on movable robot as shown below.

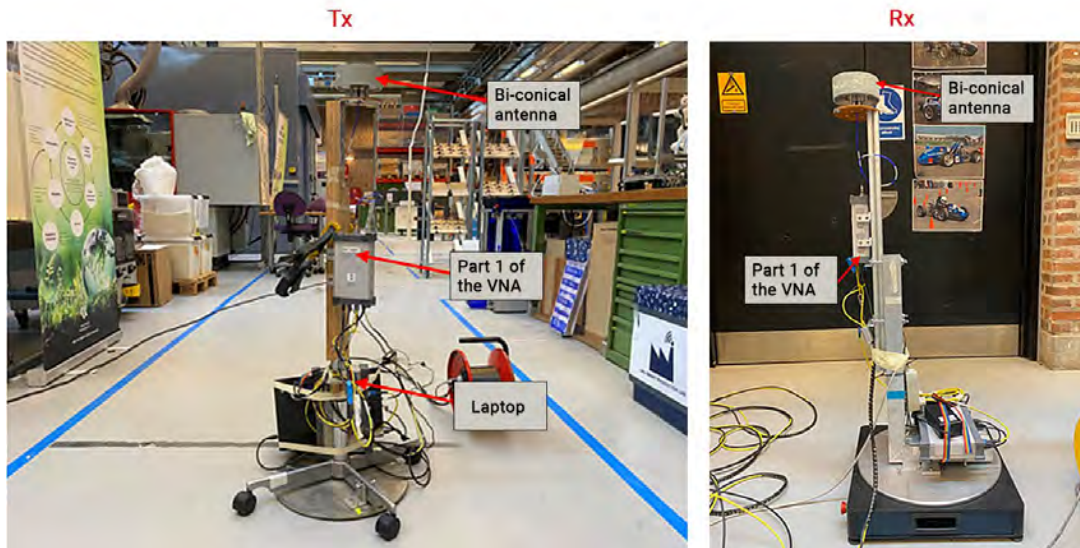


Figure 3.4: The Tx and the Rx of the Sounder

The VNA and cables are calibrated prior to the testing and link budget analysis.

### 3.1.1.3. AT&T Channel Sounder System Description

The channel sounder baseband design is based on National Instrument's Universal Software Radio Peripheral (USRP) x410. The USRP at the channel sounder Tx generates an Orthogonal Frequency-Division Multiplexing (OFDM) baseband signal with 400 MHz bandwidth and carrier spacing of 120 KHz, mixed with a local oscillator frequency of 3.5 GHz, resulting in an Intermediate Frequency (IF) signal with a spectrum between 3.3 GHz and 3.7 GHz. This resultant IF signal is then filtered, upconverted, and amplified to either the 8, 11, or 15 GHz bands.

The channel sounder Rx is equipped with two types of Rxs:

> **An omnidirectional Rx:**

Where the Tx RF signal is captured via a conventional omnidirectional antenna, followed by direct downconversion to the IF frequency. The downconverter has a 45 dB conversion gain and a 2.5 dB Noise Figure (NF).

> **A 360-degree analog beamformed Rx, nicknamed ROACH for Realtime Omnidirectional Array Channel sounder:**

ROACH consists of four dual-pole 8x8-element phased arrays having 13 degrees Half Power Beam Width (HPBW) per beam. The arrays are set up so that each one points to a different 90° sector surrounding the UE. As such, each array is configured so its field of view covers a  $\pm 45^\circ$  in azimuth and  $\pm 26^\circ$  in elevation using a codebook of 30 beams. The RF input is directly downconverted to the IF frequency by array for measurements and data collection. Each array has a dedicated Rx, which allows full scan and measurements of received signal at all 30 beams within 1.25 ms independent of each other. This configuration gives ROACH a  $360^\circ/52^\circ$  (azimuth/elevation) measurement capability to within 1.25 ms.

Both Tx and Rx could be made mobile. Figure 3.5 shows the setup for indoor communication measurements.



Figure 3.5: AT&T's Channel Sounder Setup for Indoor Communication Measurements

### 3.1.2. Penetration Loss Measurements for Various Materials

Keysight performed material penetration loss measurements using the setup shown in Figure 3.6. A list of typical construction materials is selected, whose type and dimension are summarized in Table 3.1, and the measured penetration loss is reported in Figure 3.7.

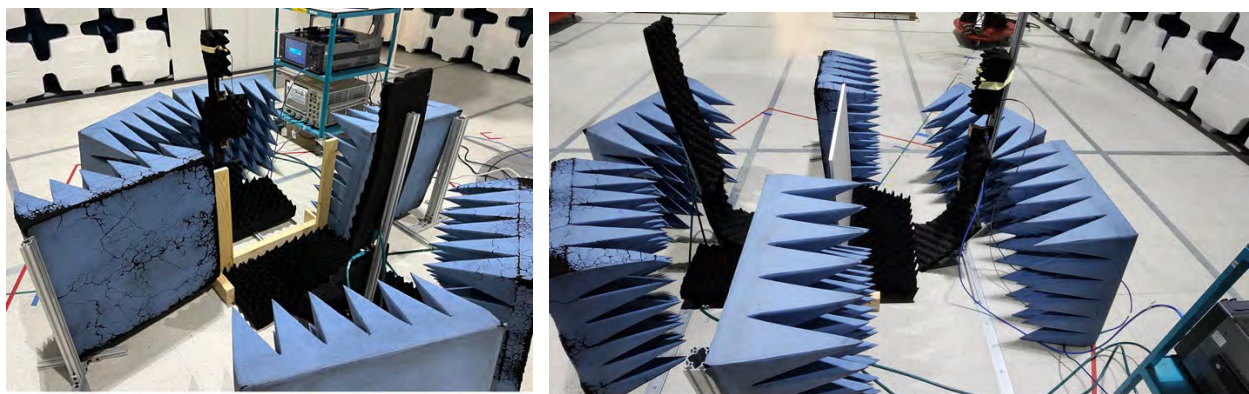


Figure 3.6: Penetration Loss Measurement Setup by Keysight

Table 3.1: Summary of Material for Penetration Loss Measurement

Material	Thickness (inches)	Thickness (mm)
Drywall	31/64	12.3
Plywood	25/32	19.8
Treated Plywood	3/4	19.05
Particle Board	41/64	16.27
Strand Board	35/64	13.89
Foam Insulation Board	1 – 3/63	26.6
Butcher Block	1- 17/32	38.89
Aluminum Sheet	5/64	1.98
Hardie Board with Ceramic Tile	15/64	5.95
Wire Mesh (1 inch opening)	1/32	0.793
R13 Insulation Mounted on 2x4	3.5	88.9
Sediment Stone	2.5	63.5

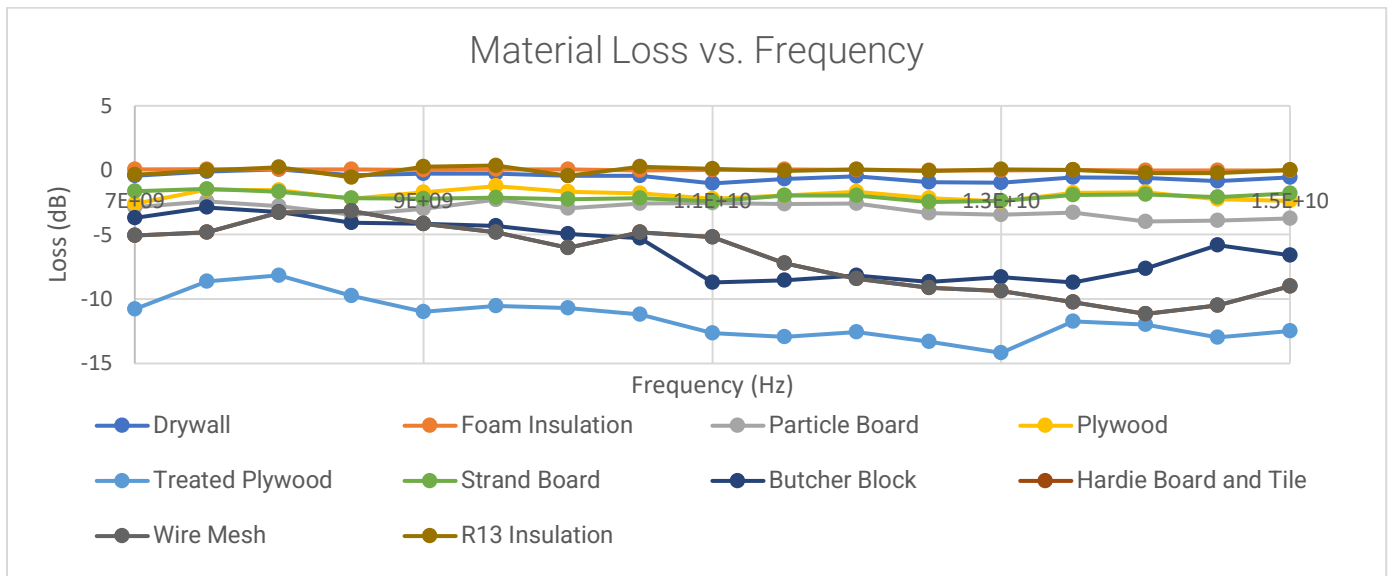


Figure 3.7: Summary of Measured Material Penetration Loss

### 3.1.3. Indoor Measurements

#### 3.1.3.1. Measurement in the Smart Production Lab



Figure 3.8: Picture of the Smart Production Lab at Aalborg University

- > Scenario: The Smart Production Lab at the Department of Mechanical and Manufacturing Engineering at Aalborg University.
- > Laboratory size: 41 x 14 x 6 m
- > The ceiling height of the Smart Factory is approximately 6.0 m, and the height of the metal beams under the ceiling is approximately 4.5 m
- > The height of Tx (i.e., UE) and Rx (i.e., BS): 1.2 m
- > Coordinate:
  - o The defined coordinate system is shown in Figure 3.9 (a).
  - o Each Tx site is always located to the east, west, south, or north of its neighboring point.
  - o In scenario (a), BS\_0 (-0.52m, 17.07m), the intervals between the adjacent Tx sites are 1 m, except for:
    - The next Tx site for a Tx site with coordinates (0.0m, 7.0m) is (0.0m, 9.0m)
    - The next Tx site for a Tx site with coordinates (0.0m, 9.0m) is (0.0m, 11.0m)
    - The next Tx site for a Tx site with coordinates (0.0m, 11.0m) is (0.0m, 13.0m)
    - The next Tx site for a Tx site with coordinates (0.0m, 20.0m) is (0.0m, 20.75m)
  - o In scenario (b), BS\_1 (0.0m, 0.0m), the intervals between the adjacent Tx sites or adjacent Tx and Rx sites are 1.0 m.
  - o In scenario (c), BS\_2 (2m, 36.75m), the intervals between the adjacent Tx sites are 1.0 m.

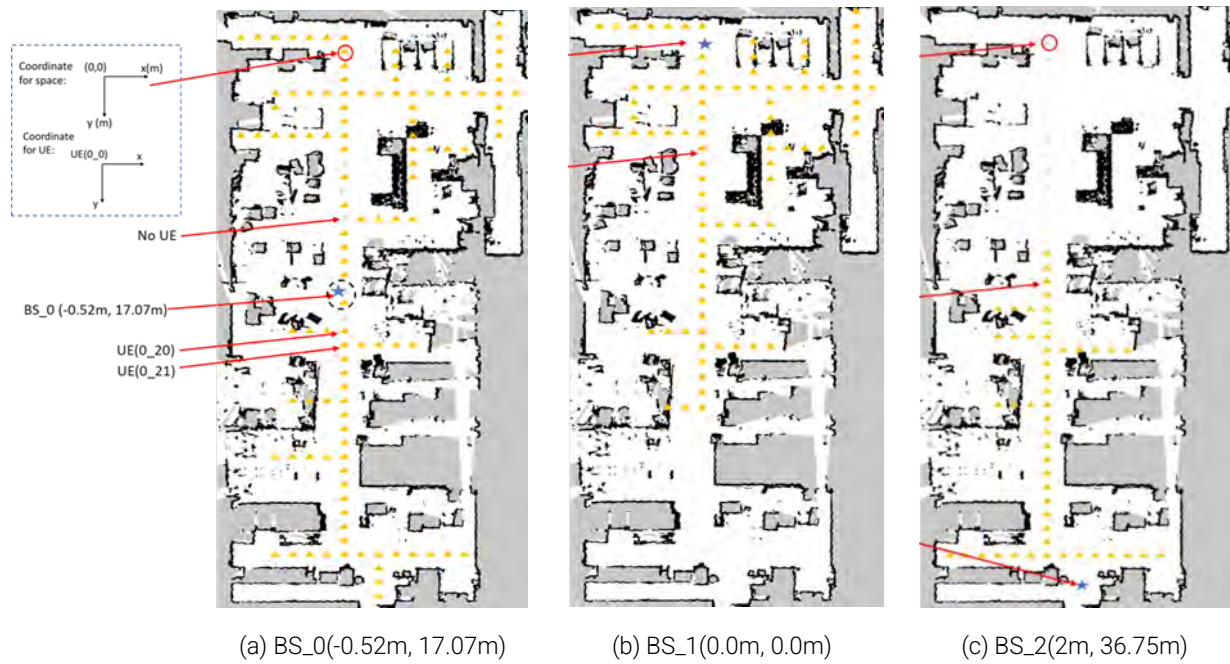


Figure 3.9: Measurement Map for (a) Rx<sub>0</sub>, (b) Rx<sub>1</sub> and (c) Rx<sub>2</sub>, where the Rx and the Tx are denoted by BS and UE, respectively

Table 3.2. VNA Settings and Measurement Parameters

VNA setting	Power [dBm]	Frequency [GHz]	Number of frequency points	IF Beam Width (BW) [Hz]
0	0	Band 1: 2.5 - 4.5 Band 2: 10 - 12 Band 3: 28 - 30	2001 for each band	500

Table 3.3. Measurement Configuration

	Antenna	Radius of Uniform Circular Array (UCA) [cm]	Number of UCA elements	Height [m]	Location number of UCA center
Tx	P bi-conical antenna/INFO SZ-2003000. Polarization: vertical. Gain: <ul style="list-style-type: none"> <li>• 3.5 GHz: 1 dB</li> <li>• 11.0 GHz: 3.2 dB</li> <li>• 29.0 GHz: 4.5 dB</li> </ul>	0	1	1.15	Rx <sub>0</sub> : 115 points Rx <sub>1</sub> : 89 points Rx <sub>2</sub> : 50 points
Rx		0	1	1.15	3

## Preliminary Results

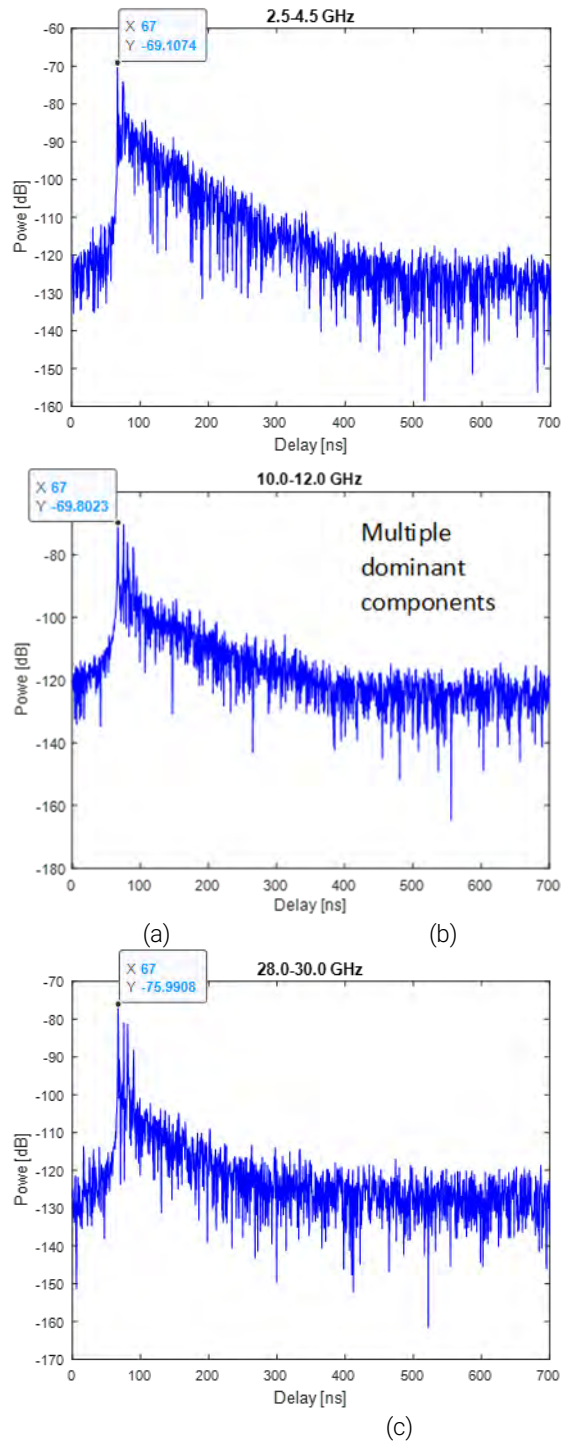


Figure 3.10: Preliminary Results of CIRs of Data BS\_1-UE(01,20) for the Three Frequency Bands

### 3.1.3.2. Measurement in the Production Factory

Indoor measurements were performed in several scenarios at the Keysight Technologies campus in Santa Rosa, CA. Scenarios included:

- > Conference room
- > Cafeteria, including LOS and NLOS scenarios
- > Automated production area

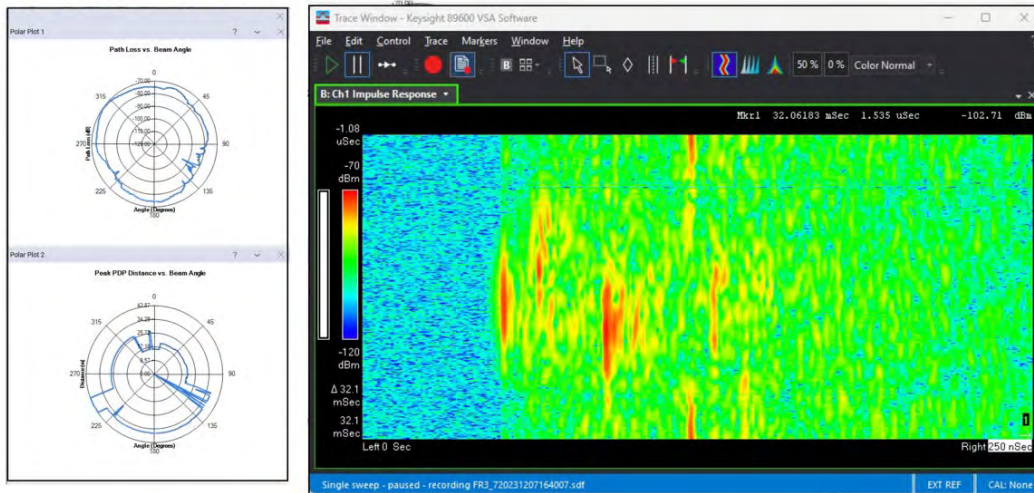
Measurements were performed with the channel sounding system described in Section 4.1.1 at carrier frequencies of 7.0, 10.25, and 13.0 GHz. Figure 3.11 shows the three measurement scenarios in the cafeteria. In the third setup, the Rx was placed directly behind a post blocking the site to the Tx.



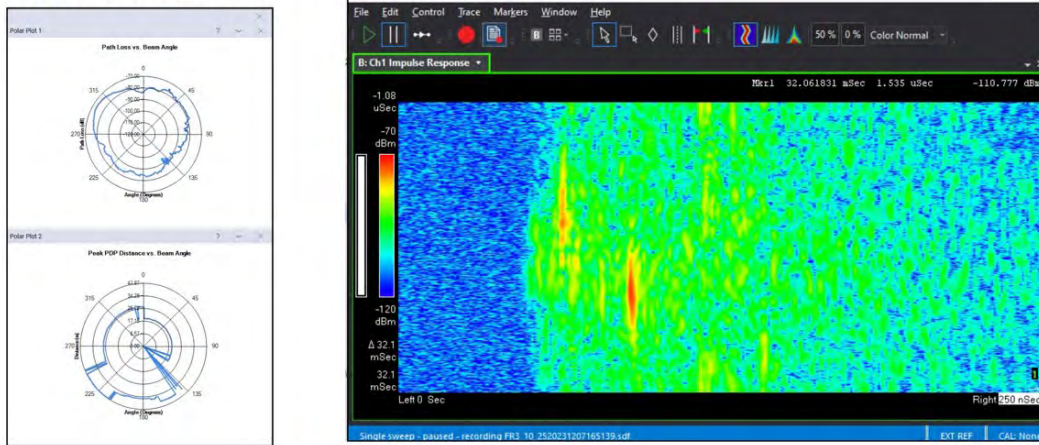
Figure 3.11: Keysight Cafeteria Measurement Locations

The obstructed LOS measurements showed different results dependent on the carrier frequency. Figure 3.12 shows the received signal strength in the obstructed LOS for each carrier frequency tested.

### LOS Obstruction 7 GHz



### LOS Obstruction 10.25 GHz



### LOS Obstruction 13 GHz

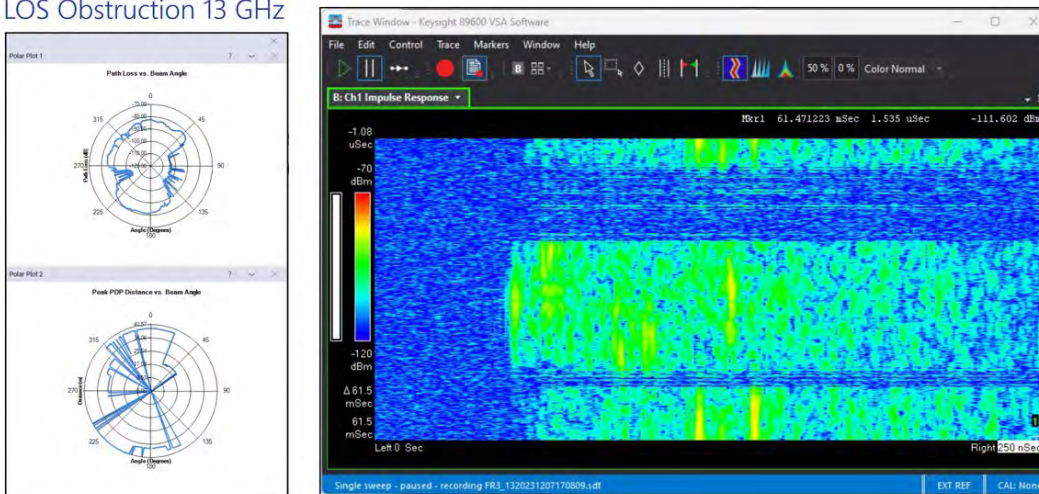


Figure 3.12: Obstructed LOS Signal Strength and Impulse Response

### 3.1.3.3. Indoor Office Measurements at 15 GHz

The indoor experiments were performed by placing the Tx at a fixed location and moving the mobile channel sounding Rx over different LOS and NLOS locations. Once the PL was recorded for all possible Rx locations for a given Tx location, the channel sounding Tx was moved to the next pre-determined location. The Tx locations were chosen in four floors of the AT&T labs building in Austin, Texas. The building is a nine-story concrete and steel frame commercial building with mixture of administrative (cubicle and closed office), lab spaces, and interconnecting corridors, as shown in Figure 3.13.

The indoor channel was measured at a total of 650 Rx points (over four floors and 11 Tx locations), 96 of which were LOS and 554 were NLOS locations. The Tx antenna height was set to 2.7m (except on one floor of the building with lower ceiling height, where the Tx was placed as close to the ceiling as possible), featuring a standard gain horn with 55 degrees HPBW in both horizontal and elevation planes. The Rx antenna was set at a 1.8m height.



Figure 3.13: Measurement Environments: (a) Building Exterior, (B) Corridor, (C) Open Seating Area

### 3.1.4. Outdoor Measurements

#### 3.1.4.1. University Campus Courtyard

Outdoor measurements were collected at the courtyard of the ES building from one Rx location and 130 Tx locations, as shown in the map in Figure 3.14.



Figure 3.14: Anritsu's Courtyard Measurement Map and Locations of the Tx (130 locations) and the Rx

Table 3.4: Courtyard Measurements Configurations

	Power [dBm]	Frequency [GHz]	Number of frequency points	IF BW [Hz]
VNA setting	0	Band 1: 2 - 16 Band 2: 28 - 30	14001 for band 1 2000 for band 2	1000

### 3.1.4.2. Industry Campus

Outdoor measurements were performed on the Keysight Technologies campus in Santa Rosa, CA. Measurements were performed at center frequencies of 7.0, 1.25, and 13.0 GHz using the channel sounding system described in Section 4.1.1. Locations of the Tx and Rx are shown in Figure 3.15.



Figure 3.15: Locations of Measurements at Keysight Technologies

Measurements were performed from each of two transmit locations, shown by the red dots, to 12 Rx locations, shown by the green dots. At each location, the Rx antenna pointed in each of the 360 degree azimuth angles and 7 elevation angles from -30 to 30 degrees in 10 degree steps. Impulse responses were captured for each measurement.

### 3.1.5. Directional Measurements

Directional measurements using Virtual Antenna Arrays (VAA) were collected from selected indoor and outdoor settings with a virtual UCA at one end using a rotating bi-conical or directional antenna over a fixed radius, and a stationary bi-conical antenna at the other end. Table 3.5 summarizes these measurements. Both the Tx antenna and the Rx antenna are placed 1.15m above its local ground. Tx power is set to 0 dB m, and VNA IF bandwidth is 500 Hz (unless other specified). Summary of directional measurements using UCA by Anritsu can be found in Table 3.5, and a list of antennas used is summarized in Table 3.6.

Table 3.5: Summary of directional measurements using UCA by Anritsu

	Antenna	Radius of UCA [cm]	Number of UCA elements	Frequency [GHz]	Number of frequency points
<b>Smart manufactory, 3 links</b>					
Tx	P bi-conical/INFO SZ-2003000	stationary			
		20	180	2-30	15001
Rx	P bi-conical/INFO SZ-2003000	41.5	360	2.5 - 4.5 10 - 12 28 - 30	2001 for each band
<b>Entrance of APMS ground-floor, case 1, 1 link with Tx-Rx separation of 7.45m</b>					
Tx	Homemade biconical antenna	stationary			
	P bi-conical/INFO SZ-2003000	18	180	2 - 30	15001
Rx	ASY-CWG-S(D)-265	11.5	360	26.5 - 40	7001
		20	360	38-40	1001
<b>Entrance of APMS ground-floor, case 2, 1 link with Tx-Rx separation of 6.1m</b>					

Tx	Homemade biconical antenna				
Rx	P bi-conical/INFO SZ-2003000	18	360	2 - 30	15001
<b>Corridor of 3<sup>rd</sup> floor of APMS, case 1, 8 links</b>					
Tx	ASY-CWG-S/D-082	20	180	8.4 – 10.4	2001
	ASY-CWG-S/D-265	10	180	26.5-40	7001
Rx	Homemade biconical antenna	Stationary, displaced to 8 different locations			
<b>Corridor of 3<sup>rd</sup> floor of APMS, case 2, 5 links</b>					
Tx	ASY-CWG-S(D)-124	20	180	12.4 – 18	2801
Rx	Homemade biconical antenna	Stationary, displaced to 5 different locations			
<b>Ground floor of APMS</b>					
Tx	Homemade biconical antenna				
Rx	P bi-conical/INFO SZ-2003000	20	360	20-30	5001
	MVG corrugated antenna	20	360	20-30	5001
	SAS-574 A.H. double ridge guide horn antenna	20	360	20-30	5001
	MVG corrugated antenna	50	720	18-35	8501
	ASY-CWG-124 corrugated antenna	50	720	12.4-18	2801
	P bi-conical/INFO SZ-2003000	50	720	2-30	14001
<b>Parking lot of APMS building</b>					
Tx	Homemade biconical antenna				
Rx	P bi-conical/INFO SZ-2003000	20	360	2.5-4.5 12-14 28-30	2001 for each band IF 1000Hz
<b>lawn beside ES building</b>					
Tx	Homemade biconical antenna				
Rx	P bi-conical/INFO SZ-2003000	20 / 21.5	360	2.5-4.5 12-14 28-30	2001 for each band IF 1000Hz
	ASY-CWG-124 corrugated antenna	20	180	12.5-14.5	2001
	ASY-CWG-265	20	360	28-30	2001

Table 3.6: Antenna used in the campaign by Anritsu

Antenna name	Polarization	Gain (HPBW, if specified)
Homemade biconical antenna	vertical	3.5 GHz: 0 dB; 11.0 GHz: 3 dB; 29.0 GHz: 5 dB
P bi-conical/INFO SZ-2003000	vertical	3.5 GHz: 1 dB; 11.0 GHz: 3.2 dB; 29.0 GHz: 4.5 dB
ASY-CWG-S(D)-265	vertical	26.5-40.0 GHz: 13.5 dBi, HPBW: 44 deg
ASY-CWG-S/D-082	vertical	8.2-12.4 GHz: 13.5 dBi
ASY-CWG-S(D)-124	vertical	12.4-18.0 GHz, 13.5 dBi, HPBW: 44 deg
MVG corrugated antenna	vertical	18-40.0 GHz, 11 dBi, HPBW: 50 deg
SAS-574 A.H. Systems double ridge guide horn antenna	vertical	18-40 GHz, 15-21.2 dBi, HPBW: around 20 deg
ASY-CWG-124 corrugated antenna	vertical	12.4-18 GHz, 13 dBi, HPBW: 44 deg

### 3.1.6. Channel Model for Path Gain and Delay Spread, in Comparison to Existing Models of 38.901

In this subsection, we present the data analysis and channel modeling for path gain and delay spread done by Nokia Bell Labs based on measurement data provided by Anritsu for an indoor smart manufactory lab environment and a courtyard with vegetations.

#### 3.1.6.1. Path Gain and its Frequency Dependence in a Factory

Average path gain on all 254 links measured in the factory is plotted vs. Tx-Rx distance in Figure 3.16 for the three bands. Also shown are the best common-slope fit lines. Measurements in each band are labeled by the center

frequency of the band, thus 3.5 GHz, 11 GHz, and 29 GHz. The best-fit common distance exponent is found to be 2.17. Best-fit lines are separated within 2 dB of what would be expected from frequency squared scaling of path gain.

A more illustrative way to display frequency dependence of PL beyond what is expected in free space is to plot path gain relative to free space, thus Relative Gain = Path gain – Free Space gain, shown in Figure 3.17. Also shown are the three common slope fit lines. The fit lines for the three bands in Figure 3.17 are within 3 dB of each other, thus exhibiting only weak frequency dependence, as compared to absolute path gain in Figure 3.16 spanning some 20 dB for the 3 bands.

Point-by-point frequency dependence is now examined by calculating the excess loss, defined as pairwise difference between the measured path gains reference to 1m Free Space Pathloss (FSPL) in different bands (to compensate the expected frequency squared scaling of PL):

$$Excess\ Loss = (P_G(f_1) - 20\log_{10}(\lambda_1/4\pi)) - (P_G(f_2) - 20\log_{10}(\lambda_2/4\pi)) \quad (3-1)$$

where  $f_1 < f_2$ , with  $f_1, f_2 \in [3.5, 11, 29]$  GHz. Cumulative distribution of excess loss (3-1) for the three band pairs (3.5, 11), (11,29), and (3.5,29) GHz measured at all 254 factory locations is plotted in Figure 3.18. Values of Excess loss >0 dB indicates locations where the PL gap is larger than that given by frequency squared scaling.

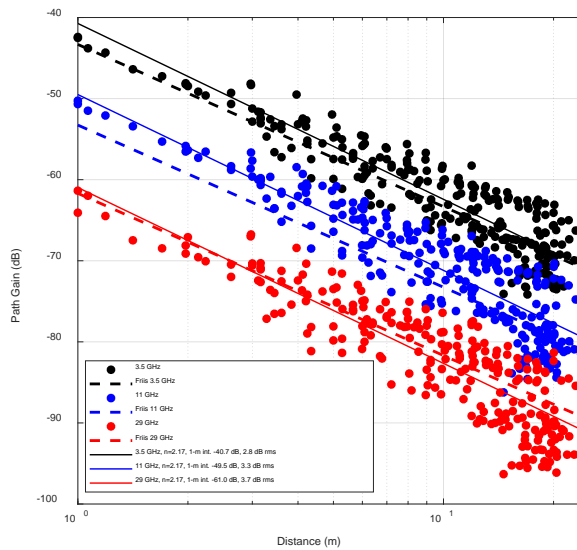


Figure 3.16: Measured Average Path Gain in Factory for Three Bands

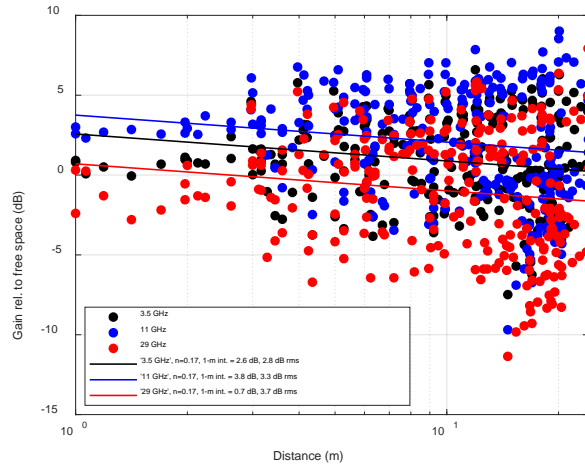


Figure 3.17: Gain Relative to Free Space in a Factory

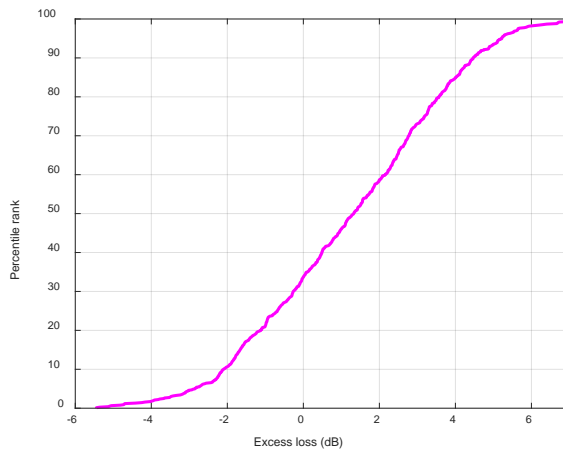


Figure 3.18: Cumulative Distribution Function (CDF) of Measured Excess Loss (3-1) in a Factory, All Locations

Measured excess loss values are observed to cover both negative and positive values, with a median of 1.3 dB. This is an indication of a very weak path gain bias in favor of lower frequencies, beyond the expected frequency squared scaling.

Path gain and related quantities in Figure 3.16, Figure 3.17, and Figure 3.18 covered all measured locations. It may be argued that power in LOS locations is dominated by a direct arrival, for which path gain scaling with frequency as in free space is particularly unsurprising. Yet coverage concerns arise most often in NLOS conditions. It is therefore of interest to examine path gain frequency dependence in NLOS locations. Measured path gain excess loss for NLOS locations where distance >10m are plotted in Figure 3.19 and Figure 3.20, respectively. The common slope fit lines for NLOS path gain are seen in Figure 3.19 to span about 20 dB for the three bands, consistent with frequency<sup>2</sup> path gain scaling, as in free space and in 3GPP recommendations. Point by point NLOS excess loss between bands is seen in Figure 3.20 to have both positive and negative values, with a median of 2.3 dB indicating a weak bias in favor of lower frequencies.

It is thus concluded that path gain measured in this factory both for all locations and the NLOS subset scales as frequency squared, as per 3GPP recommendations.

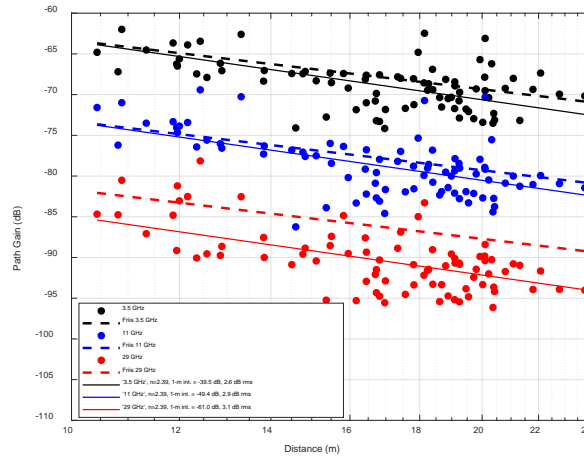


Figure 3.19: Path Gain Measured in NLOS Links, >10m Distance in a Factory

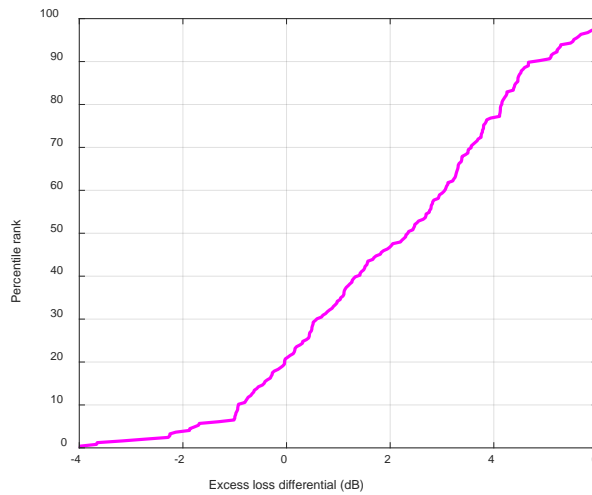


Figure 3.20: CDF of Excess Loss Measured in NLOS Links, >10m Distance in a Factory

Measured path gain in NLOS factory links at 3.5 GHz and 29 GHz is compared in Figure 3.21 and Figure 3.22 to two of the 3GPP factory models (SH-inF and DL-inF) [2], as well as a published theoretical model [18], attributing main NLOS propagation mechanism in a factory to the ceiling reflection. The theoretical model was previously found [18] to be more accurate against diverse factory environments. Both the 3GPP and the theoretical model predict path gain as scaling with the square of the center frequency. It is seen in Figure 3.21 and Figure 3.22 that both the 3GPP models and the theoretical model are accurate in predicting the current data, with Root Mean Square (RMS) errors below 3.5 dB.

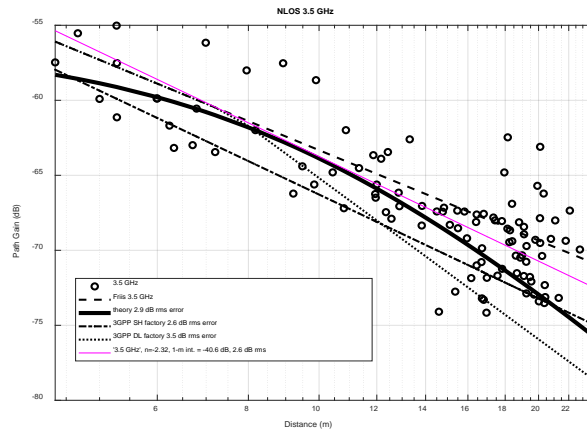


Figure 3.21: Measured Path Gain in Factory NLOS Links at 3.5 GHz, Compared Against 3GPP and Theoretical Models

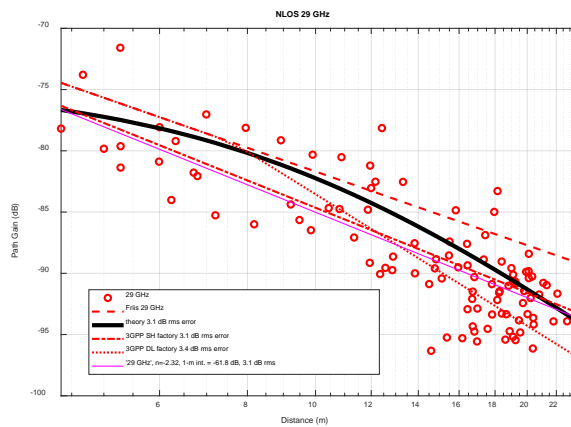


Figure 3.22: Measured Path Gain in Factory NLOS Links at 29 GHz, Compared Against 3GPP and Theoretical Models

### 3.1.6.2. RMS Delay Spread in a Factory

Impulse responses computed from measured complex frequency response of the channel were processed to extract RMS delay spread. To reduce the impact of weak, possibly noisy, arrivals at long delays, only the strongest arrivals constituting 90% of measured power were kept.

Cumulative distributions of the RMS delay spread in LOS and NLOS conditions are plotted for the three bands in Figure 3.23 and Figure 3.24. The RMS delay distributions for different bands are seen to be quite close to each other, with no definitive trend in favor of lower or higher frequencies: As the center frequency increases, the median RMS delay spreads decrease in LOS links (Figure 3.23) from 16 to 10 ns and increase in NLOS links (Figure 3.24) from 22 to 24 ns. Measured RMS delay spreads are also seen even smaller than RMS delay spreads recommended by the 3GPP, whose recommended delay spreads for factories are independent of center frequency.

It is therefore concluded that no RMS delay spread dependence on center frequency in factories is warranted based on this study, in line with the 3GPP recommendation.

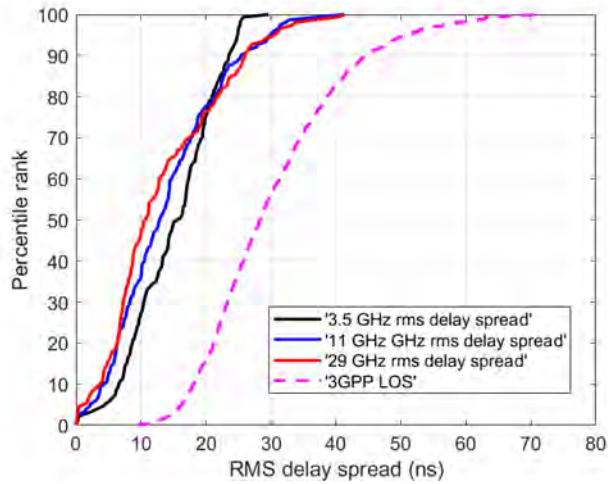


Figure 3.23: RMS Delay Spread in Factory LOS Links

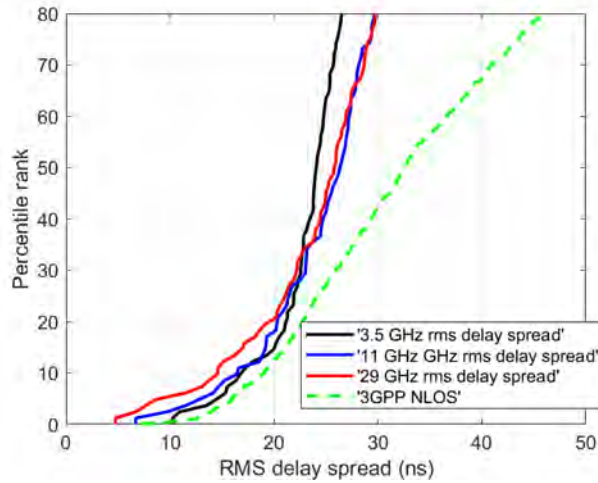


Figure 3.24: RMS Delay Spread in Factory NLOS Links

### 3.1.6.3. Courtyard Path Gain

Similar measurements of channel complex frequency response have been conducted in a courtyard, in both LOS and NLOS conditions, at ranges reaching 90 m. Corresponding path gains are plotted in Figure 3.25 and Figure 3.26. It may be observed that the separation between the common slope line fits for the 3 bands are within 2 dB of what is expected based on frequency squared path gain scaling.

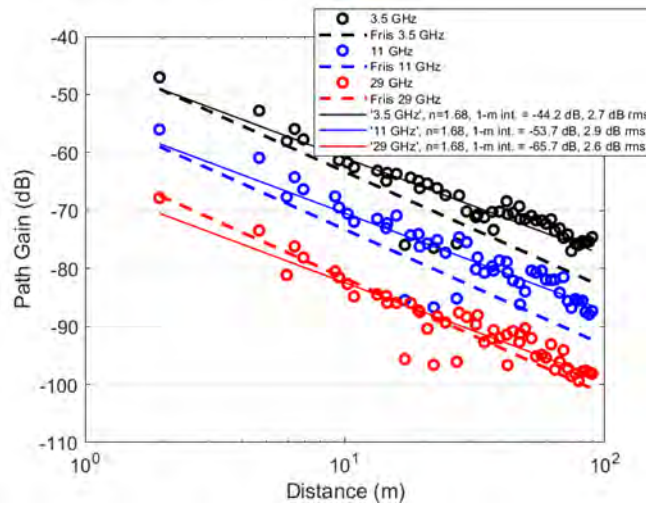


Figure 3.25: Measured Average Path Gain in Courtyard LOS Links for Three Bands

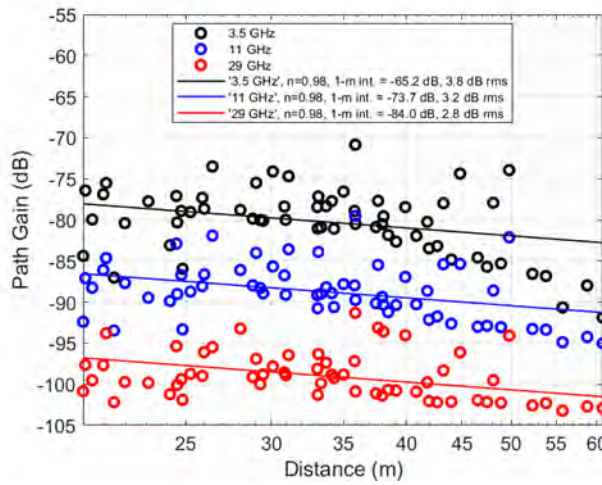


Figure 3.26: Measured Average Path Gain in Courtyard NLOS Links for Three Bands

Cumulative distribution of the point-by-point excess loss (3-1) for NLOS links is shown in Figure 3.25. The median excess loss differential value of 0.3 dB is an indication of negligible impact of center frequency on path gain in the collected data, beyond the frequency<sup>2</sup> used in models.

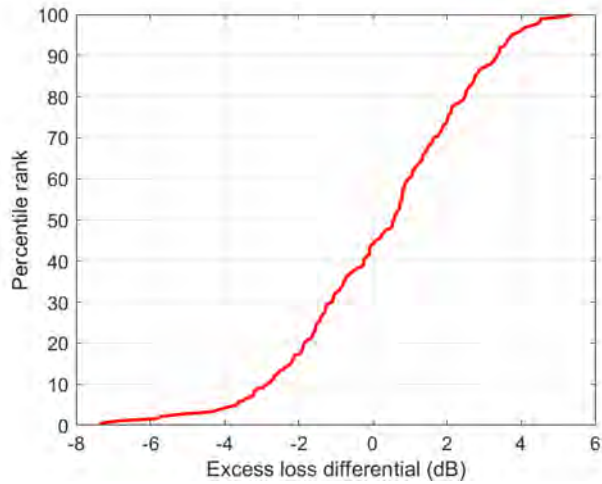


Figure 3.27: CDF of Point-by-Point Excess Loss Differential (3-1) Measured in NLOS Links, >20m Distance in a Courtyard

### 3.1.6.4. RMS Delay Spread in a Courtyard

Cumulative distributions of the RMS delay spread in LOS and NLOS conditions are plotted for the three bands in Figure 3.28 and Figure 3.29. Median RMS delay distributions for different bands range from 18-26 ns in LOS and 45-60 ns in NLOS, increasing as the center frequency increases. This is in contrast to the 3GPP Umi (Urban-street-canyon) model, which predicts a decrease in RMS delay spread as center frequency increases. Because the 3GPP Umi model is stated as applicable to ranges reaching 5 km, it is unclear if it is an appropriate representation of the courtyard environment measured in this work.

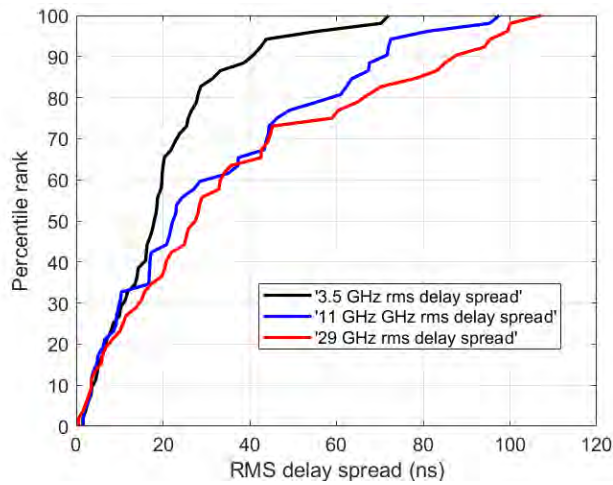


Figure 3.28: RMS Delay Spread in Courtyard LOS Links

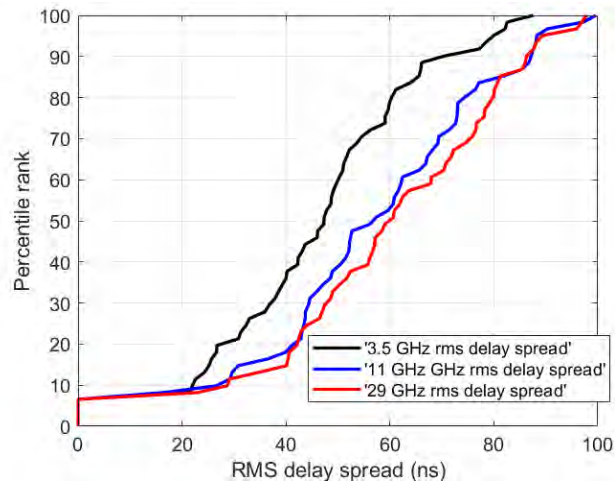


Figure 3.29: RMS Delay Spread in Courtyard NLOS Links

### 3.1.6.5. Conclusions

Wideband channel response measurements were collected in 254 factory links at ranges up to 25m and 125 courtyard links at ranges up to 90 m, in both LOS and NLOS conditions. Wideband biconical antennas were used at each location, allowing direct comparison of channel path gain and RMS delay spread in three 2 GHz-wide bands, centered on 3.5 GHz, 11 GHz, and 29 GHz. Key findings include:

- > A weak (<2 dB) increase in PL as center frequency increased from 3.5 GHz to 29 GHz, aside from expected frequency squared, in line with standard models (3GPP), in both factory and courtyard.
- > No systematic rms delay spread dependence on center frequency in the factory. This is in line with 3GPP factory models on center frequency.
- > A modest increase in median RMS delay spreads in a courtyard (45 to 60 ns in NLOS) as center frequency increases from 3.5 GHz to 29 GHz. Observed delays are smaller than those predicted by 3GPP in urban street canyons, which predicts a decrease in RMS delay spread as center frequency increases.

### 3.1.7. Analysis and Channel Modeling for Indoor Office Environment at 15 GHz

The Floating Intercept (FLPt) PL model is defined as:

$$PL[\text{dB}] = PL_0 + 10 \gamma \log_{10}(d) + \sigma_s,$$

where  $PL_0$  (the intercept of the PL model),  $\gamma$  (the Path Loss Exponent (PLE)), and  $\sigma_s$  (the lognormal shadow fading) are computed via least squares estimation [31].

The floating intercept PL model was fit to indoor omnidirectional PL data collected by AT&T over 650 Rx locations, across four floors. A typical floorplan where the measurements were conducted is depicted in Figure 3.30, with the red dots indicating the Rx locations where the sounding signal from Tx 0 was measured, and the green dots indicating the Rx locations where the sounding signal from Tx 1 was measured.

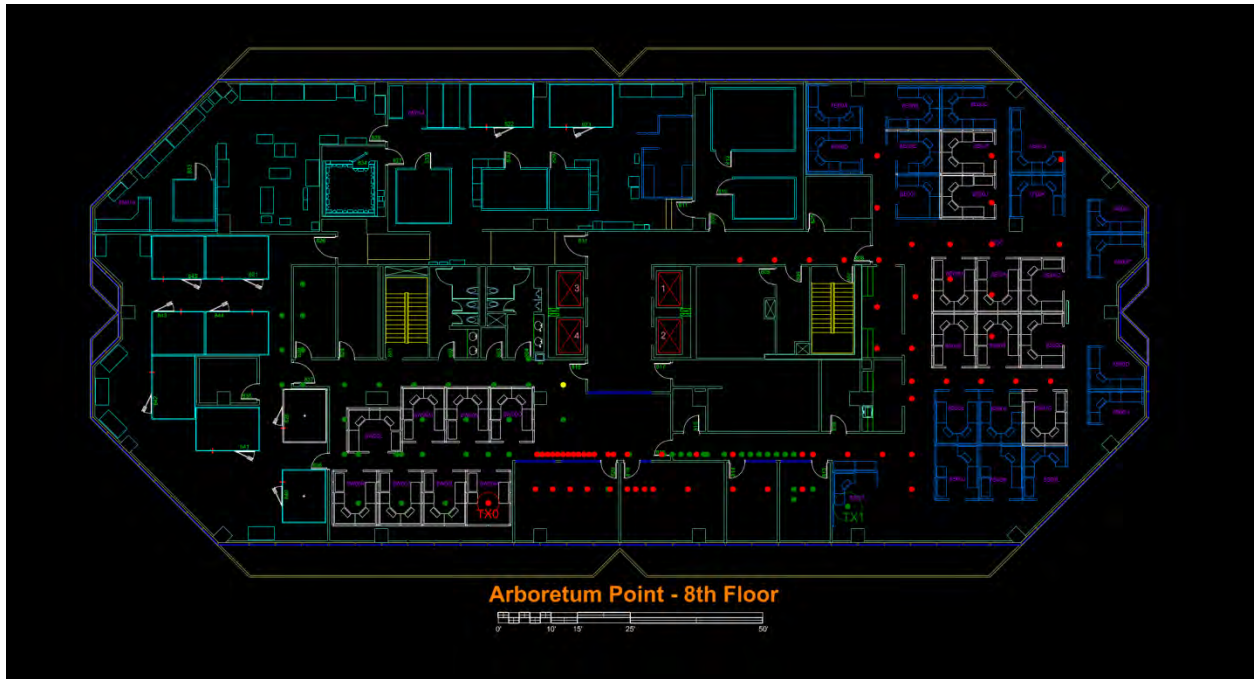


Figure 3.30: Floor plan of one of the four floors where indoor propagation measurements were conducted at 15 GHz. The Rx locations were selected uniformly in the log scale, with more Rx locations selected close to each Tx over a decade of distance.

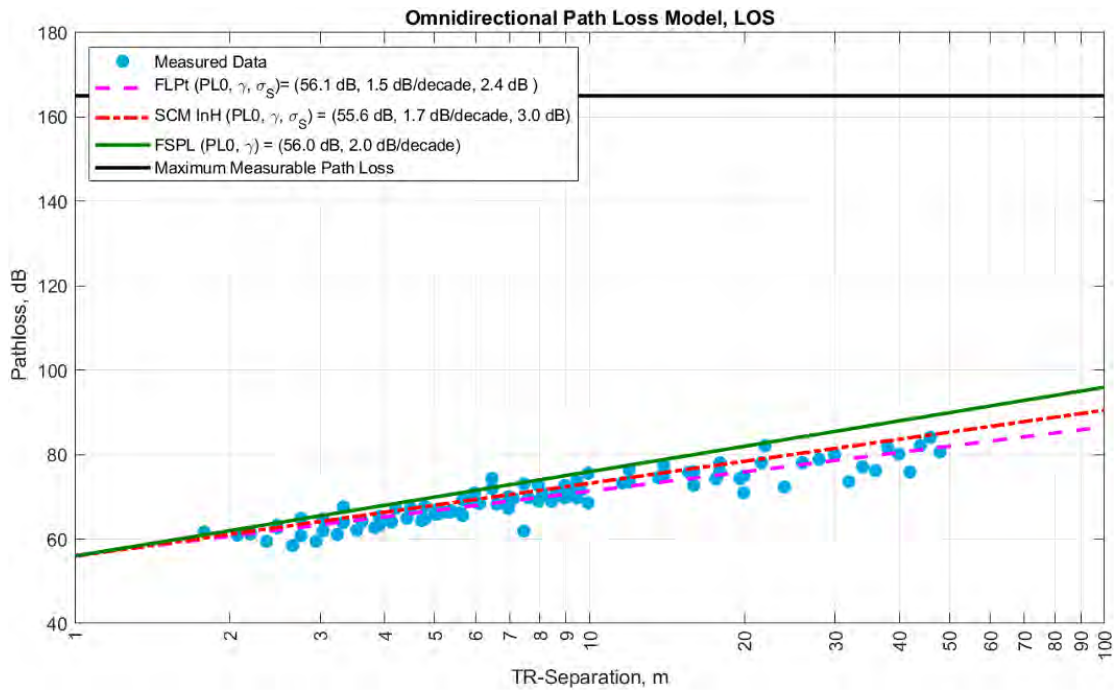


Figure 3.31: Measured PL (blue dots) in LOS Environments Over 96 LOS Locations at 15GHz. The FLPt PL model (dotted magenta line) is fit to the data.

Figure 3.31 illustrates omnidirectional PL data at 15 GHz, collected by the omnidirectional Rx (as described in Section 3.1.1.3) over 96 LOS locations across four floors of an office building. All collected PL data was within the maximum measurable PL of the channel sounding system with the omnidirectional Rx (165 dB).

The PLE of 1.5 dB/decade in LOS is consistent with the current InH LOS 3GPP Spatial Channel Model (SCM) model PLE of 1.7 at 15 GHz [2].

Similarly, Figure 3.32 illustrates omnidirectional PL data at 15 GHz, collected by the omnidirectional Rx (as described in Section 3.1.1.3) over 554 NLOS locations across four floors of an office building. All collected PL data was once again within the maximum measurable PL of the channel sounding system with the omnidirectional Rx (165 dB). Note that the SCM PL model depicted above is the NLOS “arm” of the dual-line 3GPP SCM InH PL model ( $PL'_{\text{InH-NLOS}} = 38.3 \log_{10}(d_{3D}) + 17.30 + 24.9 \log_{10}(f_c)$ ) [2].

The floating-point PL model was used to model the collected omnidirectional PL. The PLE of 3.4 dB/decade in LOS is consistent with the current InH LOS 3GPP SCM model PLE of 3.8 at 15 GHz [2].

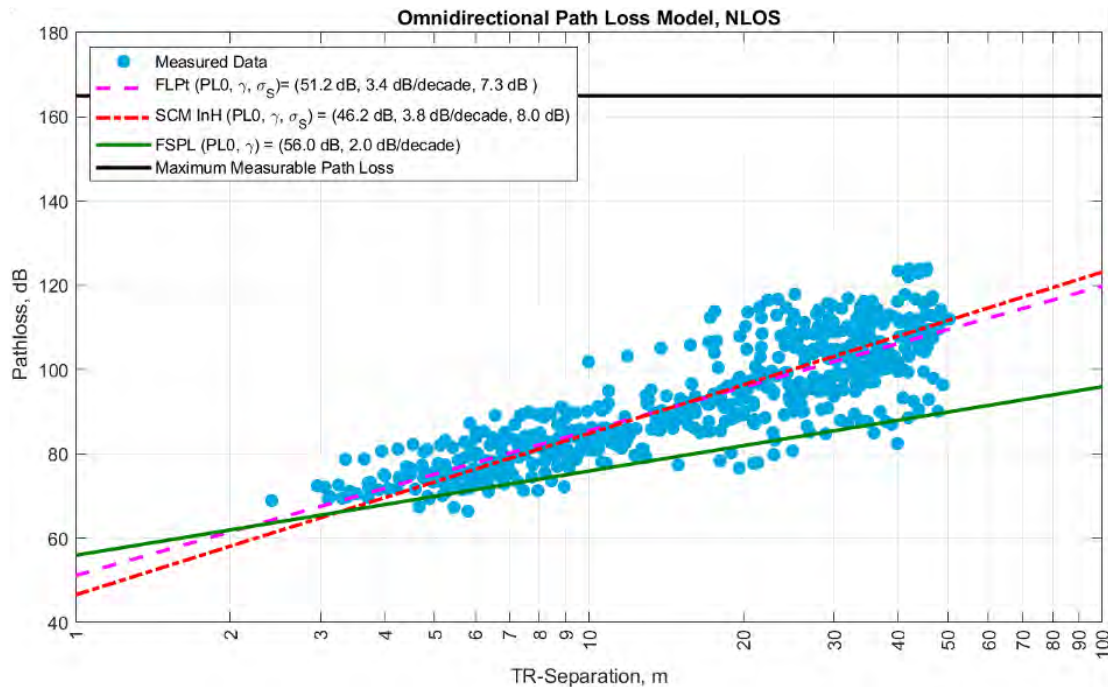


Figure 3.32: Measured PL (blue dots) in NLOS Environments Over 554 LOS Locations at 15 GHz. The FLPT PL model (dotted magenta line) is fit to the data.

Shadow fading ( $\sigma_s$ ) is obtained by subtracting the distance dependent mean PL from the measured PL, i.e.:

$$\sigma_s = PL[dB] - PL_0 - 10 \gamma \log_{10}(d)$$

Shadow fading is typically modeled as a lognormal random variable with zero mean. Shadow Fading Log normal plot distribution is shown in Figure 3.33.

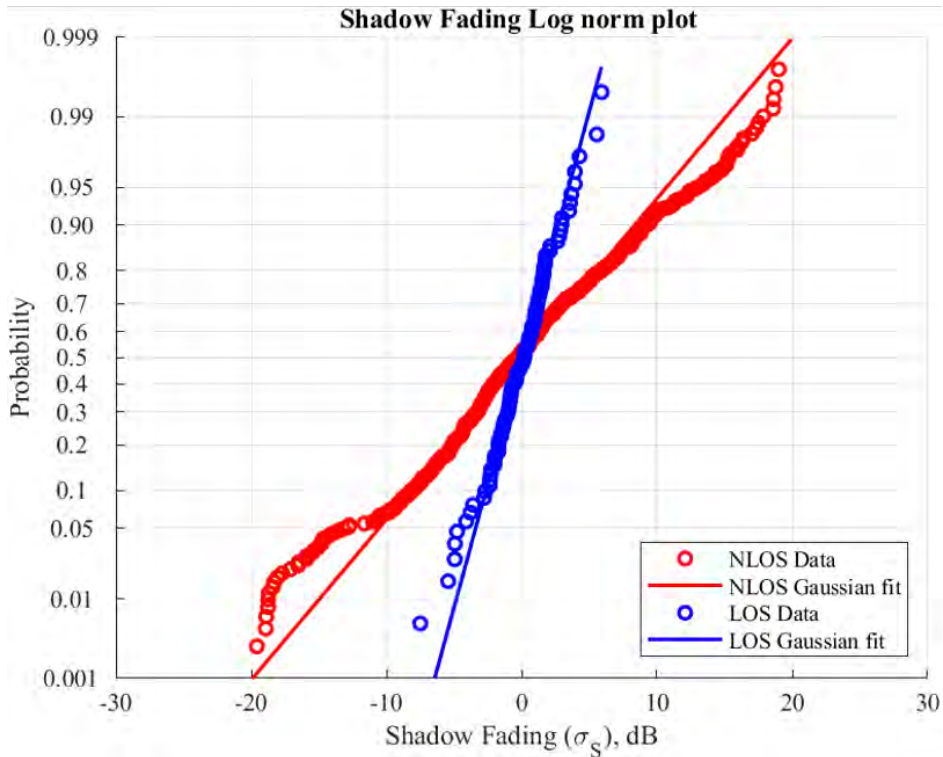


Figure 3.33: Distribution of Shadow Fading in LOS and NLOS Environments

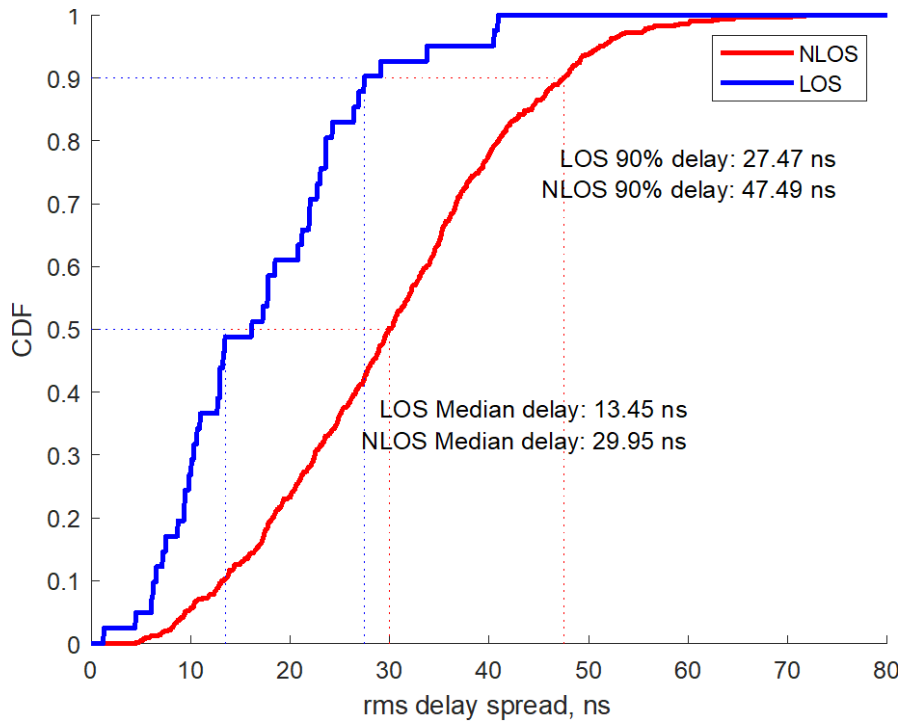


Figure 3.34: CDF of Delay Spread in LOS and NLOS Environments

The CDF of the delay spread is plotted in Figure 3.34. A median delay spread of 13.45 ns was observed in LOS environments, while a much greater median delay spread of 29.95 ns was observed in NLOS environments.

The CDF of the azimuth and elevation angular spread is plotted in Figure 3.35 and Figure 3.36, respectively. Although the median azimuth angular spread in NLOS environments ( $61.62^\circ$ ) is nearly twice the azimuth angular spread in LOS environments ( $32.97^\circ$ ), the elevation angular spread is similar for LOS and NLOS environments. This suggests that multipath components arrive from a wider spread of angles in the azimuth in NLOS environments, but are comparatively less dispersed in the elevation in both LOS and NLOS environments.

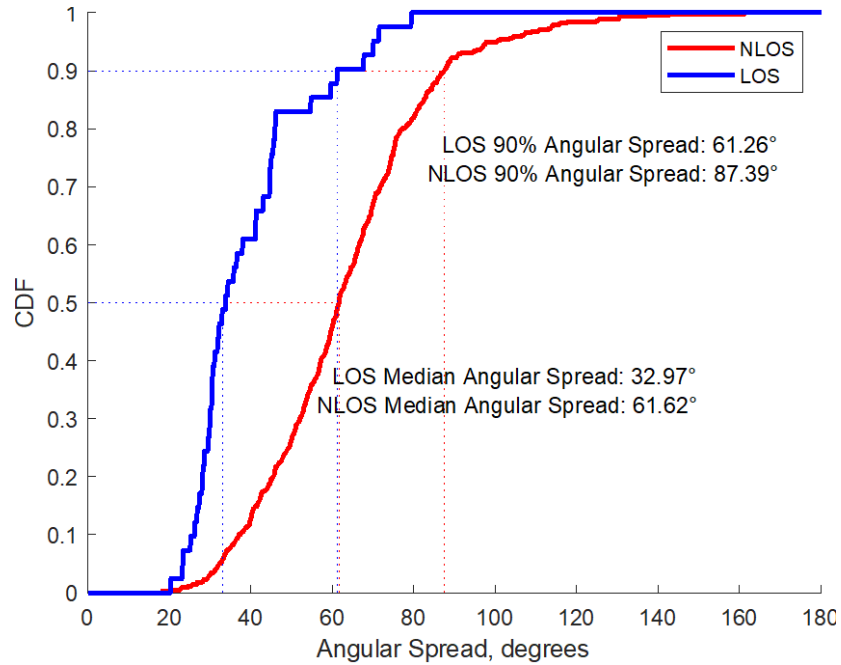


Figure 3.35: CDF of Azimuth Angular Spread in LOS and NLOS Environments

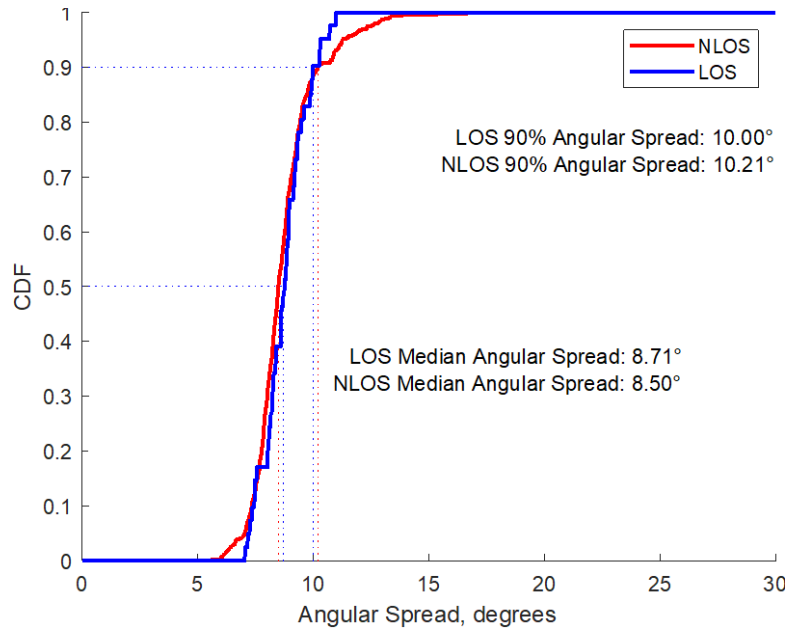


Figure 3.36: CDF of Elevation Angular Spread in LOS and NLOS Environments

Channel parameters estimated by AT&T from the indoor office propagation measurements at 15 GHz were compared against the values proposed by 3GPP, as shown in Table 3.7. A good agreement was observed between the values of PLE, shadow fading, and the mean and standard deviation of the logarithmic delay spread, and the azimuth angular spread estimated by AT&T and the values predicted in 3GPP TR 38.901 [2].

Table 3.7: Channel Parameters Comparison Between AT&T Indoor Measurements at 15GHz and 3GPP InH Model in TR 38.901

Parameter		LOS		NLOS	
		3GPP Model	AT&T Measurements	3GPP Model	AT&T Measurements
PLE		1.7	1.5	3.8	3.4
Shadow Fading		3.0	2.4	8.0	7.3
log(Delay Spread/1s)	$\mu$	-7.70	-7.94	-7.51	-7.57
	$\sigma$	0.18	0.34	0.17	0.22
log(ASA/1°)	$\mu$	1.55	1.57	1.73	1.78
	$\sigma$	0.26	0.15	0.20	0.15
log(ZSA/1°)	$\mu$	1.13	0.94	1.21	0.94
	$\sigma$	0.22	0.05	0.64	0.06

### 3.2 Communication Channel Model for D-Band & Above

This application has been de-prioritized by the 3GPP for Rel. 19 and is left to be addressed in the future. It is foreseen that important topics would include penetration loss for various materials, as well as measurement-based models for large scale parameters, such as PL, angle, and delay spreads.

# 4 TARGET MODELING

Channel propagation models are defined by the properties of the link between a Tx and Rx pair. The link, in turn, can be expressed through the properties of the LOS propagation ray together with the rays scattered by objects in the environment. The 38.901 channel model [2], which was designed for communications applications, is cluster based, meaning that the rays scattered from a distinct object in the environment are represented as a cluster of rays. This enables the gross motion of the object (or the motion of the base and/or use stations with respect to the object) to be represented by a clusterhead through one of the two procedures provisioned by the model for Spatial Consistency (SC): either SC-A, a deterministic procedure, or SC-B, a stochastic procedure. The rays of the cluster are geometrically distributed in a random manner around the clusterhead, as shown in Figure 4.1. This is sufficient for communications applications because it is the aggregate properties of the rays that matter to define key communications metrics such as large-scale and small-scale fading. For sensing applications, it is the properties of the individual rays scattered from the target objects – in particular how they vary in a spatially and temporally consistent manner – that define the very radio-frequency (RF) signature that is used for sensing targets. Hence, a random distribution of the rays around the clusterhead may not satisfy the requirements for all sensing use cases.

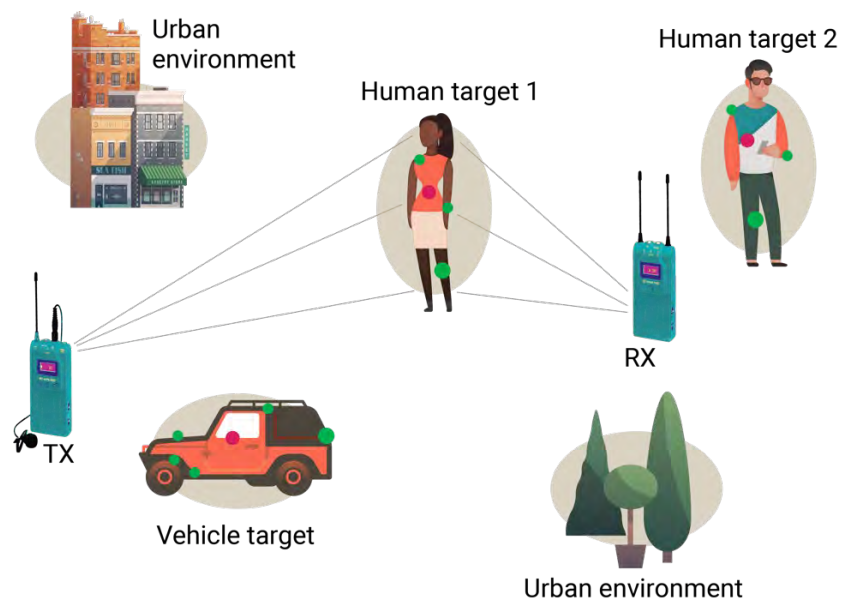


Figure 4.1: Illustrative JCAS Channel Model, Composed of One Class of Environment Clusters (Urban) and Several Classes of Target Clusters (Human, Vehicle)

Given the different requirements for communications and sensing applications, to produce a channel model that meets the requirements for JCAS applications, we propose characterizing separate models for environment classes (urban, suburban, office, factory, etc.) and for target classes (humans, vehicles, UAVs, robots, etc.). That way, the channel can be represented by the collection of rays from the environment clusters plus the rays from the target clusters. Specifically, any realization of the channel will be defined by a single environment class and by a number of target classes (and multiple realizations of each target class): e.g., urban environment + two human targets + one vehicle target. Thus, for

the most general representation of the JCAS channel model, the environment class model and the target class models can be combined into a single realization. The additional advantage is that a wealth of models for many different environment classes at many different center frequencies already exist and can be leveraged.

In this section, we focus on the characterization of the target models from measurements on a number of target classes ranging from humans to vehicles to drones to robots. First, we describe the channel sounder and the measurement campaign. Then we describe the target models reduced from the measurements.

## 4.1. Channel Measurements

### 4.1.1. NIST Channel Sounder

To model the target channel under several sensing use cases, a context-aware channel sounder, as shown in Figure 4.2, was utilized. This sounder features an RF system to extract multipaths from the RF measurements and camera/Lidar systems to assist in refining the channel model by, for example, identifying the scattering centers, responsible for the signal scattering.

The Tx and Rx in the RF system feature 28.5 GHz 8x8 phased-array boards of microstrip antennas spaced a half-wavelength apart (see Figure 4.2(a)). The Tx features a single board only, while the Rx features four boards stacked in a skew tetromino configuration (see Figure 4.2 (b)) to increase angular resolution in both dimensions, forming a 256-element antenna array. At the Tx, the probing signal is a repeated M-ary Pseudorandom (PN) sequence with 2047 chips; the chip duration is 0.5 ns, corresponding to a baseband signal bandwidth of 2 GHz. The PN sequence is generated at the baseband and modulated at an IF of 4 GHz by an arbitrary waveform generator. The IF signal is fed to the Tx antenna board and subsequently upconverted to precisely 28.5 GHz through an onboard mixer and radiated. An optical cable was used for phase synchronization between the Tx and Rx and for coordinated switching of the Rx antennas at each repeated PN sequence at the Tx.

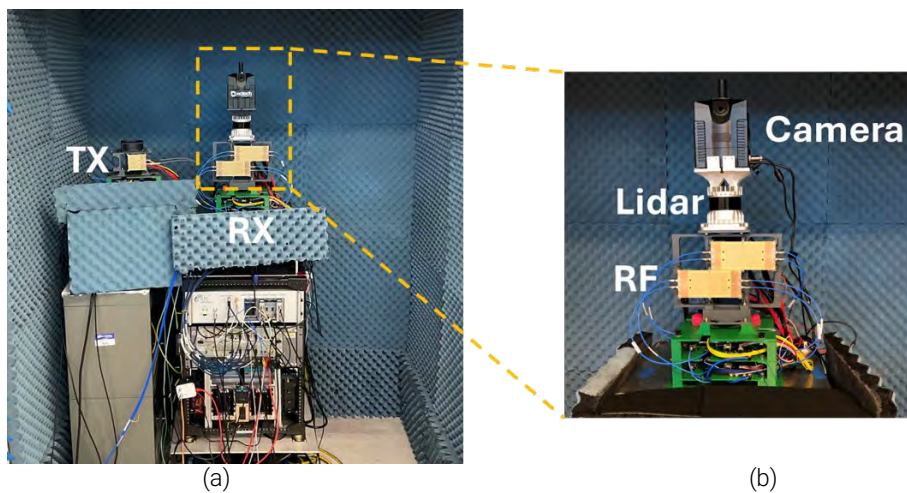


Figure 4.2. Context-Aware Channel Sounder Where Rx Has Four Stacked 28 GHz 8x8 Phased-Array Antennas and the Camera and the Lidar Mounted Above Them

At the Rx, the received signal at each antenna is downconverted back to IF and directly digitized at 16 Giga samples/s. The digitized signal is then matched and filtered with the known PN sequence to generate a complex CIR in delay. Predisortion filtering is employed to reduce the delay sidelobes of the matched filtered response to the PN sequence to 47 dB. For each case, a channel acquisition consists of 256 CIRs (across the Rx antennas) acquired at a sample interval indexed through  $t$  during an observation period. In postprocessing, the 256 CIRs of a single acquisition are beamformed every  $1^\circ$  within the field-of-view (FoV) of the boards (4,500 beams) and then synthesized through the SAGE super-resolution algorithm to extract multipaths per time  $t$ , indexed as path gain (complex amplitude squared)  $PG_{tg}(t)$ , delay  $\tau_{tg}(t)$ , azimuth AoA  $\phi_{tg,AoA}(t)$ , and Zenith Angle of Arrival (ZoA)  $\theta_{tg,ZoA}(t)$ . The azimuth AoD  $\phi_{tg,AoD}(t)$  and Zenith Angle of Departure (ZoD)  $\theta_{tg,ZoD}(t)$  from the Tx of any multipath can be computed uniquely from its AoA, ZoA, and delay [8]. Here subscript  $tg$  is in reference to the target channel model. Note that the sample interval and the total observation period depend on the specific measurement campaign, as specified in Table 4.1.

#### 4.1.2. AT&T Channel Sounder

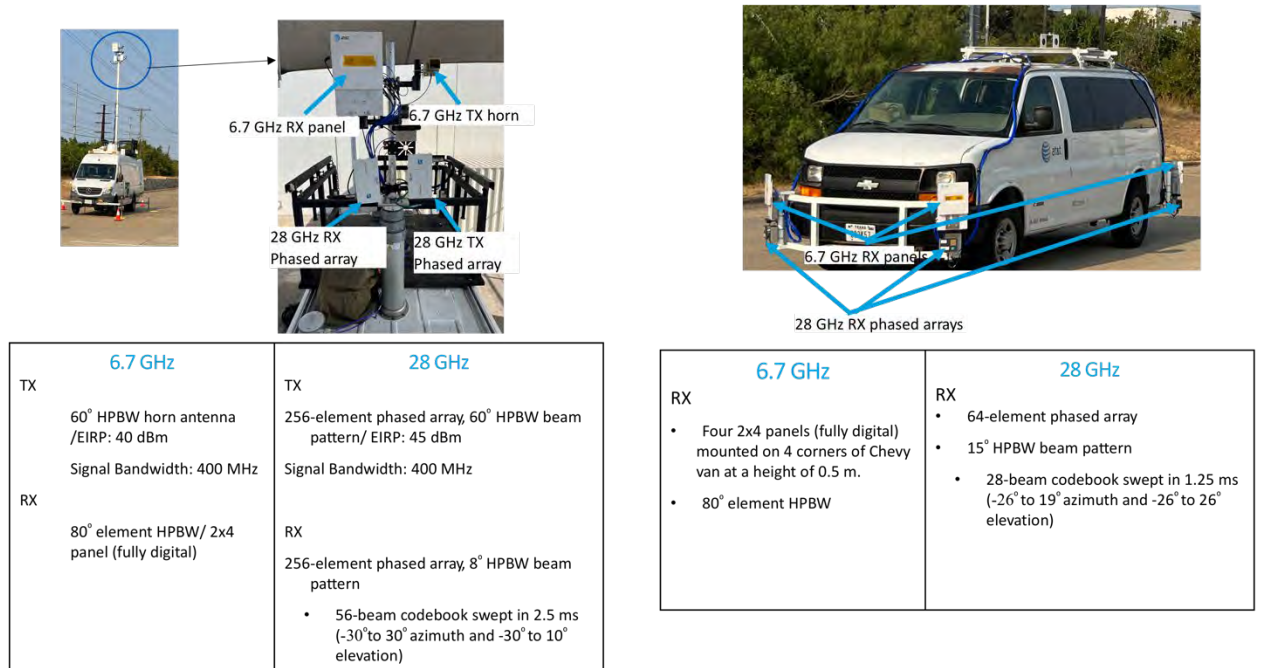


Figure 4.3: AT&T's Channel Sounder for ISAC

AT&T's measurements for ISAC object detection and tracking were conducted outdoors at AT&T's Spectrum drive facility in Austin, Texas. The measurements consisted of a fixed gNB and a mobile UE, as shown in Figure 4.3. A Tx and Rx antenna were mounted on the gNB. The targets used were (i) a Ford Transit consumer vehicle and (ii) a pedestrian. Both 28 GHz and 6.7 GHz frequencies were used with a signal bandwidth of 400 MHz (subcarrier spacing of 120 kHz) at each carrier frequency.

The BS Tx was mounted on a mast at a height of 10m, featuring (i) a 60 degree HPBW horn antenna with an Effective Isotropic Radiated Power (EIRP) of 40 dBm/400 MHz at 6.7 GHz and (ii) a 256-element phased array with a 60 degree HPBW beam pattern at an EIRP of 45 dBm/400 MHz at 28 GHz. The BS Rx for mono-static based sensing is (i) a 2x4 panel (fully digital) with an 80 degree HPBW per antenna element, at 6.7GHz and (ii) 256-element phased array with an 8 degree HPBW per beam at 28GHz. Beam sweeping is done with a 56-beam codebook swept in 2.5 ms (-30 degrees to 30 degrees azimuth and -30 degrees to 10 degrees in elevation). The mobile Rx for bi-static sensing consists of (i) four 2x4 panels (fully digital panels) mounted on four corners of the van at a height of 0.5 m, with a 80 degree per element HPBW, (ii), a 64-element phased array with a 15 degree HPBW per beam at 28GHz, with beam sweeping done with a 28 beam codebook swept in 1.25ms (-26 degrees to 19 degrees azimuth and -26 degrees to 26 degrees elevation).

For the experiments, the UE was parked at fixed location while targets roamed the test track. All nodes were precisely tracked and time-synchronized for the duration of the data collection using a Global Positioning System (GPS) with 1 cm resolution. Complex channel impulse responses were collected continuously during the experiments.

Figure 4.4 shows the trajectories of Target 1 (green) and Target 2 (yellow) for each of the two UE positions. For these experiments, a vertically polarized standard horn with 3 dB-BW of 60° in azimuth and elevation antennas was used at gNB, which was oriented Southward (North is up). Complex channel impulse responses were measured and were recorded every 1 ms.

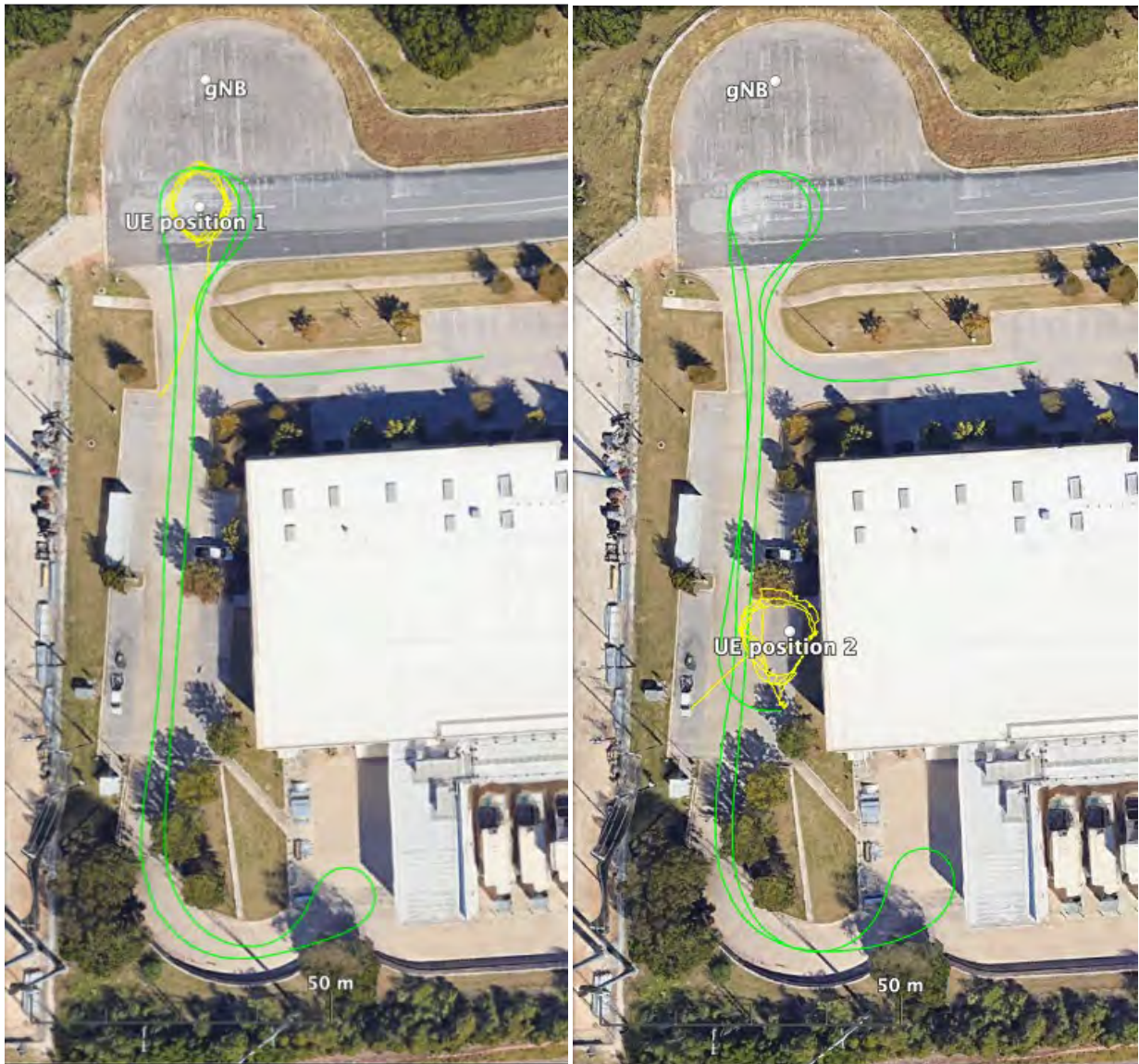


Figure 4.4: Vehicle and Pedestrian Track for UE Position 1 (left) and UE Position 2 (right). Vehicle Track is Shown in Green and Pedestrian Track is Shown in Yellow

#### 4.1.3. Measurement Campaigns

The following two tables summarize the measurement campaigns that were conducted by NIST and AT&T, respectively, to characterize the target models.

Table 4.1: NIST Target Measurement Campaigns

Target Class	Target	Photo	Dims.	Tx-Rx-target configurations	Channel capture
Human Walking (bistatic)	Human A / B / C		157 cm tall female / 165 cm tall male / 185 cm tall male	27 total configurations: - 9 per human • Rx fixed while human walking towards Tx Tx positioned at 9 different bistatic angles around semicircle (22.5° spacing)	<ul style="list-style-type: none"> <li>• 2,000 channel captures per configuration</li> <li>• Sample interval between captures was 2.6 ms, for a total 5.2 s observation period per walk</li> </ul>
Human Gesturing (monostatic)	Human A / B / D / E		157 cm tall female / 165 cm tall male / 168 cm tall female / 179 cm tall male	80 total configurations: - 20 configurations per human • 16 hand motions (two hands moving independently in four directions) • 4 body motions (standing up, sitting down, etc.)	<ul style="list-style-type: none"> <li>• 1,500 channel captures per configuration</li> <li>• Sample interval between captures was 2.6 ms, for a total 3.9 s observation period per gesture</li> </ul>
Human Breathing (monostatic)	Human single B / C / D		(see above)	50 total configurations: + 27 single human configurations: - 9 per human: • 3 positions: sitting, standing, lying down • 3 orientations: front, side, back + 18 pairwise human configurations	<ul style="list-style-type: none"> <li>• 2,000 channel captures per configuration</li> <li>• Sample interval between captures was 26 ms, for a total 52 s observation period</li> </ul>
	Human pairwise B & C (shown) \ B & D \ C & D				
Vehicles (bistatic)	Vehicle A		4.9m wide	1,344 total configurations: - 448 per vehicle + 8 Rx positions around vehicle (45° spacing) • 56 large-scale Tx positions per Rx positions, while Tx moving on a robot around the vehicle at center	<ul style="list-style-type: none"> <li>• 20 channel captures per configuration</li> <li>• Sample interval between captures was 26 ms, for a total 0.52 s observation period per large-scale Tx position</li> </ul>
	Vehicle B		4.8m wide		
	Vehicle C		5.9m wide		
Miscellaneous targets (bistatic)	Drone		1m wide	180 total configurations: - 270 per target • Rx fixed while target on rotator • Target rotated at 30 different angles • Tx positioned at 9 different bistatic angles	<ul style="list-style-type: none"> <li>• 37 channel captures per configuration</li> <li>• Sample interval between captures was 2.6 ms, for a total 96.2 ms observation period per configuration</li> </ul>
	Robot base		1.2m wide		

	Robot arm		0.65m wide	around semicircle (22.5° spacing) with target at center	
--	-----------	---	------------	---	--

Table 4.2: AT&T Target Measurement Campaign

Target Class	Target	Photo	Dims.	Tx-Rx-target configurations	Channel capture
Human walking (bistatic and monostatic)	Human A		172cm	Continuously varying target orientation over multiple paths and multiple BSs and UE locations over 2 frequency bands (6.7 GHz, 28 GHz)	Continuous capture every 1.25 ms over 10min
Vehicles (bistatic and monostatic)	Vehicle A		180" L x 72" W x 72" H	Continuously varying target orientation over multiple paths and multiple BSs and UE locations over 2 frequency bands (6.7GHz, 28GHz)	Continuous capture every 1.25 ms over 10 mins

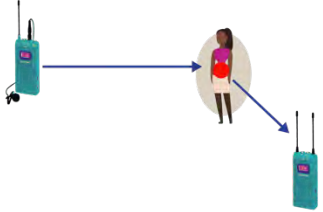
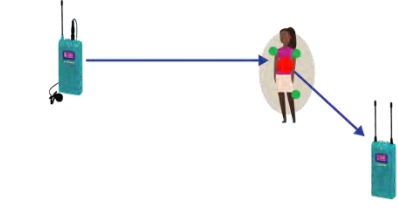
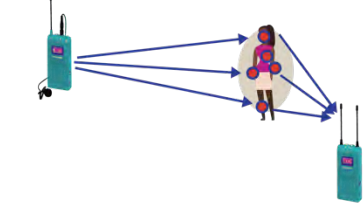
## 4.2. Target Models

The 3GPP TR 22.837 [1] document proposes a host of use cases for sensing applications, capturing a wide range of targets (e.g., humans, animals, vehicles, UAVs, robots, etc.). The spatial-temporal consistency requirement of the target model will depend on the level of abstraction that is sufficient for the performance evaluation of a specific use case and the intended application of the channel model. Consider, for instance, the sensing applications (e.g., intruder detection); here, a target model represented as a single target might suffice because these applications render a binary decision of present or absent. However, to identify the intruder (e.g., animal or human) and also evaluate mmWave signal processing techniques to detect and classify different human activities, a more complex RF signature may be required. Given the high angle-delay resolution in the mmWave and sub-THz bands, multiple scatter centers (and corresponding rays) from the same target may indeed be resolvable. As such, in this subsection we propose three target models, shown in Table 4.3, with different levels of complexity.

The single-ray target model focuses on detection of the target: Is it there or not? Thus it is sufficient to represent the target as a single-ray. The stochastic cluster target model of use cases focuses on classification of the target: – Is it a human or a vehicle? Thus cluster definition is required. For example, the target’s dimensions (and in turn the cluster’s dimensions) and the target’s rigidity (whether the distribution of the rays around the clusterhead changes) matter, even though how the rays are distributed around the clusterhead does not. The quasi-deterministic cluster model third focuses on classifying the target motion: Which hand gesture for enhanced reality applications (swiping up/down/left right)? Which class of motion for sports monitoring (running, jumping, etc.)? Thus the rays within the cluster cannot be

distributed randomly; rather some or all the rays within the cluster must have deterministic spatial-temporal consistency.

Table 4.3: Target Models and Associated 3GPP Use Cases [1]

 <p><b>Single-Ray Target Model</b> Use cases: 5.1 Intruder detection in smart home 5.2 Pedestrian/animal intrusion detection on highway 5.6 Intruder detection outside smart home 5.7 Railway intruder detection</p>	 <p><b>Stochastic Cluster Target Model</b> Use cases: 5.9 AGV detection 5.10 UAV intrusion detection 5.22 UAV/vehicle/pedestrian detection near Smart Grid 5.25 Immersive experience based on sensing</p>	 <p><b>Quasi-Deterministic Cluster Target Model</b> Use cases: 5.24 Sports monitoring 5.27 Public safety search and rescue 5.29 Gesture recognition</p>
---	--	--

\*Indexing of use cases in the table are in reference to [1].

#### 4.2.1. Geometry of Target Links

A target can be approximated electromagnetically by the  $M_{tg}$  geometrical scatter centers that contribute most significantly to the total scattering from the target, thereby delineating the shape and the dimension of the target. The generic geometry of a target link is depicted in Figure 4.5, whereby the  $M_{tg}$  scatter centers are indexed through  $m$ . Each scatter center acts as a point source when illuminated by the transmit signal. The figure shows the geometry of the corresponding  $m$ th ray from the Tx to the tg and from the tg to the Rx, where tg denotes the target. A generic ISAC system configuration will consider Tx and Rx at positions  $(x_{Tx}, y_{Tx}, z_{Tx})$  and  $(x_{Rx}, y_{Rx}, z_{Rx})$ , respectively (i.e., in a bistatic configuration, where the monostatic configuration can be considered a special case).

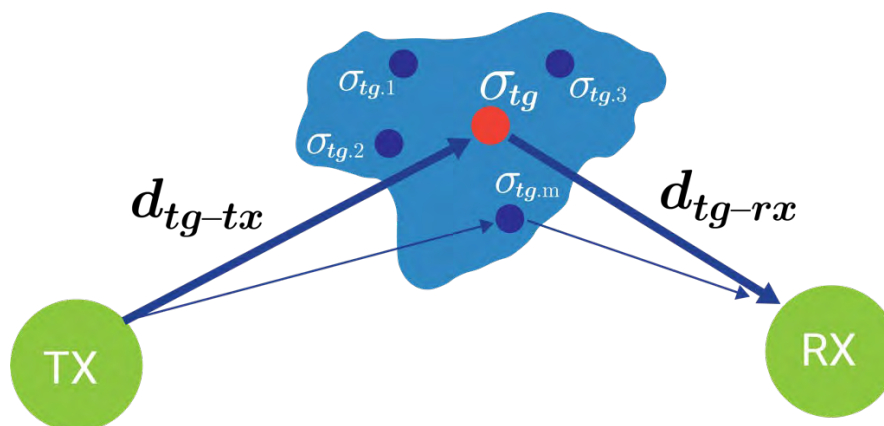


Figure 4.5: Generic Geometry of an ISAC Link

Let  $(x_{tg,m}(t), y_{tg,m}(t), z_{tg,m}(t))$  denote the 3D coordinates of the  $m$ th scatter center at time  $t$ , assuming the target is mobile. The delay of the  $m$ th ray is computed as:

$$\tau_{tg,m}(t) = \frac{d_{Tx-tg,m}(t) + d_{tg,m-Rx}(t)}{c}, \quad (4.2.1)$$

where  $d_{Tx-tg,m}(t)$  is the distance between the Tx and the  $m$ th center,  $d_{tg,m-Rx}(t)$  is the distance between the  $m$ th center and the Rx, and  $c$  is the speed of light.

The  $m$ th ray's 3D azimuth AoD and zenith angle of departure (ZoD) from the Tx is denoted by  $\phi_{tg,m,AoD}(t)$  and  $\theta_{tg,m,ZoD}(t)$ , respectively, which are computed as:

$$\phi_{tg,m,AoD}(t) = \text{atan2}(y_{tg,m}(t) - y_{Tx}, x_{tg,m}(t) - x_{Tx}). \quad (4.2.2)$$

$$\theta_{tg,m,ZoD}(t) = \text{acos}\left(\frac{z_{tg,m}(t) - z_{Tx}}{d_{Tx-tg,m}(t)}\right). \quad (4.2.3)$$

Analogously, the  $m$ th ray's 3D azimuth AoA and ZoA to the Rx is denoted by  $\phi_{tg,m,AoA}(t)$  and  $\theta_{tg,m,ZoA}(t)$ , respectively, which are computed as:

$$\phi_{tg,m,AoA}(t) = \text{atan2}(y_{Rx} - y_{tg,m}(t), x_{Rx} - x_{tg,m}(t)). \quad (4.2.4)$$

$$\theta_{tg,m,ZoA}(t) = \text{acos}\left(\frac{z_{Rx} - z_{tg,m}(t)}{d_{tg,m-Rx}(t)}\right). \quad (4.2.5)$$

The path gain of the  $m$ th ray, in addition to bistatic free-space propagation loss, includes the RCS, which is a measure of how much energy is scattered by the target in the direction of the Rx. The RCS depends on the target shape, dimension, and reflectivity, as well as the incident angle of the ray on the target. Assuming unitary transmit power and unitary Tx and Rx antenna gains, the  $m$ th ray's path gain is computed as:

$$PG_{tg,m}(t) = \frac{\sigma_{tg,m}(t)c^2}{(4\pi)^3 f_c^2 d_{Tx-tg,m}^2(t) d_{tg,m-Rx}^2(t)}, \quad (4.2.6)$$

where  $\sigma_{tg,m}(t)$  is the bistatic RCS expressed in units of (m<sup>2</sup>) and  $f_c$  is the center frequency of operation.

#### 4.2.2. Single-ray Model

In this section we describe an extension of 38.901, introducing the notion of a single-ray target. The single-ray target model is a simplified model that characterizes the total power scattered by a target, enabling simulation of ISAC systems to study sensing tasks and evaluate statistical sensing metrics, such as false alarm rate and successful detection rate.

Usual sensing targets are extended objects (i.e., entities that cannot be electromagnetically reduced to a mere ray due to their composition of different materials and their irregular, extended shapes, such as human bodies). As a result, a single-ray target cannot describe the scattered field from the object. Instead, it describes the composite echo, which is the sum of the scattered field from the object.

Assuming the target can be represented as a single scatter center, and defining  $d_{tg-Tx}$  the distance between the target and the Tx, and a  $d_{tg-Rx}$  the distance between the target and the Rx (as shown in Figure 4.6), the total received scattered power can be expressed as follows:

$$PG_{tg}(t) = \frac{\sigma_{tg}(t)c^2}{(4\pi)^3 f_c^2 d_{tx-tg}^2(t) d_{tg-rx}^2(t)}, \quad (4.2.7)$$

where the term  $\sigma_{tg} = \sum_m \sigma_{tg,m}(t)$  represents the composite RCS and fully characterizes the proposed model. Practically,  $\sigma_{tg}$  models the visibility of a target in the ISAC system, representing the equivalent area that would scatter energy to the Rx.

The RCS value may depend on the geometry of the system and the target, including their relative position and orientation. Measurements conducted with different geometries have been aggregated to reduce a general model, valid independently of the simulated configuration.

The single-ray target model is derived from the measurements by identifying the scattering center of the target. The scattering center is conceptualized as the ray that most accurately represents where most of the signal is scattered to the Rx. Hence, to determine the ray properties, RMS delay, RMS AoA, and RMS ZoA have been used.

Once the scatter center is determined, the distances  $d_{tg-Tx}$  and  $d_{tg-Rx}$  are inferred from the measurements by assuming a single bounce ray. The observed delay outlines the range ellipsoid, indicating the ray's potential origin. The AoA and ZoA, combined with the orientations of the Tx and Rx, enables determination of the direction from which the signal arrives at the Rx, from which the accurate scattering point and distances are computed, as shown in Figure 4.6.

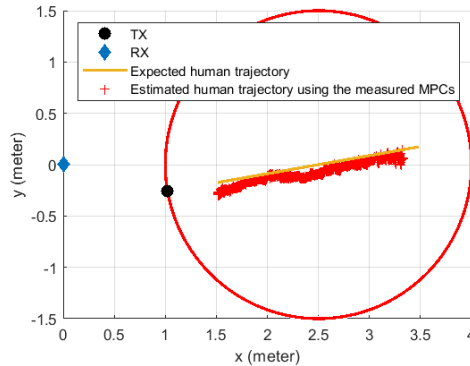


Figure 4.6: Scattering Center Estimates

Using the Human walking target class data in Table 4.1 (18,395 points available for fitting), the probability density function of the estimated  $\sigma_{tg}$  is illustrated in Figure 4.7, comparing Humans A, B, and C. The probability density function of  $\sigma_{tg}$  in  $m^2$  - aligns with a Gamma distribution described by:

$$f_{\sigma_{tg}}(x, \mu, \omega) = \frac{1}{\Gamma(\mu)\omega^\mu} x^{\mu-1} \exp(-x/\omega), \quad (4.2.8)$$

where  $\Gamma(\mu)$  is the gamma function, the shape parameter  $\mu$ , and scale parameter  $\omega$  reduced from the measurements are reported in Table 4.4 for different subjects with different body heights. This analysis supports the hypothesis that a single-ray target model can effectively model the visibility of a target in ISAC systems. The median  $\sigma_{tg}$  for Humans A, B, and C is -21.3 dBsm, -16.7 dBsm, and -14.9 dBsm, respectively. The estimated  $\sigma_{tg}$  increases with the height of the target and in turn the target's body area, quantifying the effective area that scatters electromagnetic power into the Rx. We denote the effective area to differentiate it from the total area: The body is not flat and so not all of the power that is incident on the body will be scattered back into the Rx.

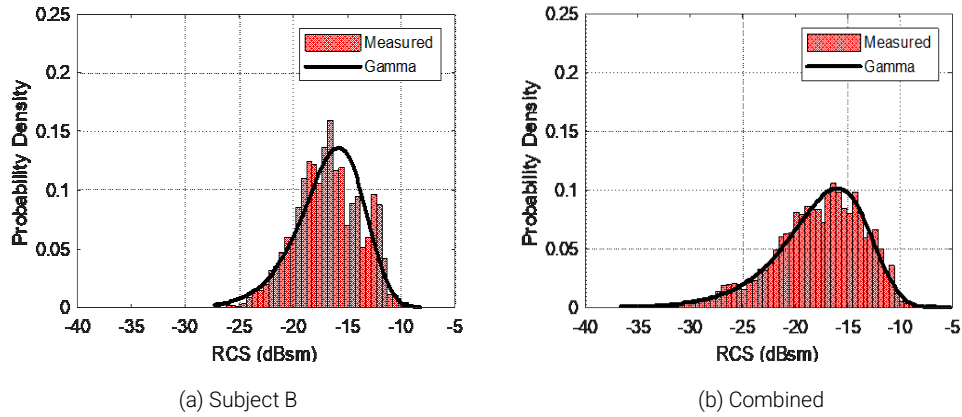


Figure 4.7:  $f_{\sigma_{tg}}$  for Human B and for all Humans Combined (A, B, and C)

Table 4.4: RCS Model Parameters

Subject:	A (1.57 m)	B (1.65 m)	C (1.85 m)	Combined
$\mu$	1.67	2.35	2.49	1.37
$\omega$	0.005	0.011	0.015	0.018

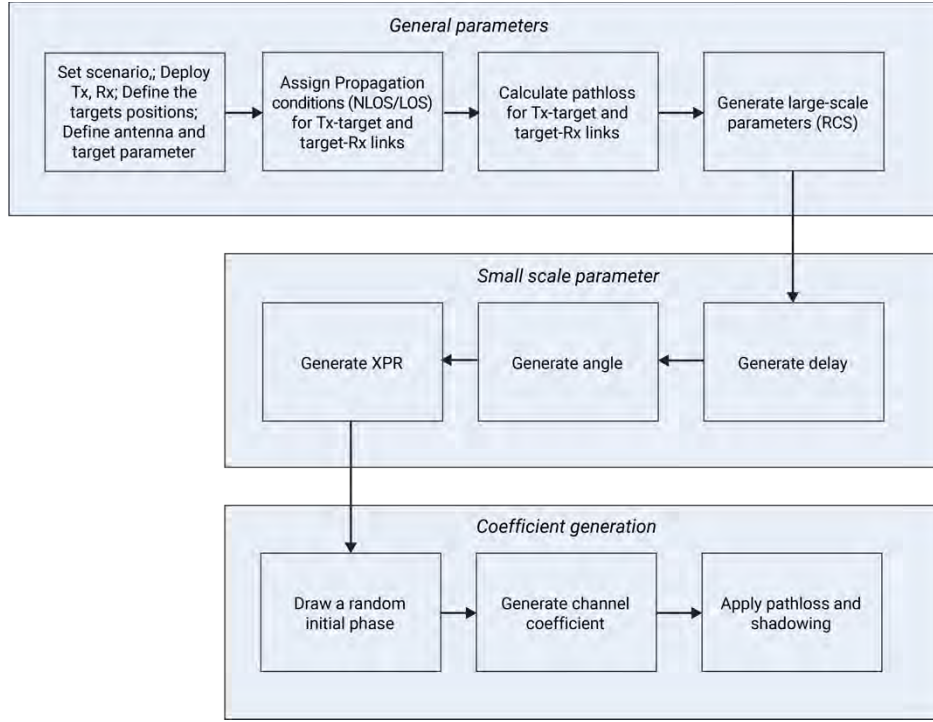


Figure 4.8: Single-ray Target Model Channel Coefficient Generation Procedure

Within the TR 38.901 framework, a new step to generate RCS according to equation 4.2.8 may be added to incorporate the RCS of a target in existing PL model. To generate the single-ray target channel coefficient, the following steps, summarized in Figure 4.8, may be followed:

- 1) Generate the network layout, including Tx, Rx, target position and coefficient ( $\mu$  and  $\omega$ ).
- 2) Assign the propagation conditions for the Tx-target and target-Rx links based on the NLOS/LOS propagation probabilities defined in the environment.
- 3) Calculate the PL  $PL_{tg-tx}$  for the Tx-target and  $PL_{tg-rx}$  target-Rx links according to step 2. The distances  $d_{tg-tx}$  and  $d_{tg-rx}$  can be inferred from the position of target, Tx and Rx defined in step 1.
- 4) Generate the composite RCS using the pdf  $f_{\sigma_{tg}}(\mu, \omega)$ .
- 5) Compute the delay based on geometry.
- 6) Compute angle based on geometry.
- 7) Generate XPR.
- 8) Draw random initial phase of the ray.
- 9) Generate channel coefficient.
- 10) Apply pathloss and RCS such that  $PL = PL_{tg-tx} + PL_{tg-rx} - \sigma_{tg} - 10 \log_{10}(4\pi/\lambda^2)$ .

#### 4.2.2.1. Fading Single-ray Target Model

The backscattering cross-section  $\sigma_{\text{back}}(t)$  is generally fluctuating in time both due to changes in target orientation and the relative motion of different target components, sometimes termed “micro-Doppler,” particularly relevant in targets

with time-varying shape, such as people in motion. A simple way to represent such fluctuations is through Swerling models [21], developed in traditional radar applications, with target backscattering radar cross-section  $\sigma_{\text{back}}(t)$  a stochastic process in time:

$$\begin{aligned}\sigma_{\text{back}}(t) &= \sigma_o |\xi(t)|^2, \\ \sigma_o &= A_{\text{geom}} \gamma \\ \xi(t) &\sim CN(0,1)\end{aligned}\tag{4.2.2.1}$$

Where the average target cross-section  $\sigma_o$  is a product of target geometric cross-sectional area  $A_{\text{geom}}$  and a loss factor  $\gamma$  representing, for example, reflection loss from a human body. For example,  $\sigma_o$  has been reported (in decibels) as -8 dBsm [22] for a person. In the Swerling I model, the scattered field fluctuation  $\xi(t)$  is assumed to follow a complex Gaussian distribution, whose relative power  $|\xi(t)|^2$  is, thus, exponentially distributed. This is a common assumption for arrivals consisting of many multipaths (from different target parts) with time-varying relative phases. The rate of target backscatter time fluctuation is determined by relative motion of body parts and can be obtained from measured Doppler spectrum studies. Here it is estimated using general considerations: for an assumed relative limb speed of  $v_{\text{target}} = 0.1$  m/s, the maximum Doppler frequency  $f_{\text{v}_{\text{target}}/c} \sim 10$  Hz at  $f = 28$  GHz, with coherence time scale of  $\sim 0.1$  sec. The fluctuation  $\xi(t)$  can be simulated by convolving a white noise sequence with a filter (e.g., of Gaussian shape) with characteristic width of 0.1 sec. Alternative target models may involve other distributions, including lognormal, as found effective for clutter backscatter in Section 6 for clutter return model or a Gamma distribution, as in previous section.

#### 4.2.3. Stochastic Cluster Model

This section presents an extension of the single-ray target model to a cluster target model. Unlike the single-ray model, the cluster model defines the shape of the target and can be used for classification. This is because different targets (e.g., human and vehicle) would lead to varying cluster sizes.

The single cluster target model is an extension of the single-ray target model, which can better represent the signal propagations related to the target when the target is close to the Tx and the Rx. In addition, the spreading of the rays within the cluster can potentially be used to describe the size and shape of the target, which can support the evaluation of the applications that require more information than just the position and speed of the target.

The channel realization workflow can be described as follows:

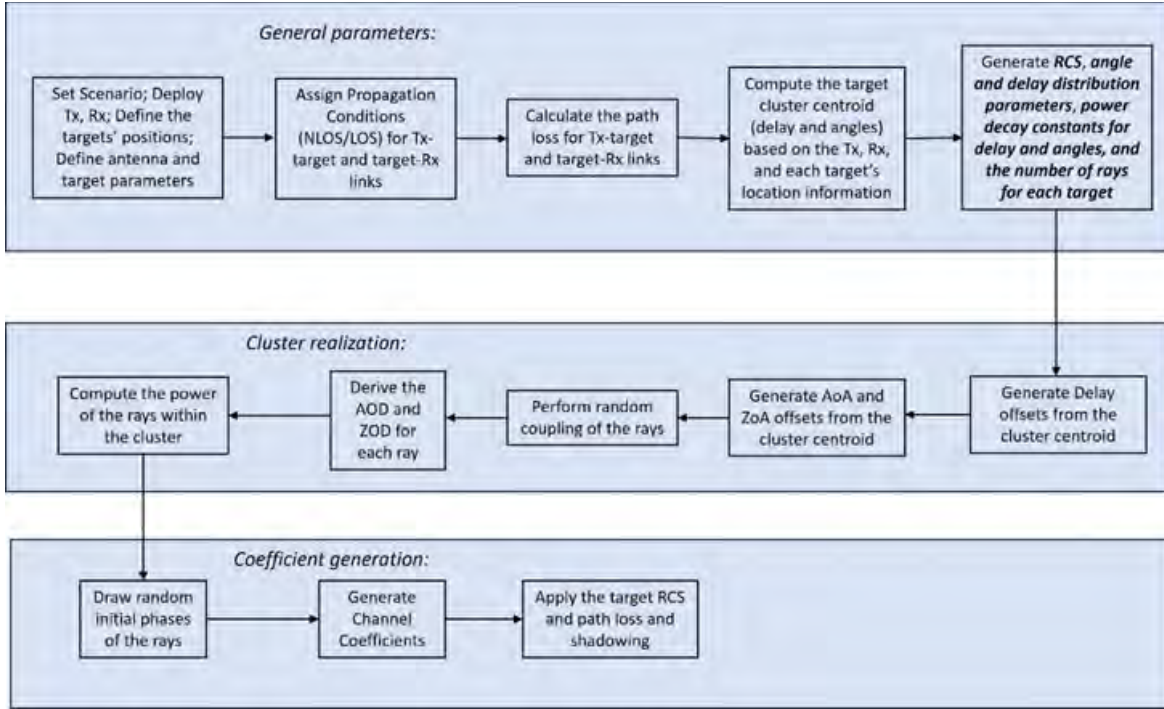


Figure 4.9: Single-Cluster Model Channel Coefficient Generation Procedure

The steps to realize the stochastic cluster target model are detailed as:

- 1) Define the simulation scenario (e.g., indoor office, street canyon), deploy the Tx, Rx, and targets in the environment, and define the antenna parameters and the targets' type and the corresponding parameters.
- 2) Assign the propagation conditions for the Tx-target and target-Rx links based on the NLOS/LOS propagation probabilities defined in the environment.
- 3) Calculate the PL for the Tx-target and target-Rx links.
- 4) Compute the target cluster head in terms of delay, AoA, ZoA, AoD, and ZoD based on the locations of the Tx, Rx, and the geometry center of the target.
- 5) Generate the cluster composite RCS value, delay offset, AoA offset, and ZoA offset distribution functions. Generate the ray RCS decay constants for the delay, AoA, and ZoA, respectively. Generate the number of rays for the stochastic target cluster.
- 6) Generate the delay offset of each ray relative to the clusterhead based on the delay offset distribution function.
- 7) Generate the AoA and ZoA offsets of each ray relative to the clusterhead based on the AoA offset and ZoA offset distribution functions.
- 8) Perform random coupling of the delay, AoA, and ZoA parameters.
- 9) Based on the AoA, ZoA, and delay, derive the AoD and ZoD of each ray.
- 10) Compute the relative RCS value of each ray based on the intra-cluster RCS decay constants and the relative delay offsets, AoA offsets, and ZoA offsets of the intra-cluster rays. For example, the RCS value of the  $m$ th ray can be computed as  $\sigma_m = \exp\left(\frac{-|\tau_m|}{\gamma_\tau}\right) \exp\left(\frac{-|\alpha_{m,AOA}|}{\gamma_{AOA}}\right) \exp\left(\frac{-|\alpha_{m,ZOA}|}{\gamma_{ZOA}}\right)$ , where  $\tau_m$ ,  $\alpha_{m,AOA}$ , and  $\alpha_{m,ZOA}$  are the delay offset, AoA offset, and ZoA offset of the  $m$ th ray, respectively, and

$\gamma_r$ ,  $\gamma_{AOA}$ , and  $\gamma_{ZOA}$  are their corresponding RCS decay constants. Note that the received power of each ray is directional proportional to its RCS value.

- 11) Draw random initial phases of each ray.
- 12) Generate the channel coefficients.
- 13) Calculate the cluster power based on the PL, shadowing, and cluster composite RCS value. Scale the power of each ray so that the sum power is equal to the computed cluster power.

#### 4.2.3.1. Model Parameters for Stochastic Cluster Target Model

- Number of rays  $M_{tg}$  in a cluster:

The number of rays, denoted by  $M_{tg}$ , within a cluster predominantly hinges on the target's dimensions. The larger the target's size, the greater the number of rays it is likely to reflect. To model this parameter, measurements conducted with different geometries have been aggregated for each human subject. Following the data analysis (18395 points available for fitting) as shown in Figure 4.10, the probability density function of  $M_{tg}$  aligns with a Nakagami distribution described by:

$$f_{M_{tg}}(x, \mu, \omega) = 2 \left(\frac{\mu}{\omega}\right)^\mu \frac{1}{\Gamma(\mu)} x^{(2\mu-1)} \exp\left(-\frac{\mu}{\omega} x^2\right). \quad (4.2.9)$$

The shape parameter  $\mu$  and scale parameter  $\omega$  reduced from the measurements are reported in Table 4.5 for different human subjects with different body heights.

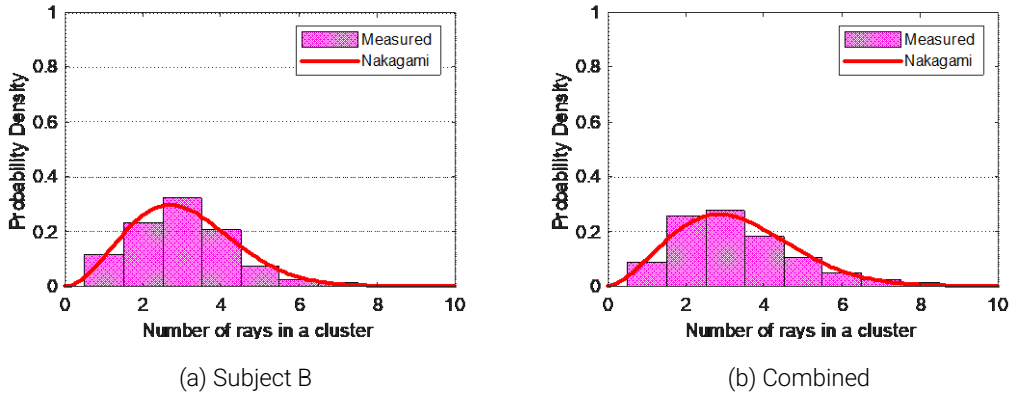


Figure 4.10: Number of Rays Modeling in a Cluster

Table 4.5: Number of Rays Model Parameters

Subject:	A (1.57 m)	B (1.65 m)	C (1.85 m)	Combined
$\mu$	3.09	1.41	1.41	1.29
$\omega$	5.75	11.14	19.27	13.21

The median  $M_{tg}$  for subjects A, B, and C is 2, 3, and 4, respectively. These values clearly indicate that the number of rays in a cluster originated from the target increases with the size of the target's body.

- Azimuth AoA Offset

The AoA offset, denoted by  $\Delta\phi_{tg,m,AOA}(t)$ ,  $m = 1, 2, \dots, M_{tg}$ , describes the absolute change in AoA with respect to clusterhead. This parameter is defined as  $\Delta\phi_{tg,m,AOA}(t) = \phi_{tg,m,AOA}(t) - \mu_{\phi_{tg,AOA}(t)}$ , where the AoA of the clusterhead is defined as the power weighted mean angle as shown below,

$$\mu_{\phi_{tg,AOA}(t)} = \arg \left\{ \sum_{m=1}^{M_{tg}} \exp(j\phi_{tg,m,AOA}(t)) \sigma_{tg,m}(t) \right\} \quad (4.2.10)$$

where  $M_{tg}$  denotes the total number of rays reflected back from the target,  $\phi_{tg,m,AOA}(t)$  and  $\sigma_{tg,m}(t)$  represent AoA and RCS of the  $m$ th ray, respectively. To model this parameter, we aggregated measured data for each human subject and calculated  $\Delta\phi_{tg,m,AOA}(t)$  for each ray per time instant. Following the data analysis as shown in Figure 4.11, the probability density function of  $\Delta\phi_{tg,m,AOA}(t)$  aligns with a Laplacian distribution described by:

$$f_{\Delta\phi_{tg,m,AOA}(t)}(x, \mu, b) = \frac{1}{2b} \exp\left(\frac{-\text{abs}(x - \mu)}{b}\right) \quad (4.2.11)$$

The location parameter  $\mu$  and scale parameter  $b$  reduced from the measurements (approximately 47,000 data points across all three subjects) are reported in Table 4.6.

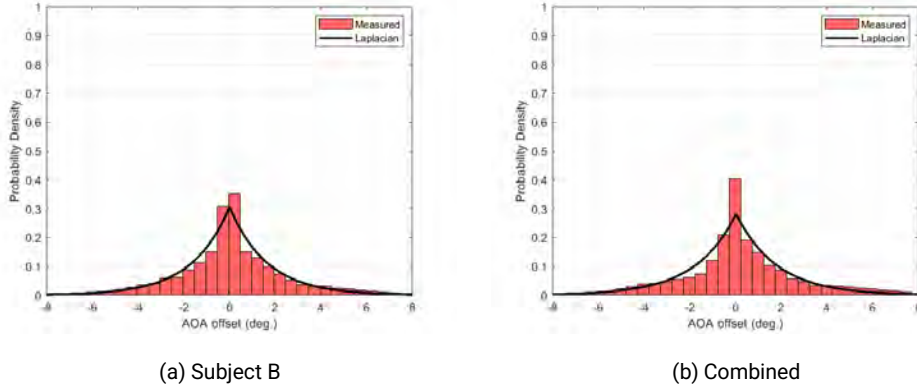


Figure 4.11: AoA Offset Modeling in a Cluster

Table 4.6: AoA Offset Model Parameters

Subject:	A (1.57 m)	B (1.65 m)	C (1.85 m)	Combined
$\mu$	0.018	0.005	0.073	0.031
$b$	1.15	1.63	2.087	1.77

- Zenith ZoA Offset

The ZoA offset, denoted by  $\Delta\theta_{tg,m,ZoA}(t)$ ,  $m = 1, 2, \dots, M_{tg}$ , describes the absolute change in ZoA with respect to clusterhead. This parameter is defined as  $\Delta\theta_{tg,k,ZoA}(t) = \theta_{tg,m,ZoA}(t) - \mu_{\theta_{tg,ZoA}(t)}$ , where the ZoA of the clusterhead is defined as the power weighted mean angle as shown below,

$$\mu_{\theta_{tg,ZoA}(t)} = \arg \left\{ \sum_{m=1}^{M_{tg}} \exp(j \theta_{tg,m,ZoA}(t)) \sigma_{tg,m}(t) \right\} \quad (4.2.12)$$

where  $\theta_{tg,m,ZoA}(t)$  represents ZoA of the  $m$ th ray reflected from the target. Similar to AoA offset, ZoA offset also follows a Laplacian distribution that can be clearly seen in Figure 4.12. The Laplacian distribution parameters  $\mu$  and  $b$  reduced from the measurements are reported in Table 4.7.

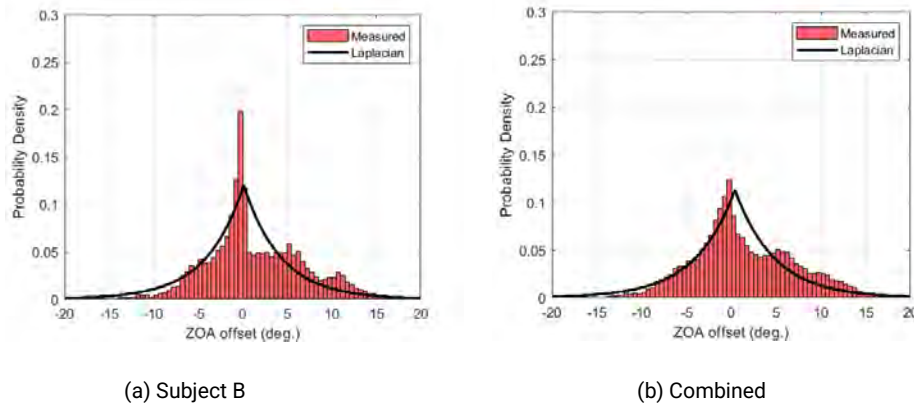


Figure 4.12: ZoA Offset Modeling in a Cluster

Table 4.7: ZoA Offset Model Parameters

Subject:	A (1.57 m)	B (1.65 m)	C (1.85 m)	Combined
$\mu$	0.095	0.11	0.44	0.41
$b$	4.98	4.16	4.36	4.42

- Delay Offset

The delay offset, denoted by  $\Delta\tau_{tg,m}(t)$ ,  $m = 1, 2, \dots, M_{tg}$ , describes the absolute change in delay with respect to the clusterhead. This parameter is defined as  $\Delta\tau_{tg,m}(t) = \tau_{tg,m}(t) - \mu_{\tau_{tg}(t)}$ , where the mean delay  $\mu_{\tau_{tg}(t)}$  of the clusterhead is defined as:

$$\mu_{\tau_{tg}(t)} = \frac{\sum_{m=1}^{M_{tg}} \tau_{tg,m}(t) \sigma_{tg,m}(t)}{\sum_{m=1}^{M_{tg}} \sigma_{tg,m}(t)} \quad (4.2.13)$$

where  $\tau_{tg,m}(t)$  represents delay of the  $m$ th ray reflected from the target. Similar to AoA and ZoA offsets, delay offset also follows a Laplacian distribution, which can be observed in Figure 4.13. The Laplacian distribution parameters  $\mu$  and  $b$  reduced from the measurements are reported in Table 4.8.

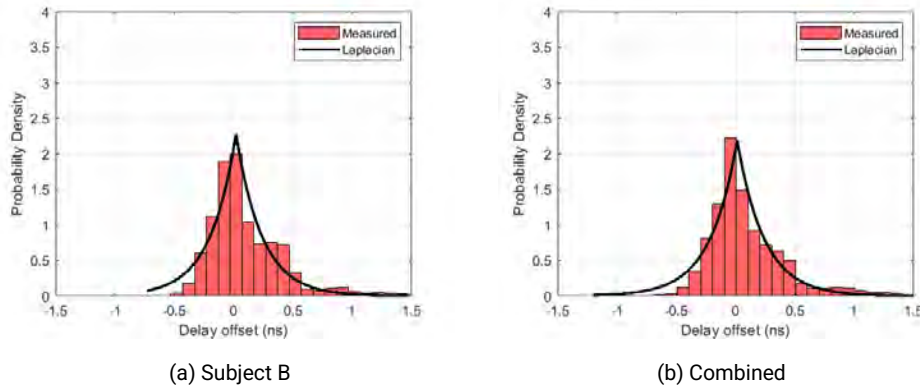


Figure 4.13: Delay Offset Modeling in a Cluster

Table 4.8: Delay Offset Model Parameters

Subject:	A (1.57 m)	B (1.65 m)	C (1.85 m)	Combined
$\mu$	0.095	0.0008	0.020	0.012
$b$	0.20	0.22	0.29	0.22

- Power Decay Constants vs. AoA, ZoA, and Delay Offsets

The power decay constants quantify how the power of a ray varies with respect delay, AoA, and ZoA of the clusterhead. These parameters are defined as the power delay decay constant ( $\gamma_\tau$ ), the power AoA decay constant ( $\gamma_{AoA}$ ), and the power ZoA decay constant ( $\gamma_{ZoA}$ ).

Figure 4.14 demonstrates the variation of relative RCS with respect to delay offset and AoA offset. It can be observed that the RCS relative to the clusterhead decreases as the delay or AoA offset increases. These parameters are reported in the Table 4.9 for all three subjects.

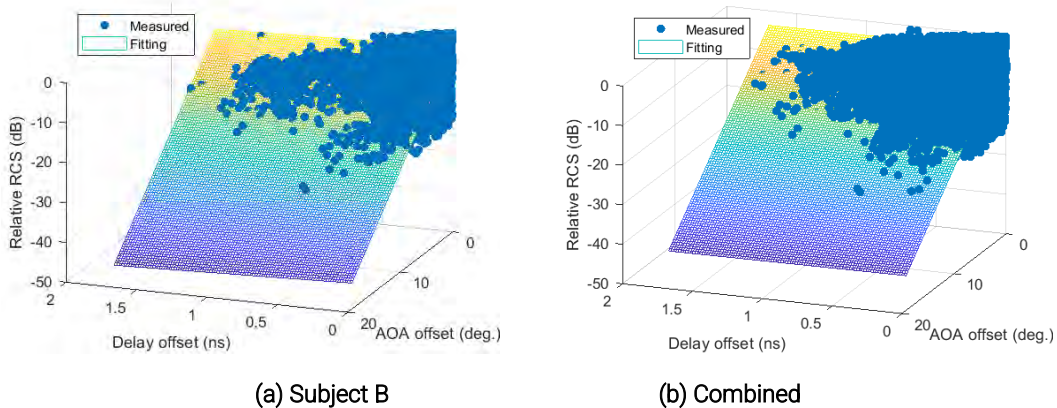


Figure 4.14: Normalized Power Variation with Respect to Delay and AoA Offsets

Table 4.9: Power Decay Constant Model Parameters for Delay, AoA, and ZoA Offsets

Subject:	A (1.57 m)	B (1.65 m)	C (1.85 m)	Combined
$\gamma_r$	1.0526	0.9091	0.3717	0.9346
$\gamma_{AOA}$	0.7812	0.7194	0.9259	0.7576
$\gamma_{ZOA}$	1.5152	1.6667	1.7544	1.7857

#### 4.2.4. Quasi-Deterministic Cluster Model

The previously discussed target models offer a statistical description of the target, focusing on total power considerations (Single-ray Target Model in Section 4.2.2) and a combination of power and geometrical distributions (Stochastic Cluster Target Model in Section 4.2.3). However, these models may fall short in applications that require or benefit from high-resolution RF signatures. For instance, the classification of human gestures represents an application where these models might not provide adequate details because the stochastic realization of the target channel might lack sufficient realism. For designing and simulating algorithms aimed at recognizing human gestures or in general other high-resolution tasks, a more detailed model that incorporates realistic temporal and spatial correlation of multiple scattering rays is needed.

A flexible quasi-deterministic cluster target model allows for closely representing the RF signatures of moving targets by describing the spatial and temporal evolution of multiple scattering centers in the delay, angle, and power domains. While the description is left generic to multiple scattering centers, the single scatter center scenario may be considered as a special case.

As in the cluster target model, the target is described as a cluster (i.e., a collection of dominant rays). The dominant rays are where most of the signal scattering occurs, providing a detailed profile of the target. In contrast to the stochastic cluster target model in Section 4.2.3, all the rays of the cluster are described geometrically (in angle and in delay). To maintain the scalability of the model and reduce the quantization error arising from the discrete scattering approximation while capturing complex electromagnetic phenomena (e.g., diffuse reflections caused by irregular surfaces and diffraction), the model is complemented with a stochastic component. The Autocorrelation Function (ACF) is provided to represent any offset (in the angle, delay, and path-gain domains) of the discrete scattering approximation from the measurements, offering the capability to integrate the deterministic component with a temporal correlated stochastic component. This model allows for a complete representation of the target response that captures both the predictable aspect of the RF signature and the uncertainties and deviation from the expect signature.

##### 4.2.4.1. Deterministic Model Component

A set of keypoints, defined through geometric description, can capture complex patterns, including human activities such as hand gesturing or walking. For many targets, biomechanical models describing their motion exist in literature. For instance, human motion can be described with kinematic models such as the Boulic model [9], which is a collection of keypoints describing the trajectories of different body parts when walking. Geometrical models allows to realize a

channel with 1) spatial correlation among different keypoints and 2) temporal correlation when the keypoints move over time. Besides walking, other models may be introduced to incorporate additional human activities, such as gesturing and falling, or to simulate the dynamics of different targets, such as vehicles, animals, and robots.

The target channel is modelled through a collection of keypoints indexed through  $m$ , each representing a distinct scattering center of the target. Each keypoint generates a single-ray as illustrated in Figure 4.15.

The geometrical parameter for each ray can be derived using the equations presented for the single-ray target model in Section 4.2.1. Similarly, the electromagnetic parameters, specifically the RCS, can be derived following the same methodology presented for the single-ray target model. In contrast to the single-ray target model, the collected measurements were not aggregated. Instead, a classification of the model predictive control was conducted [13] to identify the target's dominant scattering points. Hence, the procedure presented in Section 4.2.1 was applied for each keypoint class. However, in this subsection, we applied the Human gesturing data from Table 4.10, including Humans A, B, D, and E. Table 4.10 lists the values of the RCS estimate for each class of keypoint for four different subjects.

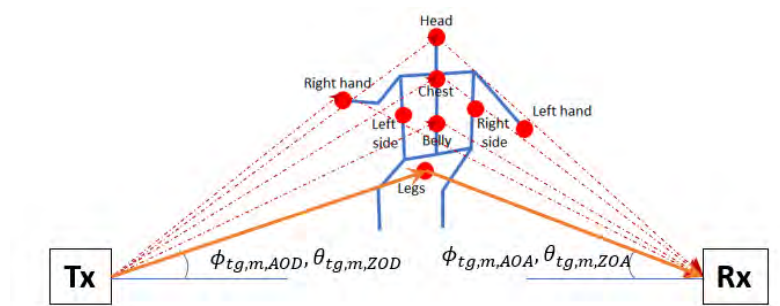


Figure 4.15: Geometry of Target Channel Defined by a Tx, an Rx, and a Collection of Keypoints. Each keypoint represents a dominant scatter center of the target, as identified from the context-aware systems of the NIST 28 GHz channel sounder [13]

#### 4.2.4.2. Stochastic Model Component

The gross body motion (e.g., walking, gesturing) is represented through the keypoints of the deterministic component of the model, ensuring spatial and temporal consistency. Keypoints, however, are used to represent point scatterers, and so will not always well represent non-flat and intricate surfaces that make up body parts and in general complex targets. Additionally, the keypoint is only an approximation of the scatter center, which can result in slight differences in angle, delay, and power when compared to actual measurements.

To overcome limitations, offsets between the measured multipaths and the keypoints are modelled stochastically, enhancing accuracy with no significant increase in model complexity. The offset of the  $m$ th keypoint is computed over time  $t$  in the same domain in which the deterministic component of the keypoint is defined – i.e., in path gain, delay, and 3D double-directional angle – and is denoted compactly in vector format as:

$$\mathbf{d}_m(t) = \left[ \partial_{P_{G_{tg,m}}}(t), \partial_{\tau_{tg,m}}(t), \partial_{\phi_{tg,m,AOD}}(t), \partial_{\theta_{tg,m,ZOD}}(t), \partial_{\phi_{tg,m,AOA}}(t), \partial_{\theta_{tg,m,ZOA}}(t) \right].$$

Even if the offsets are modelled stochastically, the measurements indicate that the offsets exhibit significant temporal correlation, as quantified through the ACF. What is more, the ACF was found to be specific to the scenario's geometry

and to the periodic behavior of the motion. To capture this specificity, the ACF of the offsets were computed in the four domains per configuration. Figure 4.16 illustrates the measured ACF of the ZoA offset.

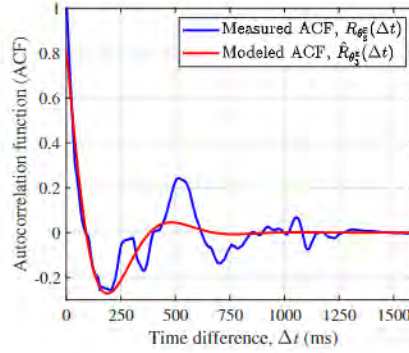


Figure 4.16: Comparison Between Measured ACF and Damped Sinusoid Fit

The ACFs exhibit damped sinusoid behaviour as shown in Figure 4.16 – this was consistent across all ACFs calculated in all domains and across all keypoints and configuration. The autocorrelation is thus described through the following function:

$$R_{\partial_{t,g,m}}(\Delta t) = \exp(-\lambda_{t,g,m} \cdot \Delta t) \cos(\omega_{t,g,m} \cdot \Delta t) \quad (4.2.14)$$

where parameter  $\lambda$  denotes the decay rate in ms<sup>-1</sup> and  $\omega$  denotes the oscillation frequency of in ms<sup>-1</sup>. The process is assumed to be wide-sense stationary, meaning that it depends not on the absolute time  $t$ , but only on the relative time  $\Delta t$  between any two-time instances. Four of the offsets,  $[\partial PG_{t,g,m}(t), \partial \tau_{t,g,m}(t), \partial \phi_{t,g,m,AOA}(t), \partial \theta_{t,g,m,ZOA}(t)]$ , have respective independent ACFs  $[R_{\partial PG_{t,g,m}}(\Delta t), R_{\partial \tau_{t,g,m}}(\Delta t), R_{\partial \phi_{t,g,m,AOA}}(\Delta t), R_{\partial \theta_{t,g,m,ZOA}}(\Delta t)]$  defined by the two parameters each:  $[(\lambda_{PG_{t,g,m}}, \omega_{PG_{t,g,m}}), (\lambda_{\tau_{t,g,m}}, \omega_{\tau_{t,g,m}}), (\lambda_{\phi_{t,g,m,AOA}}, \omega_{\phi_{t,g,m,AOA}}), (\lambda_{\theta_{t,g,m,ZOA}}, \omega_{\theta_{t,g,m,ZOA}})]$ . The other two residuals,  $[\partial \phi_{t,g,m,AOD}(t), \partial \theta_{t,g,m,ZOD}(t)]$ , are dependent on  $[\partial \tau_{t,g,m}(t), \partial \phi_{t,g,m,AOA}(t), \partial \theta_{t,g,m,ZOA}(t)]$  (see [13]) to ensure the geometrical consistency that is described in Section 4.2.1.

With the offsets in hand, the double-directional channel impulse response of the target channel is expressed as

$$\begin{aligned} & h_{t,g}(t, \tau, \phi_{AOD}, \theta_{ZOD}, \phi_{AOA}, \theta_{ZOA}) \\ &= \sum_{m=1}^{M_{tg}} \sqrt{PG_{t,g,m}(t) + \partial PG_{t,g,m}(t) \exp(j\gamma_m) \exp(j2\pi f_c(t - \tau_{t,g,m}(t) - \partial \tau_{t,g,m}(t)))} \\ & \cdot \delta(\tau - \tau_{t,g,m}(t) - \partial \tau_{t,g,m}(t)) \cdot \delta(\phi_{AOD} - \phi_{t,g,m,AOD}(t) - \partial \phi_{t,g,m,AOD}(t)) \\ & \cdot \delta(\theta_{ZOD} - \theta_{t,g,m,ZOD}(t) - \partial \theta_{t,g,m,ZOD}(t)) \cdot \delta(\phi_{AOA} - \phi_{t,g,m,AOA}(t) - \partial \phi_{t,g,m,AOA}(t)) \cdot \delta(\theta_{ZOA} \\ & - \theta_{t,g,m,ZOA}(t) - \partial \theta_{t,g,m,ZOA}(t)) \end{aligned} \quad (4.2.15)$$

where  $f_c$  is the center frequency,  $\gamma_m \sim U[-\pi, \pi]$  represents the phase, and  $\delta(\cdot)$  is Dirac delta function.

The fitted model parameters ( $\sigma, \lambda, \omega$ ) for each keypoint class were averaged across 20 measurement configurations and reported per subject in Table 4.10.

Table 4.10: Model parameters for gesturing use case

Model parameters	Subject	Body parts					
		Head $m = 1$	Left / right side $m = 2 / 3$	Left / right hand $m = 4 / 5$	Legs $m = 6$	Chest $m = 7$	Belly $m = 8$
$\sigma$ (dB·m <sup>2</sup> )	A	-19.17	-23.09	-19.88	-23.80	-19.85	-19.95
	B	-21.32	-17.87	-18.60	-18.85	-19.14	-18.32
	D	-22.88	-19.75	-18.49	-17.37	-20.40	-18.03
	E	-23.23	-16.60	-17.69	-15.46	-22.41	-16.14
$\lambda_{PG}, \omega_{PG}$ (ms <sup>-1</sup> , ms <sup>-1</sup> )	A	62, 63	134, 147	62, 63	71, 73	94, 99	118, 141
	B	98, 154	149, 152	38, 33	77, 102	101, 110	108, 112
	D	130, 160	117, 130	44, 42	89, 98	110, 109	94, 107
	E	99, 101	160, 180	50, 59	51, 66	123, 139	102, 127
$\lambda_T, \omega_T$ (ms <sup>-1</sup> , ms <sup>-1</sup> )	A	132, 139	136, 145	52, 51	98, 71	119, 122	110, 130
	B	110, 139	156, 176	58, 49	90, 111	131, 139	114, 149
	D	147, 176	117, 139	55, 52	113, 148	142, 152	106, 106
	E	130, 150	140, 191	68, 78	120, 160	152, 179	99, 133
$\lambda_{\theta\Lambda}, \omega_{\theta\Lambda}$ (ms <sup>-1</sup> , ms <sup>-1</sup> )	A	85, 86	127, 141	52, 58	110, 112	113, 130	131, 149
	B	116, 152	96, 121	53, 39	97, 78	145, 145	123, 133
	D	113, 155	120, 125	65, 44	73, 115	129, 121	137, 150
	E	117, 143	157, 169	62, 65	53, 81	143, 155	124, 133
$\lambda_{\theta E}, \omega_{\theta E}$ (ms <sup>-1</sup> , ms <sup>-1</sup> )	A	68, 91	132, 149	66, 70	101, 98	123, 139	118, 146
	B	104, 134	102, 130	52, 40	87, 90	133, 154	134, 140
	D	107, 146	135, 145	65, 55	76, 99	133, 164	95, 136
	E	115, 133	131, 181	55, 58	60, 80	149, 166	95, 120

#### 4.2.4.3. Quasi-Deterministic Target Channel Realization

To generate the quasi-deterministic target channel coefficient the following steps, summarized in Figure 4.17, may be followed:

1. Generate the network layout, including Tx, Rx, target keypoint position and subject. The target keypoint position may be defined over time to simulate target motion. Selecting the target subject (A,B,D,E) allows to select the parameters ( $\lambda, \omega$ ) for each keypoint class and the RCS  $\sigma$ .
  - 2a. Calculate the PL for the Tx-target and target-Rx links, for each keypoint, using free space PL (Section 4.2.1).
  - 3a. Calculate delay for each keypoint (Section 4.2.1).
  - 4a. Calculate angle for each keypoint (Section 4.2.1).
  - 2b. Generate offset RCS for each keypoint.
  - 3b. Generate offset delay for each keypoint.
  - 4b. Generate offset azimuth for each keypoint.

5. Draw initial phase

6. Generate  $h_{tg}(t, \tau, \phi_{AOD}, \theta_{ZOD}, \phi_{AOA}, \theta_{ZOA})$

For the points 2b, 3b, and 4b: to generate correlated random variables, several methods can be used. A computational efficient method used in 38.901 to generate correlated random variables is the Sum of Sinusoid model (SOS), relying on a summation of properly weighted sinusoids [13].

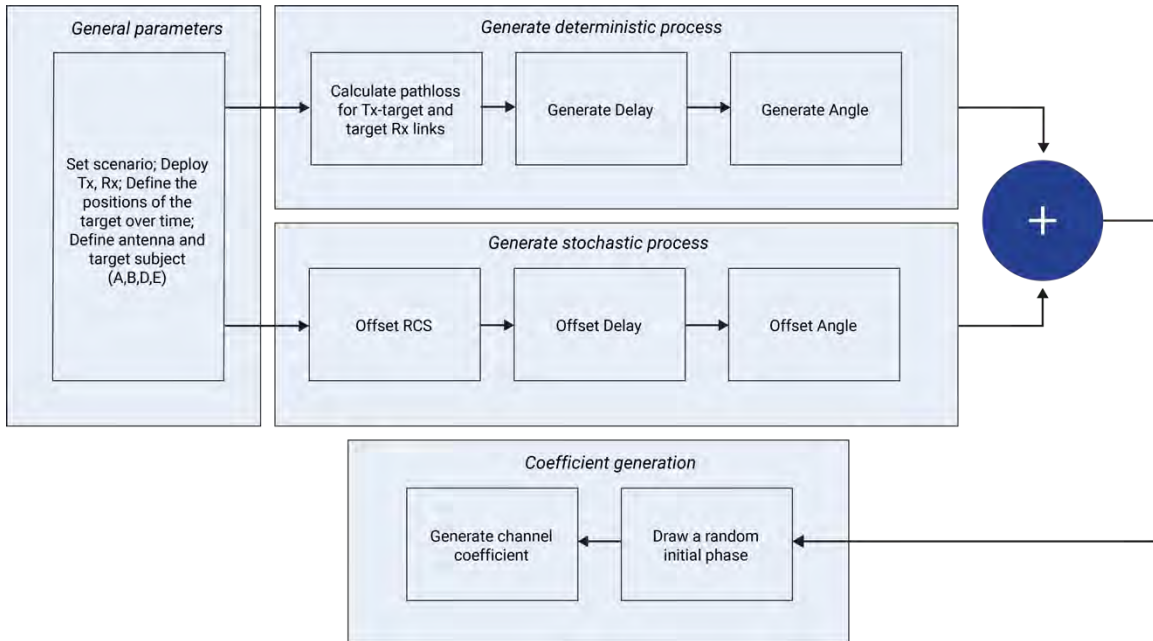


Figure 4.17: Quasi-Deterministic Target-Channel Realization Flowchart

#### 4.2.5. AT&T Target Measurements and RCS Models

In radar technology, RCS is used to quantify the target's scattering behavior. The RCS is a function of the target viewing angle relative to the Tx and Rx antenna and of the frequency and polarization of the incident electromagnetic wave. The RCS is a measure of how much of the incident wave is intercepted by and reflected from the target, as well as how much of that is directed toward the radar Rx. The RCS depends on the size and shape of the target, and the materials from which the target is made on the outer surface, as well as the sensing mode.

RCS is expected to similarly be used to quantify the scattering behavior of the target in the ISAC channel model. For the use cases considered for the ISAC channel model, quantifying the RCS of the vehicles is different from that of a UAV or the pedestrian. For smart transportation, a large vehicle's RCS is different from a small vehicle's RCS.

There are different methods to quantify the RCS, ranging in complexity. The simplest option is to model the RCS as a fixed value depending on the type of the target and use the fixed value in the subsequent channel model pathloss and small-scale fading calculations. The second option is a statistical modelling of the RCS, where the RCS is assumed to be a random variable with a given distribution, accounting for the range of the values that the RCS of the target can take depending on the target viewing or bistatic angle as well as the heading angle, without the complexity of modeling this angle dependency explicitly. Some example distributions used to model the target include Rayleigh, Chi-square, or log-

normal distribution with a given mean and standard deviation that depends on the target's shape and material and its location with respect to the sensing devices. The third option is to quantify the RCS explicitly as a function of the viewing angles to the transmitting and receiving sensing devices, considering the particularities of the shape and the material of the target, by considering, for example, the shape of the target as a combination of simpler shapes with multiple points of reflections. One can then isolate the different sensing regions: monostatic, bistatic, and forward scattering, and quantify the RCS values as a function of the angles. This last option, albeit being the most accurate, is also the most complex. Figure 4.18 shows the Tx heading angle and the bistatic angle between the gNB, the UE, and the sensing target, depending on the sensing mode.

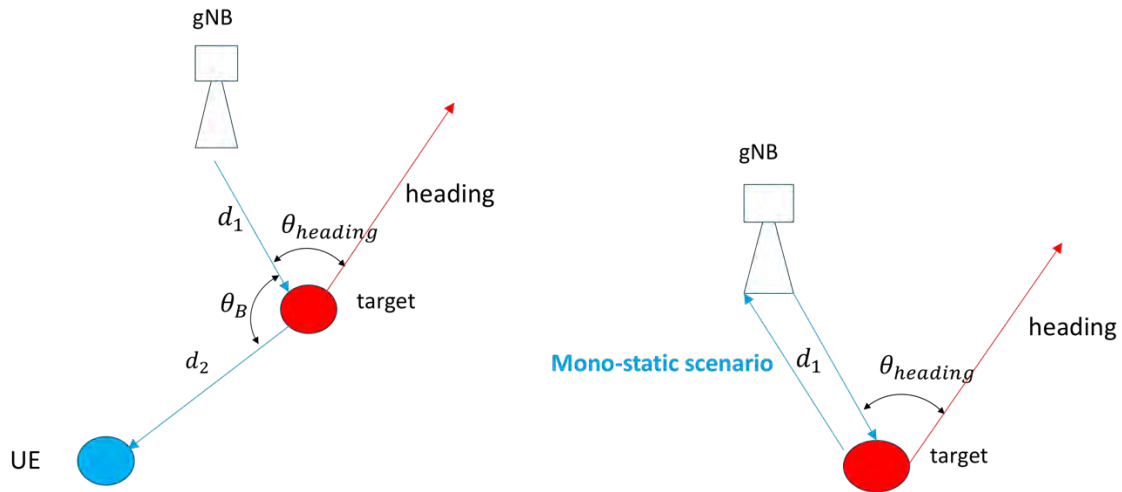


Figure 4.18: Target Scattering Model Geometry

As is well known in the radar community, measured RCS has significant variation vs. bistatic angle  $\theta_B$  and heading angle  $\theta_H$ . Figure 4.19 shows how measured RCS varies for target 1 in the pseudo-monostatic (small  $\theta_B$ ) region vs. heading angle  $\theta_H$  for bistatic based sensing. In general, variations in RCS are highly dependent on target composition and shape. In this case, the box-like structure of the Ford Transit leads to peaks at multiples of  $90^\circ$ .

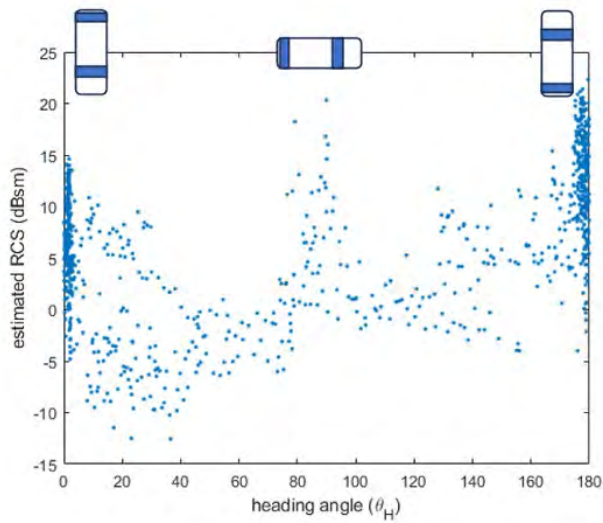


Figure 4.19: Heading angle dependence of RCS for vehicle target in pseudo-monostatic (small  $\theta_B$ ) region. Bright scattering (high RCS) is observed when planar surfaces of vehicle (front, side, rear) are oriented perpendicular Tx pointing direction. The vehicle's rear has more co-planar area than its front, resulting in a higher RCS for  $\theta_H \approx 180^\circ$  vs  $\theta_H \approx 0^\circ$ .

Figure 4.20 depicts how the measured RCS varies as a function of the heading angle in mono-static-based sensing for (a) a vehicle target and (b) a pedestrian target. As the figure shows, there is a very clear distinction on the RCS heading angle dependency depending on the type of target and its material composition.

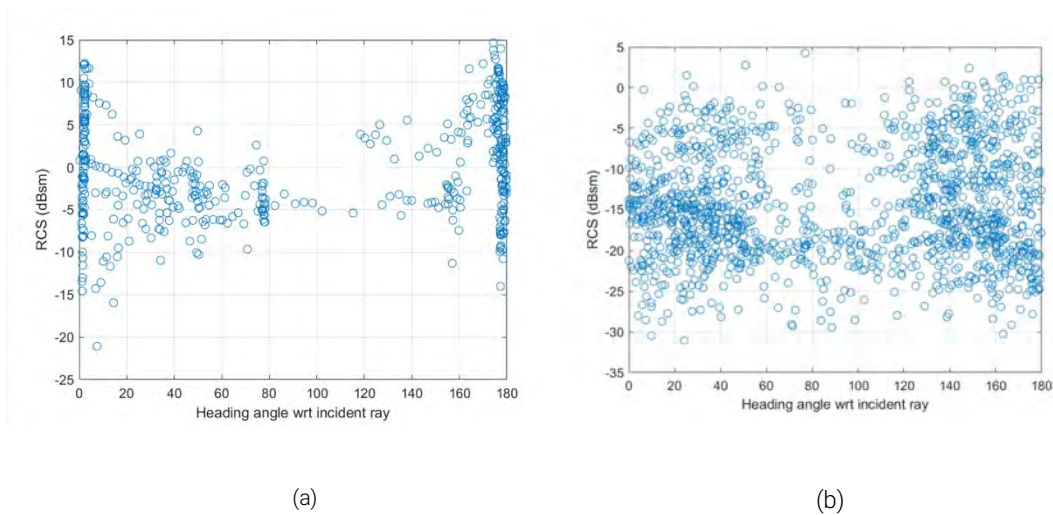


Figure 4.20: Heading Angle Dependence of RCS for (a) a Vehicle Target (b) a Pedestrian Target for Mono-Static Sensing

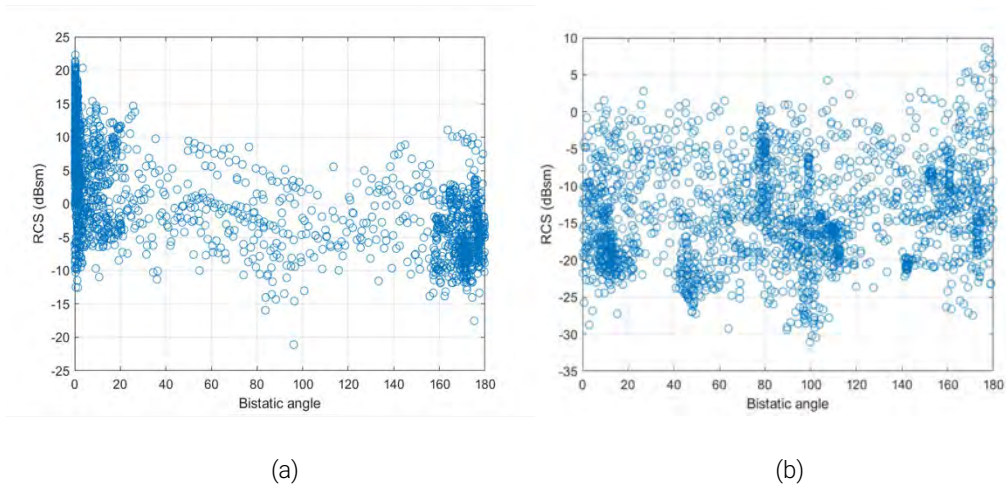


Figure 4.21: RCS Dependence on Bistatic Angle for (a) Vehicle Target, (b) Pedestrian Target

Figure 4.21 shows a snapshot of the RCS for bistatic sensing measurements as a function of bistatic angle  $\theta_B$  for targets 1 and 2, respectively. The difference between the nature and the shape of the target between the vehicle and the pedestrian is noticeable in the distribution of the RCS with respect to the bistatic angle.

Despite these dependencies on the bistatic angle and the heading angle, for a first order modelling of the ISAC channel, modeling RCS should balance accuracy and complexity. For some of the objects and use cases considered, such as object detection and tracking, and for scenarios where these objects are sufficiently far from sensing Tx and sensing Rx, a single point scatter model is sufficient to model the target, with a statistical representation of RCS as a random variable with a mean and variance depending on the target, the sensing mode, and the sensing frequency.

Using large scale fading, and assuming single point scattering, we derive the RCS statistical model as follows. Here, we model target pathloss  $PL_t$  using the following equation:

$$PL_t = PL_1 - G_s + PL_2 \text{ dB}$$

$$G_s = \gamma + 10 \log_{10} \frac{4\pi}{\lambda^2}$$

Where  $\gamma$  is dBm<sup>2</sup> and  $\lambda$  is the wavelength in m. In our model,  $PL_1$  and  $PL_2$  are based on FSPL as a function of  $d_1$  and  $d_2$ , respectively. For monostatic sensing,  $d_1 = d_2$ . Here, we assume UE is within LOS of target. This was enforced during the measurement campaign.

To simplify the model, we propose to model  $\gamma$  as a random variable with conservative values (taken from bistatic region of  $\theta_B$ ). Additional measurements may be necessary to further refine this model.

Using the model described above, we fit  $\gamma$  to a lognormal random variable with parameters shown in Table 4.11 for bistatic sensing, and Table 4.12 for monostatic sensing.

Figure 4.22 shows a good fit to measured data that is less optimistic in pseudo monostatic region (large  $\sqrt{d_1 d_2}$ ).

Table 4.11: Lognormal Parameters for two Target Classes Based on Measurement Data for Bistatic Sensing

Target class	$\mu$ (dBsm)	$\sigma$ (dBsm)
Passenger car	-0.1	6.1
Pedestrian	-14.4	6.7

Table 4.12: Lognormal Parameters for Two Target Classes Based on Measurement Data for Monostatic Sensing

Target class	$\mu$ (dBsm)	$\sigma$ (dBsm)
Passenger car	7.7	8.4
Pedestrian	-6.2	10.0

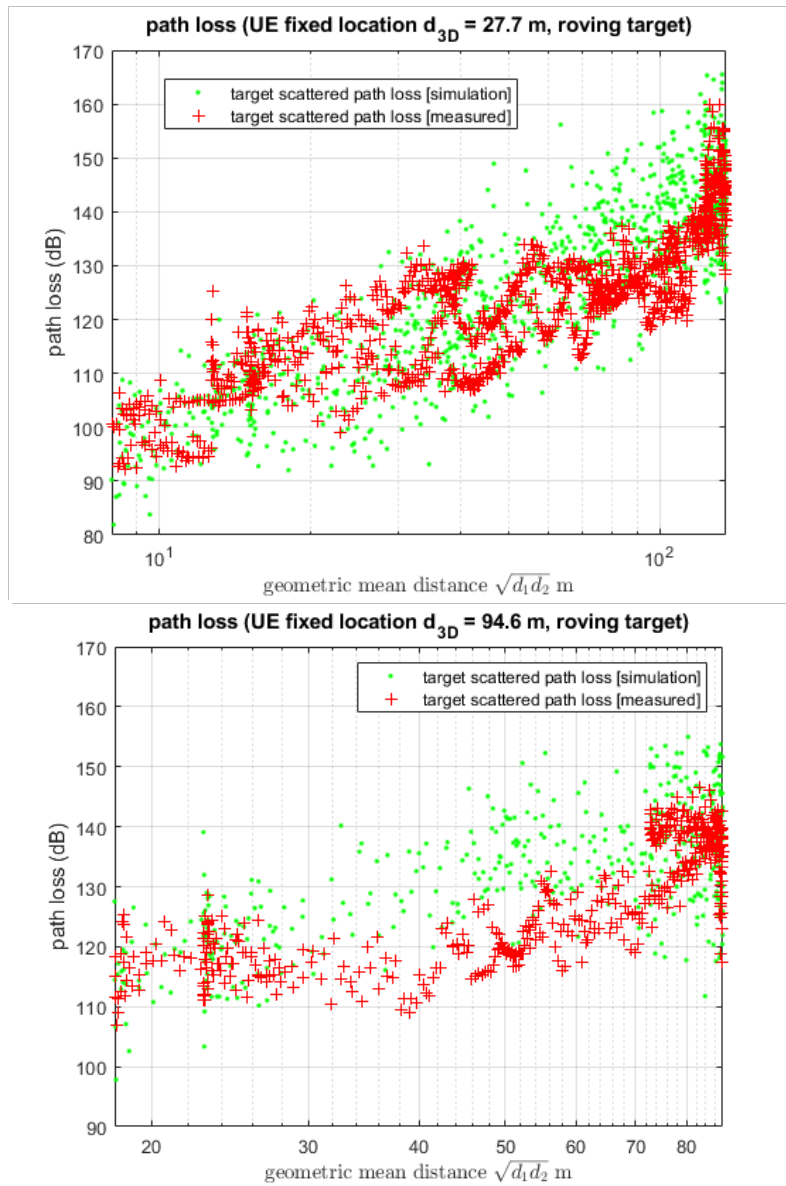


Figure 4.22: Measured Pathloss Components of total PL and Target-Scattered Pathloss  $PL_t$  as a Function of Geometric Mean Distance. Simulated Target-Scattered Pathloss  $PL_t$  is Shown in Green.

### 4.3. Measurement of a Pedestrian Target

Ericsson has undertaken a measurement campaign to investigate Doppler spectrum and radar cross section of a pedestrian moving in a bistatic sensing model. Figure 4.23 shows the geometry of the environment, where the Rx is attached to a building façade, about 15m above ground. In the square in front of the building, a Tx is located on a tripod. A pedestrian walks by the Tx along a straight line. In Figure 4.24, the Rx and Tx are seen along with the pedestrian, who has just passed the Tx and is distancing itself from the Tx. The parameters of the measurement campaign are described in Table 4.13.

Table 4.13: Measurement Parameters

Rx location	15m above ground on a building façade
Tx location	1m above ground on an open square
Carrier frequency	3.8 GHz
Channel sounding interval	20 ms
Bandwidth	100 MHz
Pedestrian speed	Approx. 1.4 m/s

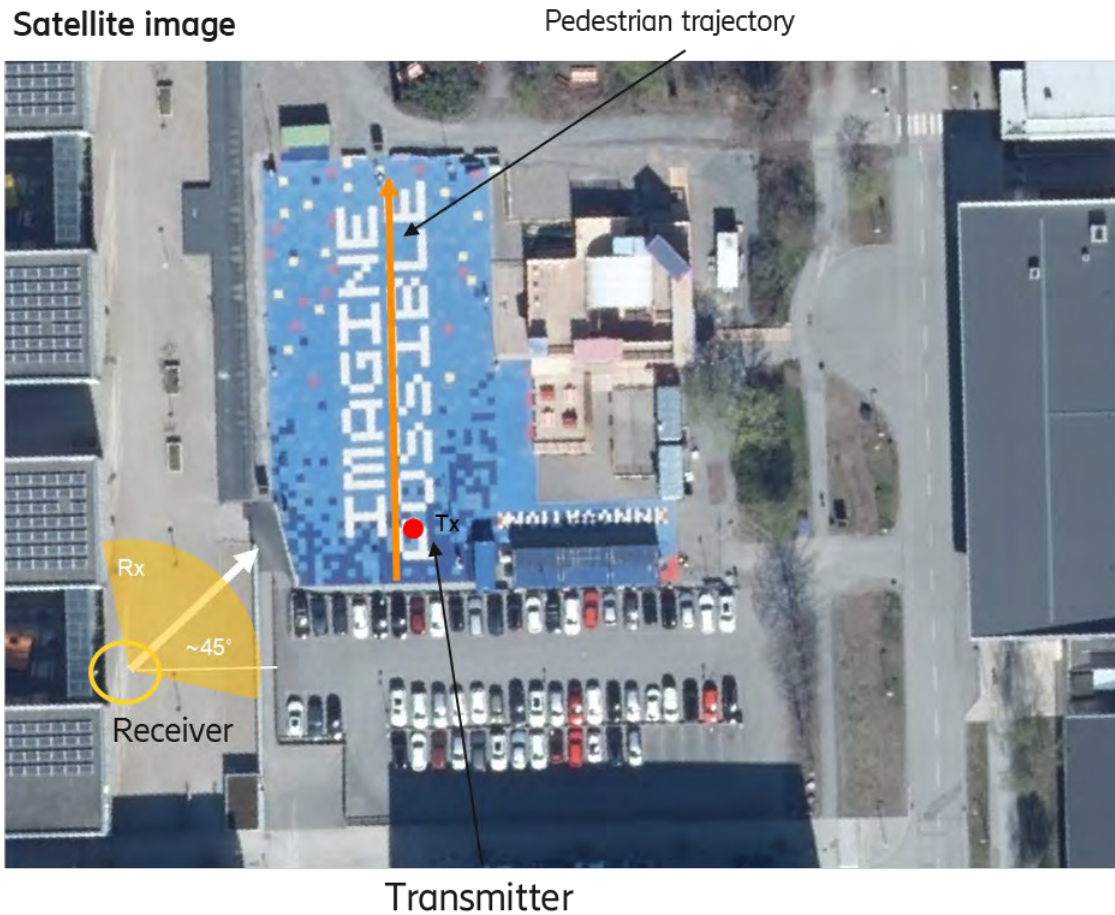


Figure 4.23: Satellite Image of Measurement Scene. The Rx position and orientation is indicated by a yellow fan and arrow. The Tx is marked by a red dot. The trajectory of the pedestrian is shown as an orange line, where the arrowhead indicates the direction of the movement.

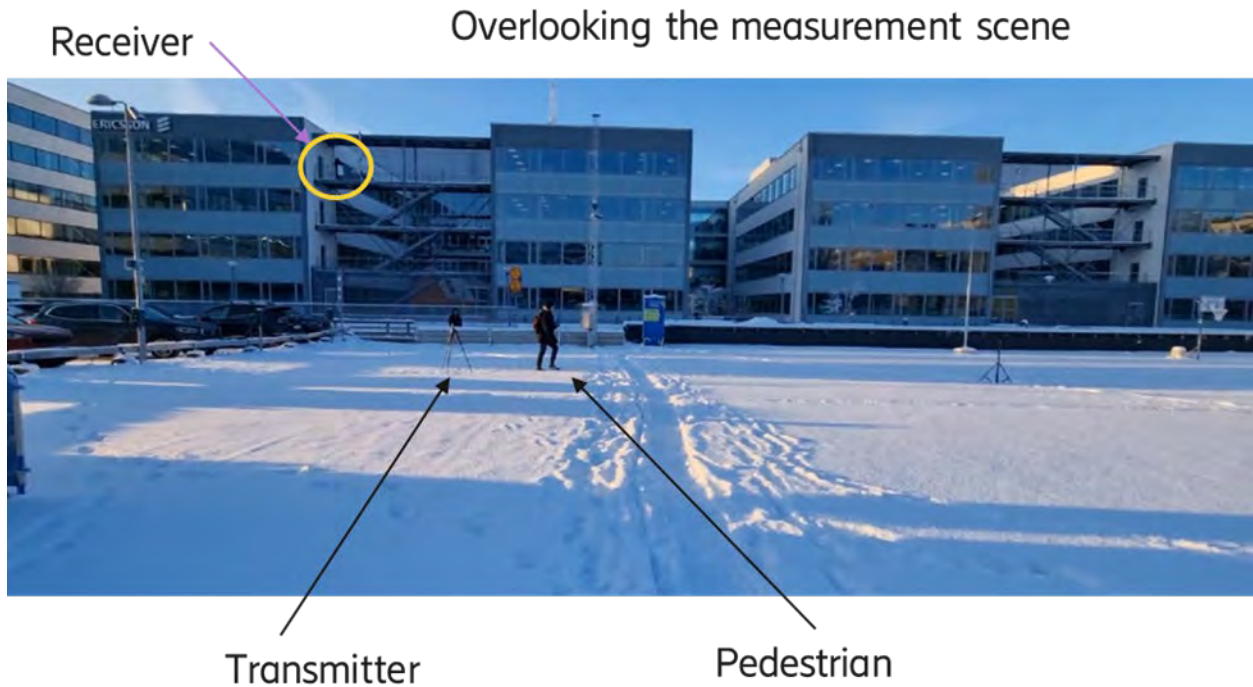


Figure 4.24: Image Overlooking the Measurement Scene. The Rx is seen as a white object mounted on the escape ladder on the building in the background (yellow circle). The Tx is seen on a tripod behind the black pedestrian (yellow arrow).

By computing the Doppler spectrum of the channel estimates, the plot in Figure 4.25 is obtained. The Doppler spectrum was computed by a 0.5-s-long moving window Fourier transform. The colour map is truncated to a dynamic range of 50 dB. Hence, the strong signal with zero Doppler looks wide and the weaker signals with non-zero Doppler are more distinct. The theoretical Doppler shift of a signal reflected off a pedestrian with constant velocity has been calculated and is shown as a white line in the plot.

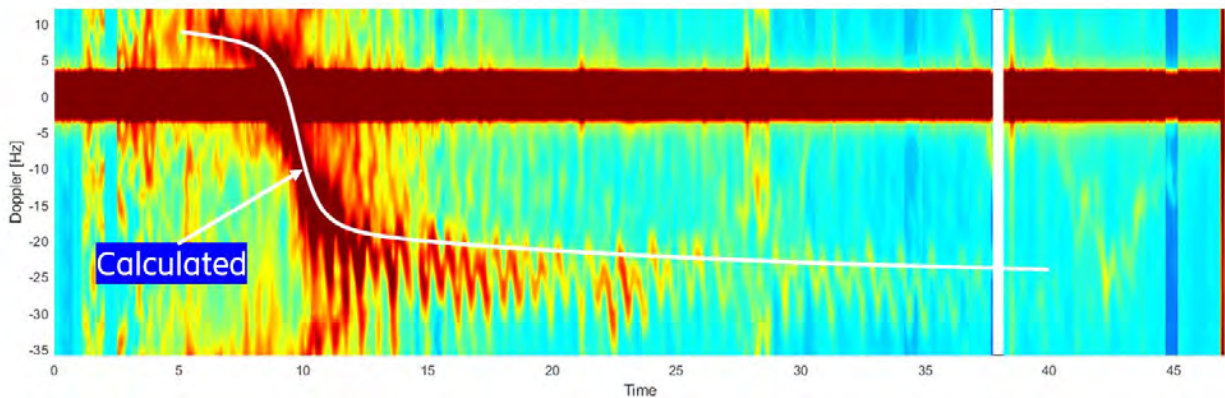


Figure 4.25: The measured Doppler spectrum over time in seconds as the pedestrian walks by the Tx. The white curve shows the calculated Doppler shift of a path scattered off an object with constant velocity moving along the same trajectory as the pedestrian.

The visible trace of peaks with non-zero Doppler in the plot agree to some extent with the calculated curve. The trace of peaks, however, oscillates around the calculated curve onward from around time 10 s. This oscillation has a frequency of approximately 1.6 Hz and an amplitude of approximately 7 Hz, which corresponds to approximately 0.5 m/s. This

oscillation around the mean Doppler can likely be attributed to the fact that the pedestrian is moving with a non-constant velocity that varies with a given frequency around a mean value.

In Figure 4.26, the power received from the two propagation paths is shown. The direct path (between Tx and Rx without the reflections from the pedestrian) has a significantly higher received power than the scattered path reflecting off the pedestrian. The difference in power between the two paths varies between 10 and 50 dB. This orders-of-magnitude difference needs to be modelled properly for the JCAS/ISAC channel. We observe that, for channel modelling for traditional communication systems, propagation paths with power this small are often neglected. For example, TR 38.901 mandates that clusters with a gain 25 dB below the strongest cluster be dropped (see “step 6” in TR 38.901).

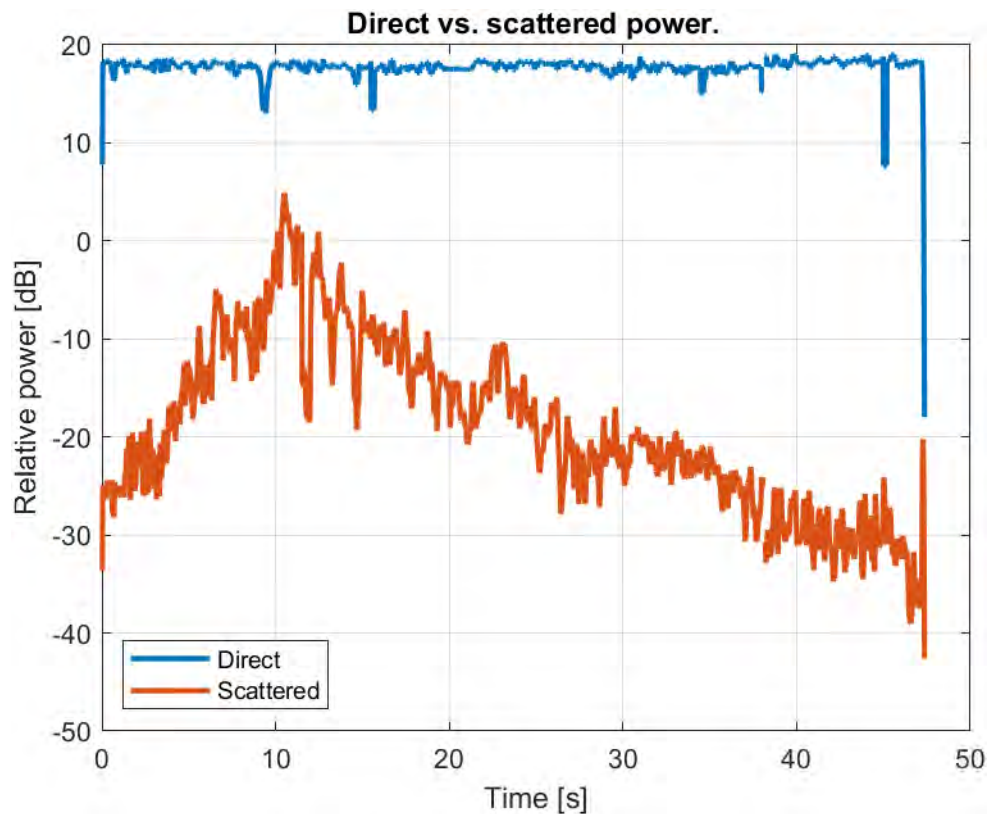


Figure 4.26: Estimated Received Power from the Two Propagation Paths

In Figure 4.27, an estimate of the radar cross-section of the pedestrian is shown. This should be compared to common radar cross-sections of a person. An example is the values shown in [15, Fig. 14.14], where a person is indicated to have a radar cross-section of approximately  $-10$  dBsm to  $0$  dBsm. The radar cross-section is modelled by assuming that the PL of the direct path from Tx to Rx can be modelled as free-space LOS PL, and the PL of the scattered path Tx–pedestrian–Rx can be modelled using the radar equation, and the distances are obtained from measurements on the map in Figure 4.23. The ratio of the two PLs can be read off from Doppler spectra of the kind shown in Figure 4.25. Further assuming that antenna gains are the same for the two propagation paths, a value for the radar cross-section can be computed.

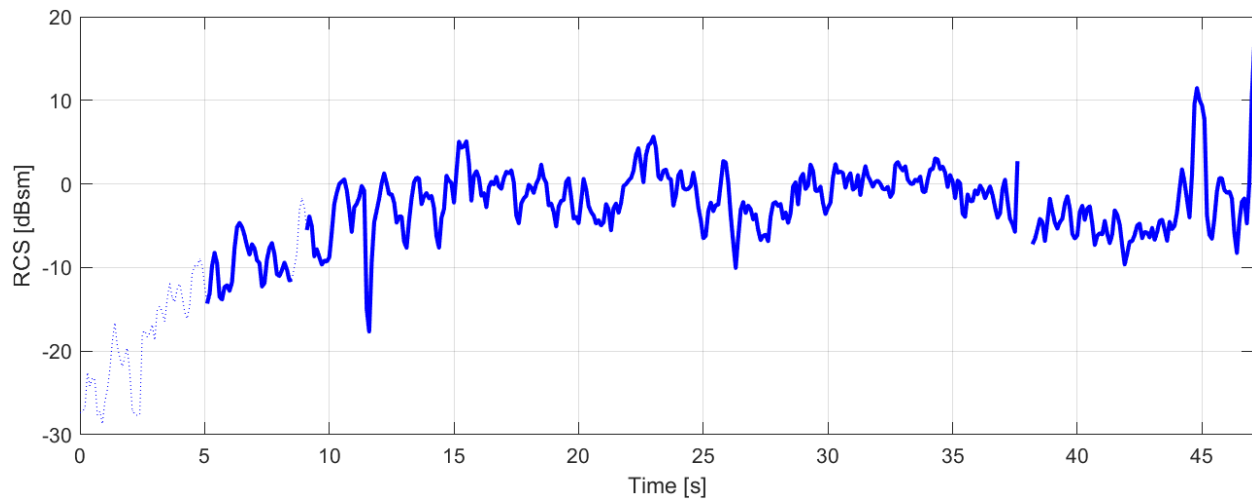


Figure 4.27: Estimated RCS Over Time

It can be seen from Figure 4.27 that the radar cross-section varies with time. The radar cross-section estimate is noisy but seems to vary around a time-varying mean. The small-scale variations of the radar cross section around the mean appear uncorrelated and constrained to within a 5 dB width. The slowly varying mean starts at a low value, increases to around -5 dB at time 5 s, then varies slowly in the interval -5 dB to 0 dB.

The variations in the radar cross-section are, at least partially, explained by the noise and imperfections in the measurement equipment and the assumptions on which the estimate is based. It is also noted that the variations also could be explained if the radar cross-section of the pedestrian is dependent on the incidence and scattering angles, which vary slowly during the measurement when the pedestrian moves. The variations can also be due to the fact that the pedestrian's body changes over time as arms and legs move. Changes in the body would affect characteristics such as the angular fading of the pedestrian.

Figure 4.28 shows the delay-Doppler profile at time 10 s, when the pedestrian has reached the approximate position shown in Figure 4.24. The path lengths are shown relative to the path length of the LOS path. Ignoring the stationary peaks centered around Doppler frequency zero, the remaining peaks can be assumed to stem from propagation paths that have interacted with the moving pedestrian.

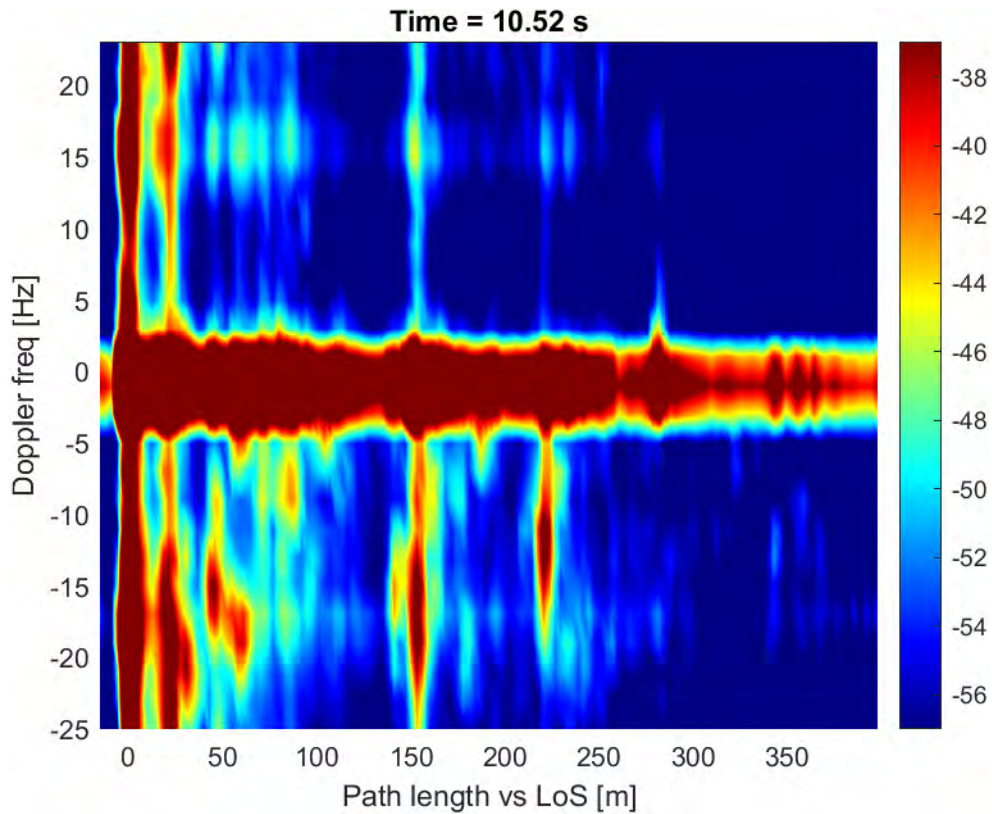


Figure 4.28: Delay-Doppler Profile Where Multiple Reflections of the Target are Visible

Four path lengths have been marked with vertical dashed lines in Figure 4.28. These peaks correspond closely to the path lengths and Doppler shifts of the signal paths shown in Figure 4.29 and Figure 4.30. The first dashed line shows that significant power with non-zero Doppler shift is received at a path length zero to a few meters above the path length of the LOS path. Because the pedestrian at the chosen time is located close to the Tx, the seen power can be an artifact of the directly scattered path: Tx–pedestrian–Rx. The next line at 22m seems to correspond well to the signal path shown in the left picture in Figure 4.30, where the scattered signal reflects off a container before reaching the Rx. The line at 153m corresponds to a signal path, where the scattered signal has reflected off the building in the northeast corner of the map. Finally, the line at 221m seems to correspond to a double-reflection, where the scattered signal is reflected off the wall of the building on which the Rx is attached and then off the wall of the building in the northeast corner of the map.

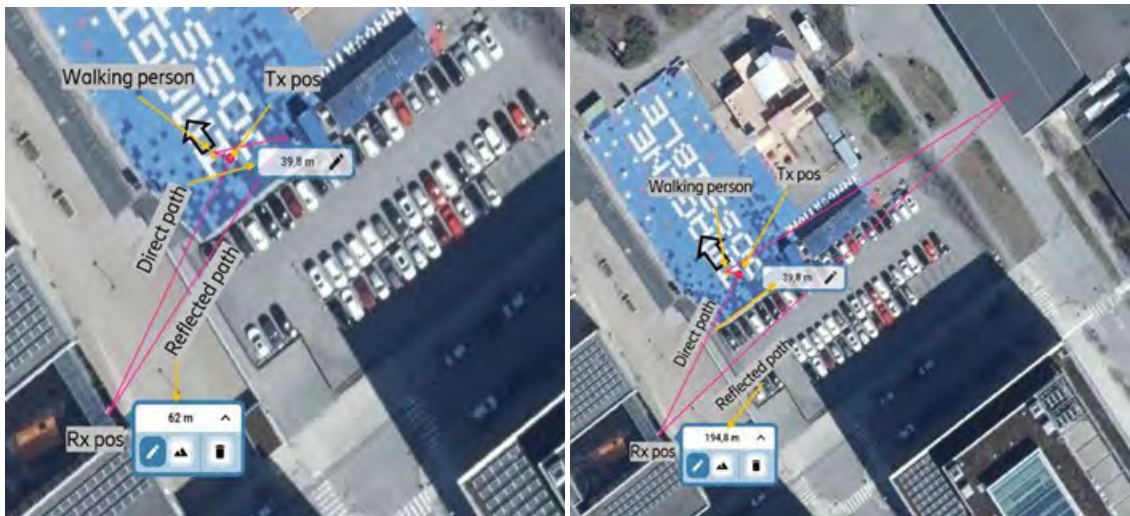


Figure 4.29: Direct path and two single-reflection paths. Left: The shown reflected path bounces on Tx–person–container–Rx. Right: The shown reflected path bounces on Tx–person–wall–Rx

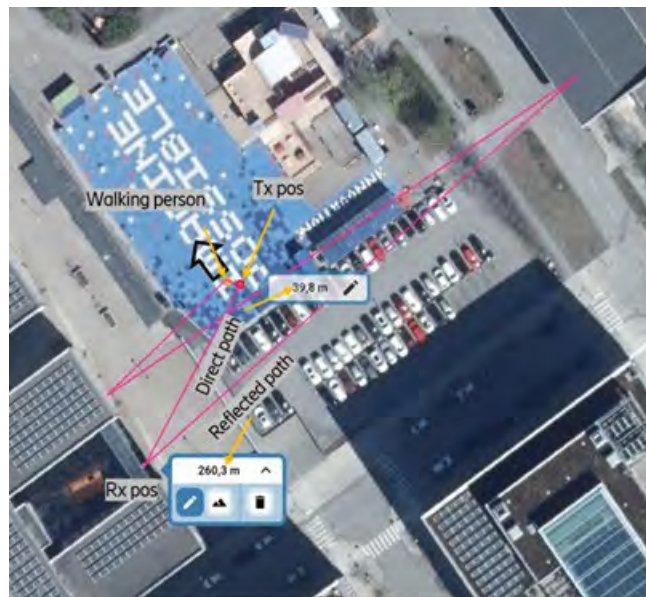


Figure 4.30: An additional double-reflection path is shown: Tx–person–wall1–wall2–Rx

Other secondary peaks with non-zero Doppler shift are also seen in the delay-Doppler profile. These might correspond to reflections from other unidentified walls or objects. We note that the polarization of the channel was not studied in this measurement campaign but should also be evaluated in future studies when measuring the effect of different targets [16].

# 5 BACKGROUND CLUTTER

## 5.1. Indoor Monostatic Background Clutter

### 5.1.1. Environment Definition

We consider clutter backscatter in enclosed indoor environments that range in size from small rooms, such as personal offices, to large, shared spaces, such as a cafeteria. The Tx and Rx are within 1m of each other (thus analogous to monostatic radar), with direct leakage from Tx to Rx sufficiently reduced partly through isolation. The received signal is then dominated by backscatter from the environment, termed “clutter,” such as walls and furnishings, as well as the object of interest, termed “target.” Target modeling was covered in the preceding section, and this section concentrates on backscatter from clutter.

### 5.1.2. Measurement Description

Narrowband measurements of arriving backscatter power as a function of azimuth at 28 GHz were collected in three cities in 251 indoor locations in rooms of different sizes, from 3x3m offices to 20x30m cafeteria. Some rooms had metal furniture and metalized windows, and others with wooden furniture and plain glass windows. The data was collected in three different building types, including office and lab spaces at Nokia Bell Labs in New Jersey, as well as university buildings via collaboration with Columbia University in New York City, and Pontificia Universidad Católica de Valparaíso and Universidad Técnica Federico Santa María in Chile. Room materials varied, with some containing metal furniture along the walls, and others with primarily wood furniture and drywall walls. We measured 81, 128, and 42 small, medium, and large office locations, with distances to nearest illuminated wall of under 2.5, 3-5 m, and greater than 5 m, respectively. Collected data allowed formulation of a model for indoor backscatter validated through a statistically significant data set.

The radar measurement set-up was adopted from a narrowband channel sounder [20]. The Tx emitted a 28 GHz CW tone at 22 dBm from an omnidirectional antenna. The Rx is a 10° (24 dBi) horn, mounted on a rotating platform allowing a full angular scan every 200 ms. The Rx records power samples at a rate of 740 samples/sec. using an onboard computer. The omnidirectional transmit antenna was placed on a lower shelf of a plastic cart (shown in Figure 5.1) to illuminate the surrounding area uniformly in all azimuthal directions. The spinning horn was placed on an upper shelf of the cart, about 0.7m above the lower shelf. Multiple layers of absorbing foam, separated with aluminum foil, attenuated the direct Tx-Rx signal path. This monostatic radar arrangement was calibrated by measuring backscattered power from a standard trihedral target with known [24]RCS in an anechoic chamber. Measured backscattered power was within 1.4 dB of prediction by the standard monostatic radar equation [19]at range R:

$$P_{\text{target}} = \frac{\lambda^2 \sigma_{\text{back}} P_T G_T G_R}{(4\pi)^3 R^4} \quad (5.1)$$

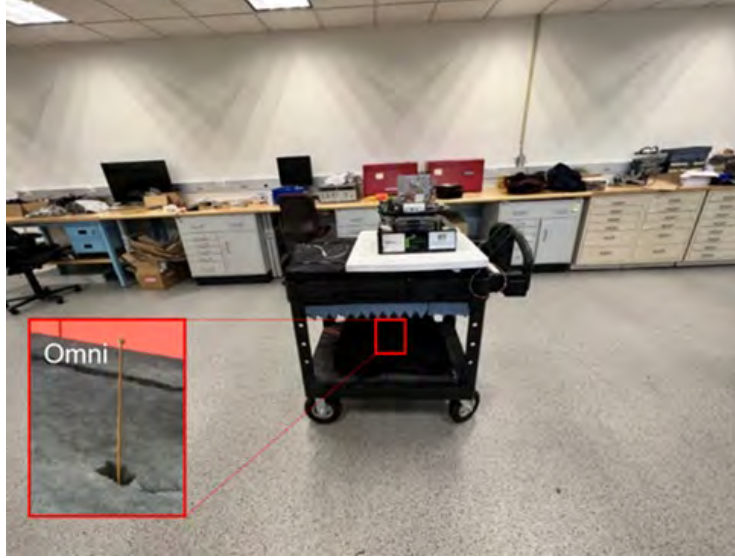


Figure 5.1: 28 GHz narrowband backscatter radar arrangement, with omnidirectional Tx antenna on lower cart shelf illuminating the scene and a spinning horn Rx collecting backscatter power vs. azimuth on top cart shelf.

### 5.1.3. Average Backscattered Power

Typical measured backscatter azimuth spectrum is shown in Figure 5.2. A general observation is that backscattered power ratio of received power to transmit power:

$$P_{\text{back}}(\phi) = \frac{P_{\text{clut}}(\phi)}{P_{\text{T}}} \quad (5.2)$$

in any direction  $\phi$  may be characterized statistically by variation around an average value over azimuth:

$$\langle P_{\text{back}} \rangle_{\phi} = \frac{\langle P_{\text{clut}} \rangle_{\phi}}{P_{\text{T}}} \quad (5.3)$$

indicated as a dashed circle in Figure 5.2. The observed average backscatter value varied from location to location, with cumulative distributions, grouped by room size, plotted in Figure 5.3. For display clarity, Figure 5.3 shows a representative set of 73 links collected in rooms with metal furniture and/or metalized windows. Both transmit and receive antenna heights were no more than 1m above the floor, thus primarily having metal cabinets in view in such rooms, seen in Figure 5.1. The average backscatter power is observed to decrease as the room size increases.

In these measurements, the radar transceiver is placed near center of a room, with clutter consisting of walls and furniture near them.

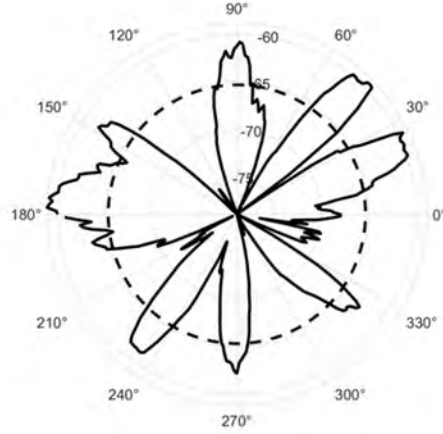


Figure 5.2: Sample Measured Backscattered Power Ratio vs. Azimuth. Dashed line is the average backscattered power ratio.

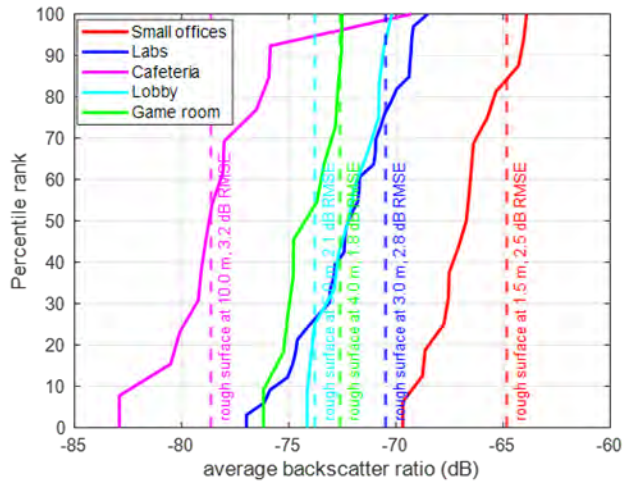


Figure 5.3: Distributions of Measured Locally Averaged Backscatter Power Ratios in Rooms of Different Sizes. Dashed vertical lines are predictions by (5.4), with distance to wall as indicated.

Average backscattered power ratio is modeled in terms of environment quantities alone:

$$\langle P_{\text{back}} \rangle = \frac{\langle P_{\text{clut}} \rangle_{\phi}}{P_{\text{T}}} = |\Gamma_{\text{wall}}|^2 \left( \frac{\lambda}{4\pi d_s} \right)^2 \quad (5.4)$$

where  $|\Gamma_{\text{wall}}|^2$  is the ordinary Fresnel reflection coefficient and  $d_s$  is the distance from transceiver to nearest illuminated wall.

Average backscatter ratio predicted by  $d_s$  is evaluated for different room sizes and compared against measurements in Figure 5.3. Rooms with steel furniture dominating the field of view of antennas (as in Figure 5.1), and metalized

windows, were assigned in  $|\Gamma_{\text{wall}}|^2 = 1$ , while rooms with wooden furniture were assigned  $|\Gamma_{\text{wall}}|^2 = 0.25$ ,

corresponding to the power reflection coefficient from air-dielectric interface with relative dielectric constant of 3 [25] (representative of dry wall/wood), averaged over a uniform distribution of incidence angles over 0-90°. Distance to clutter  $d_s$  was set to distance to nearest wall used in measurements, typically  $d_s$  is one half the smallest dimension of the room. Prediction with formula (5.4) is indicated by vertical lines in Figure 5.3 corresponding to various room sizes. Room dimensions and measured backscatter power for all data sets is tabulated in Table 5.1 along with RMS error and is found to predict measured average backscatter ratio with 4.0 dB RMS error. This is notable, considering the medians of the observed distributions span some 12 dB and with sole parameters being distance  $d_s$  to nearest illuminated wall and material-dependent reflection coefficient  $|\Gamma_{\text{wall}}|^2$  of 1 or 0.25, for metal/dielectric surroundings, respectively.

Table 5.1: Backscatter Power Ratio in Different Size Rooms. Measured and Predicted by (5.4), at Distance  $d_s$  to Nearest Wall

Data Set	# of links	Room dimensions	$d_s$ (m)	Measured median average backscatter ratio (dB)	Model RMS error (dB)
8 offices, metal furniture	16	3m×3m	1.5	-66.7	2.5
7 Labs, metal furniture	33	20m×6m	3.0	-72.1	2.8
Cafeteria, metalized windows, counters	13	30m×20m	10.0	-78.6	3.2
Lobby, metalized windows	12	30m×20m	5.0	-72.1	2.1
Game room, metalized windows	11	25m×15m	4.0	-73.7	1.8
Conference Room	26	7m×5m	2.5	-72.6	3.2
Gym	17	30m×17m	9.0	-78.7	5.4
Lab 1	15	15m×5m	2.5	-71.1	4.7
Lab 2	10	15m×5m	2.5	-71.1	4.3
Office 1	22	3.5m×2.7m	1.0	-69.3	2.4
Office 2	17	4m×3m	1.5	-71.8	2.7
Study hall	22	15m×9m	4.5	-71.7	7.7
Café	15	14m×10m	3.0	-71.4	5.2
Carleton Hall	22	25m×12m	3.0	-74.8	2.2
<b>Overall</b>	<b>251</b>				<b>4.0</b>

#### 5.1.4. Observed Azimuth Variation Statistics

Measured backscattered power exhibits variation with azimuth around its local average, as illustrated in Figure 5.2. The distribution of observed power variations is plotted as a solid line in Figure 5.4.

Spatial variation of observed azimuth spectra was examined in a lab, with locations along a 1-m-long line segment every 10 cm, for a total of 11 azimuthal spectra. Correlation coefficient of azimuthal spectra was computed for different separations using measured spectra  $P(\phi, d_n)$  at locations  $d_n$  as:

$$\rho(d_2 - d_1) = \langle p(\phi, d_2) p(\phi, d_1) \rangle,$$

$$p(\phi, d_n) \equiv \frac{P(\phi, d_n) - \langle P(\phi, d_n) \rangle}{\left( \langle (P(\phi, d_n) - \langle P(\phi, d_n) \rangle)^2 \rangle \right)^{1/2}}, \quad n = 1, 2 \quad (5.5)$$

Correlation coefficient  $\rho(d_2 - d_1)$  computed from data is plotted in Figure 5.5 as a function of location separation  $|d_2 - d_1|$ . The correlation coefficient is seen to drop to about 0.3 for location separation as small as 0.1 m, indicating rapid variation in azimuthal spectra even with small displacement, consistent with a rich multipath environment.

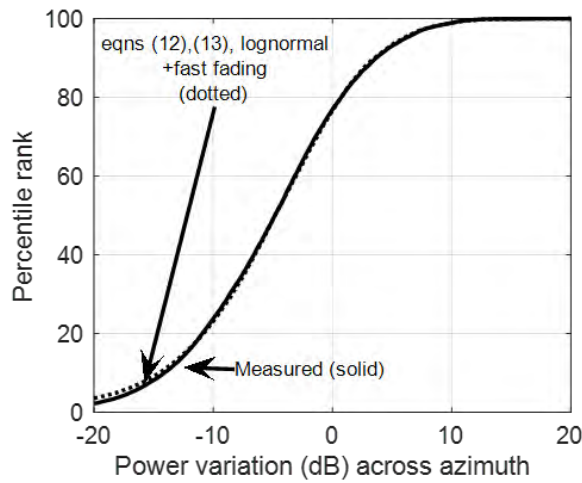


Figure 5.4: Cumulative distribution of azimuthal variation of measured backscattered power ratio around average predicted power (5.4), using a  $10^\circ$  receive antenna. Dotted line is distribution of predictions using (5.8) with (5.7).

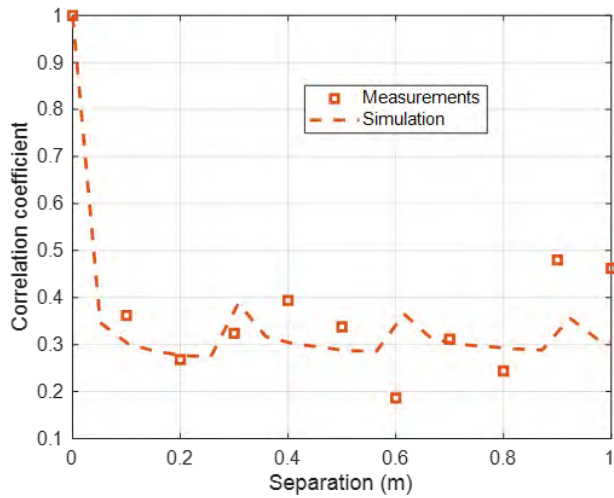


Figure 5.5: Correlation of azimuthal spectra (5.5) at locations at different separations: Measured values are squares, dashed line is simulation evaluating (5.5) using predicted spectra (5.8) with (5.7).

Autocorrelation of azimuth spectra was computed from measured azimuth spectra, normalized as in (5.5):

$$\rho(\phi_2 - \phi_1) = \langle p(\phi_1) p(\phi_2) \rangle, \quad (5.6)$$

The averaging in (5.6) is over all measured locations. The autocorrelation (5.6) is plotted in

Figure 5.6 as a function of azimuth shift  $\phi_2 - \phi_1$ , superimposed on the similar computation using the antenna azimuth pattern (dashed) measured in an anechoic chamber. The main lobe of measured autocorrelation of backscattered azimuth spectra in clutter is nearly identical to that in anechoic chamber. This indicates that the correlation of backscatter in azimuth scale is much narrower than the antenna beamwidth.

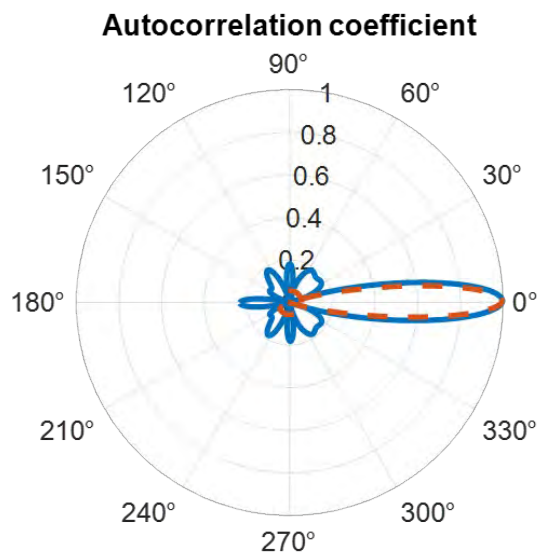


Figure 5.6: Autocorrelation of azimuthal spectra measured in a room (solid) and of antenna azimuth pattern (dashed) measured in a chamber.

### 5.1.5. Clutter Backscatter Model

Measurements described above are used to define a model for the monostatic arrangement, with backscattered plane waves arriving at radar location  $\mathbf{r}$  from azimuth  $\phi$  with complex amplitude  $h_{\text{chan}}(\mathbf{r}, \phi)$  given by:

$$\begin{aligned}
 h_{\text{chan}}(\mathbf{r}, \phi) &= \sqrt{P_0(d_s)} \sqrt{10^{P_v/10}} \sqrt{10^{P(\phi)/10}} e^{i\phi} e^{i2\mathbf{k}\cdot\mathbf{r}}, \\
 P_0(d_s) &= |\Gamma_{\text{wall}}|^2 \left( \frac{\lambda}{4\pi d_s} \right)^2, \quad \text{Average backscatter power} \\
 P_v &\sim N(\mu_v, \sigma_v), \quad \sigma_v = 4.0 \text{ dB}, \quad \mu_v = -10 \log_{10} e^{(0.1 * \ln(10) * \sigma_v)^2 / 2} \\
 P(\phi) &\sim N(\mu, \sigma), \quad \sigma = 7.0 \text{ dB}, \quad \mu = -10 \log_{10} e^{(0.1 * \ln(10) * \sigma)^2 / 2}, \text{ i.i.d.} \\
 \langle P(\phi_1) P(\phi_2) \rangle &= e^{-\phi^2 / 2\phi_{\text{rms}}^2}, \quad \phi_{\text{rms}} = 1^\circ \\
 \phi &\sim U(0, 2\pi), \quad \mathbf{k} = (k \cos \phi, k \sin \phi) \quad \text{small-scale fading}
 \end{aligned} \tag{5.7}$$

The above model includes theoretical formula (5.4) for average backscatter  $P_0(d_s)$  at distance  $d_s$  to clutter, its variation  $P_v$  (dB), azimuthal power variation  $P(\phi)$  (dB) relative to local average and small-scale fading expected in scattering environments, represented by plane wave arrivals each with random phase  $\phi$  and spatial variation  $e^{i2\mathbf{k}\cdot\mathbf{r}}$ , with a factor of 2 accounting for 2-way phase delay between transceiver and extended clutter. The random phase for each plane wave arrival is necessary to emulate small scale spatial fading, while the factor  $e^{i2\mathbf{k}\cdot\mathbf{r}}$  allows for spatially consistent channel response should one move the monostatic radar station or add another antenna in close proximity. The random azimuthal spectra  $P(\phi)$  in (5.7) are modeled as having Gaussian form correlation  $\langle P(\phi_1) P(\phi_2) \rangle = e^{-\phi^2 / 2\phi_{\text{rms}}^2}$ , with characteristic scale  $\phi_{\text{rms}} = 1^\circ$ .

A direct way to simulate a correlated Gaussian process is to convolve a white Gaussian process with a corresponding filter. Normal distributions (in dB)  $P_v$  and  $P(\phi)$  are characterized by corresponding standard deviations  $\sigma_v$  and  $\sigma$ , determined from observed distributions. Their mean values,  $\mu_v = -10 \log_{10} e^{(0.1 * \ln(10) * \sigma_v)^2 / 2}$ ,  $\mu = -10 \log_{10} e^{(0.1 * \ln(10) * \sigma)^2 / 2}$ , correspondingly, follow to enforce  $\langle 10^{P_v/10} \rangle = \langle 10^{P(\phi)/10} \rangle = 1$ , since these are deviations from local average power.

Backscattered signal received by a transceiver with transmit and receive antennas aimed in directions  $\phi_T$  and  $\phi_R$ , respectively are obtained by integrating arrival spectrum (5.7) over all angles, weighted by the product of transmit and receive antenna field patterns  $f_T(\phi)$  and  $f_R(\phi)$ :

$$y_R(\mathbf{r}, \phi_R, \phi_T) = \sqrt{P_T} \int_0^{2\pi} d\phi h_{\text{chan}}(\mathbf{r}, \phi) f_R(\phi - \phi_R) f_T(\phi - \phi_T) \tag{5.8}$$

Relative transceiver location  $\mathbf{r}$  is relevant only if channels at multiple nearby (within  $\sim 1$  m) transceiver locations are considered. The antenna patterns are normalized for unit total power:

$$\int_{-\pi}^{\pi} d\phi |f_R(\phi)|^2 = \int_{-\pi}^{\pi} d\phi |f_T(\phi)|^2 = 1 \tag{5.9}$$

Patterns obtained by spinning directional antenna are then used for evaluations of (5.8) at different angles  $\phi_R, \phi_T$ , which constitutes a circular convolution of the channel response with antenna field patterns. The result is illustrated in Figure 5.7, showing sample measured patterns on the left and sample simulated patterns on the right.

Azimuthal variation of the angular spectra generated using (5.7) and (5.8) is found to be within 1 dB of the observed distribution of backscatter power variation, as shown in Figure 5.4.

Azimuthal spectrum correlation (5.5) of simulated spinning antenna responses (5.8), plotted in Figure 5.5 as a function of antenna separation, is seen to correspond well with observed spectrum correlations. Autocorrelation of the simulated spectra closely corresponds to the measured result, with main lobe width within 1 degree of measurements.

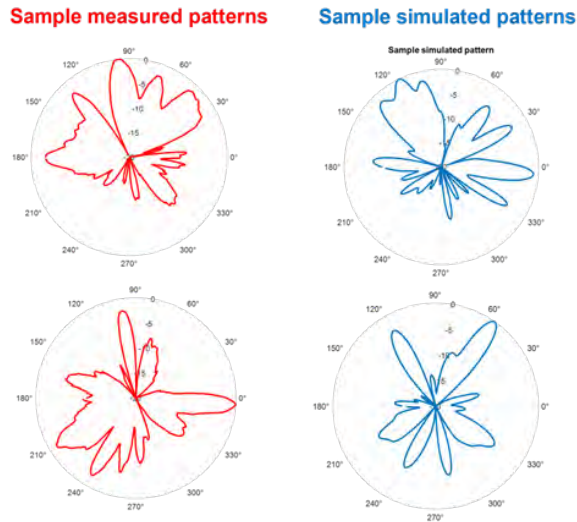


Figure 5.7: Sample Backscatter Power Ratios vs. Azimuth: Measured are on Left, Simulated Using (5.8) On Right

### 5.1.6. Delay-Azimuth Clutter Backscatter Model

The clutter backscatter model presented in Section 5.1.5 is now extended to include backscattered power distribution in delay, as well.

Distribution of power in the channel as a function of delay has been modeled in [22][23] as a superposition of the direct arrival and a reverberant power distributed over delay. In monostatic radar, the direct arrival (termed Tx/Rx leakage) is not of interest and effort is made to diminish its impact, usually through a combination of Tx/Rx isolation and time-gating. The reverberant power delay profile is represented in [23] as having an average delay envelope as decaying exponentially, with a close correspondence to measurements, including the simple version of the Saleh-Valenzuela model [26]:

$$P_d(\tau) = e^{-(\tau - 2d_s/c)/T_{rev}} u(\tau - 2d_s/c), \quad (5.10)$$

Where  $u(\tau - 2d_s/c)$  is the step function and peak power is set to unity. The characteristic time  $T_{rev}$  is related [23] to room volume  $V$ , total wall area  $S$ , and wall absorption coefficient, with a representative value  $T_{rev} = 10^{-8}$  sec. The

reverberation power sequence is taken as starting at  $\tau = 2d_s / c$ , with  $2d_s$  round-trip distance to nearest illuminated wall, typically half the room size.

Joint distribution of power in azimuth and delay can be generated by combining (5.7) and (5.10), for a single transceiver (thus relative  $r=0$ ):

$$\begin{aligned}
 h_{\text{chan}}(\tau, \phi) &= \sqrt{P_0(\tau, d_s)} \sqrt{10^{P_v/10}} \sqrt{10^{P(\tau, \phi)/10}} e^{i\varphi}, \\
 P_0(\tau, d_s) &= |\Gamma_{\text{wall}}|^2 \left( \frac{\lambda}{4\pi d_s} \right)^2 e^{-(\tau - 2d_s/c)/T_{\text{rev}}} u(\tau - 2d_s/c) \\
 P_v &\sim N(\mu_v, \sigma_v), \quad \sigma_v = 4.0 \text{ dB}, \quad \mu_v = -10 \log_{10} e^{(0.1 * \ln(10) * \sigma_v)^2 / 2} \\
 P(\tau, \phi) &\sim N(\mu, \sigma), \quad \sigma = 7.0 \text{ dB}, \quad \mu = -10 \log_{10} e^{(0.1 * \ln(10) * \sigma)^2 / 2}, \text{ i.i.d.} \\
 \langle P(\phi_1) P(\phi_2) \rangle &= e^{-\phi^2 / 2\phi_{\text{rms}}^2}, \quad \phi_{\text{rms}} = 1^\circ \\
 \varphi &\sim U(0, 2\pi), \text{ random phase for small-scale fading}
 \end{aligned} \tag{5.11}$$

Here the random distribution of backscattered arrivals in delay and azimuth is described as a lognormally distributed “clutter map”  $P(\tau, \phi)$ .

The channel response to a probing waveform  $x(t)$  of bandwidth  $B$ , using transmit and receive antenna field patterns  $f_T(\phi)$  and  $f_R(\phi)$  is obtained by convolving in angle channel impulse response (5.11) with corresponding antenna patterns as in (5.8), as well as convolving in delay with probing waveform  $x(t)$ , normalized to unit total power:

$$\int_0^\infty |x(t)|^2 dt = 1 \tag{5.12}$$

The resulting power delay profile instantiation is shown in Figure 5.8, where the channel response (5.11) was convolved with a Hamming window 1 ns duration, here corresponding to  $1/BW$ .

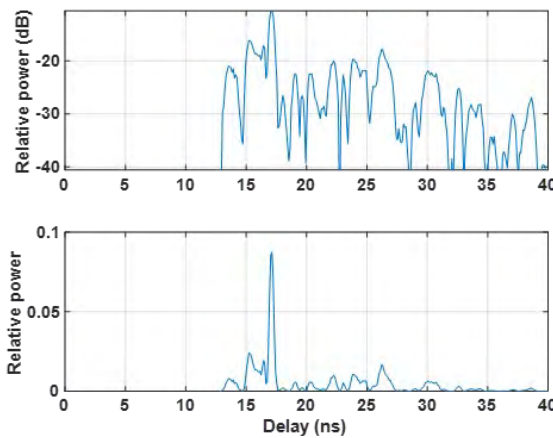


Figure 5.8: Sample backscatter power delay profiles for 1 GHz bandwidth, with relative power in dB (top) and in linear units (below)

The corresponding power distribution in azimuth and delay, obtained for 1 GHz bandwidth,  $10^\circ$  receive antenna, and omnidirectional transmit antenna is illustrated in Figure 5.9. Strong arrivals appear as bright spots, usually at shorter delays, with power decaying exponentially with delay, as prescribed by (5.10) and (5.11). Key parameters, as described above, include room dimensions, dominant materials (metal or dielectric), observed standard deviation of backscatter variabilities  $\sigma_v$  and  $\sigma$ , and reverberation time  $T_{rev}$ . The statistical model does not require a detailed room layout description, aiming to reproduce backscatter clutter statistics, as opposed to a deterministic response.

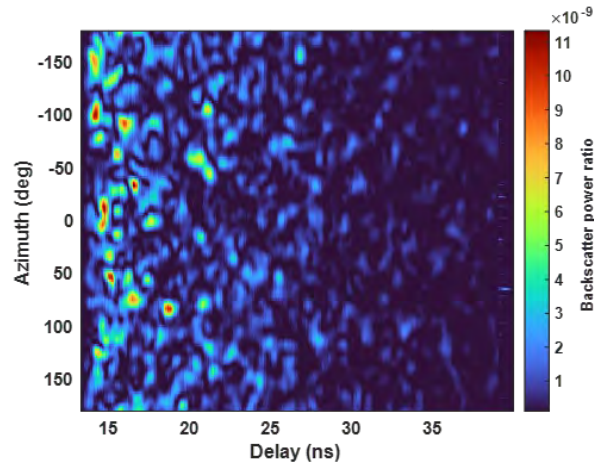


Figure 5.9: Sample backscatter power vs. azimuth and delay, for 1 GHz bandwidth,  $10^\circ$  receive antenna, and omnidirectional transmit antenna.

## 5.2. Other Environments and Sensing Arrangements

Channel models for other environments and sensing arrangements (bistatic/monostatic) is to be addressed in future studies. These include:

- > Bi-static indoor clutter. The bi-static clutter link is equivalent to the usual communication channel link. Thus ordinary models such as 3GPP TR 38.901 indoor model are expected to apply.

# 6 SENSING CHANNEL MODEL ENHANCEMENTS

## 6.1. Sensing Target Models

Target models were developed and described in Section 4 to enable simulation of target-scattered signals. Scattered power is given by the radar equation. Target RCS is described statistically, with parameters extracted from measurements for human and vehicle targets. Additional parameters such as target delay and angle spreads were also deduced from measurements to allow high-resolution simulation needed for target behavior characterization, such as human gesture recognition.

### 6.1.1. Option 1 – Single-Point Single-Ray Model

A single-ray model target is a simple model of target scattered signal, needed for target detection/tracking. The target signal is modeled as being a single arrival, characterized by power, azimuth and elevation angle, and delay. For a bi-static case, the target angles from rx and Rx are specified. Both for monostatic and bi-static cases, the target angle and delay given by simple Tx-target-Rx geometry and power given a stochastic process with RCS are extracted from measurements. Either lognormal or gamma distributions are used for RCS, with RCS fluctuation simulated by a temporal correlation deduced from expected (micro) Doppler spectrum.

### 6.1.2. Option 2 – Single-Point Multiple-Ray Model

An enhanced target model is developed suitable when the radar sensor has high resolution, allowing it to resolve a target as having more than a single time/AoA. The target model here is composed of multiple rays, whose delays and angles are defined statistically, based on measurements, relative to simple geometric target coordinates. The resulting target model thus has angle and delay spread.

### 6.1.3. Option 3 – Multiple-Point Model

An even more elaborate target model is developed, describing different target parts (human limbs) as moving in particular trajectories, whose characteristics are derived from measurements, to allow simulation of signals as needed for applications such as gesture recognition, sports monitoring, etc.

## 6.2. Sensing Environment Models

Option 1 – Statistical model for clutter backscatter is developed for monostatic sensing indoors to allow simulation of target detection, localization, and characterization in the presence of clutter. Clutter model allows generation of clutter backscatter as a “clutter map” in an angle-delay plane, with power described statistically using a lognormal distribution, with parameters deduced from measurements.

# 7 CONCLUSIONS

Communication channel behavior in the 7-24 GHz band is examined based on new measurements to assess accuracy of existing standard propagation models. Based on measurements in factories and outside courtyards conducted by Keysight and Anritsu in the current report, it is found that the measured channels (indoor factory and short range outdoor, <100 m) are consistent with the 3GPP 38.901 propagation model recommendations. Thus change might not be called for these channels. Conclusions about other channel models are pending more measurements from member companies.

Sensing channel models are developed to allow simulation of detection and characterization of target signals in the presence of clutter. Target types include humans, vehicles, drones, and robot arms. Clutter backscatter model is developed for indoor monostatic sensing.

# 8 ABBREVIATIONS AND ACRONYMS

ACF	Autocorrelation Function
AMR	Autonomous Mobile Robot
AoA	Angle of Arrival
AoD	Angle of Departure
AGV	Automated Guided Vehicle
BS	Base Station
BW	Beam Width
CDF	Cumulative Distribution Function
CIR	Channel Impulse Responses
CW	Continuous Wave
DDHC	Data Driven Hybrid Channel
EIRP	Effective Isotropic Radiated Power
FLPt	Floating Intercept
FSPL	Free Space Path Loss
GPS	Global Positioning System
gNB	gNodeB
HPBW	Half Power Beam Width
IF	Intermediate Frequency
InF	Indoor Factory
ISAC	Integrated Sensing and Communication
JCAS	Joint Communication and Sensing
LoS	Line-of-Sight
LSP	Large-Scale Parameter
METIS	Mobile and Wireless Communications Enablers for the Twenty-Two Information Society
MiWEBA	Millimetre-Wave Evolution for Backhaul and Access
NIST	National Institute of Standards and Technology
NLOS	Non-Line-of-Sight
OFDM	Orthogonal Frequency-Division Multiplexing
PL	Pathloss
PLE	Path Loss Exponent
PN	Pseudorandom
RAN	Radio Access Network
RCS	Radar Cross-Section
RF	Radio Frequency

# 8 ABBREVIATIONS AND ACRONYMS

RMS.....	Root Mean Square
ROACH.....	Realtime Omnidirectional Array Channel
RT.....	Ray Tracing
Rx.....	Receiver
SC.....	Spatial Consistency
SCM.....	Spatial Channel Model
SLAM.....	Simultaneous Localization and Mapping
SOS.....	Sum of Sinusoid
SSP.....	Small-Scale Parameter
Tx.....	Transmitter
UCA.....	Uniform Circular Array
UE.....	User Equipment
USRP.....	Universal Software Radio Peripheral
VAA.....	Virtual Antenna Arrays
VNA.....	Vector Network Analyzer
VSA.....	Vector Signal Analysis
WLAN.....	Wireless Local Area Networks
XPR.....	Cross-Polarization Ratio
ZoA.....	Zenith Angle of Arrival
ZoD.....	Zenith Angle of Departure

# 9 REFERENCES

1. 3GPP SA1 TR 22.837 v100. "Feasibility Study on Integrated Sensing and Communication (Release 19)".
2. 3GPP TR. 38.901. (March 2022). "Study on channel model for frequencies from 0.5 to 100 GHz, V17.0.0".
3. A. Bodi, S. Blandino, N. Varshney, J. Zhang, T. Ropitault, M. Lecci, P. Testolina, J. Wang, C. Lai and C. Gentile. (2022). "NIST Quasi-Deterministic (Q-D) Channel Realization Software Documentation". *National Institute of Standards and Technology*. <https://www.nist.gov/services-resources/software/quasi-deterministic-channel-realization-software>.
4. E. Egea-Lopez, J. M. Molina-Garcia-Pardo and P. Degauque. (2021). "Opal: An open source ray-tracing propagation simulator for electromagnetic characterization". <https://journals.plos.org/plosone/article?id=10.1371/journal.pone.0260060>.
5. CloudRT. <http://cn.raytracer.cloud:9090/>
6. M. Zhang et al. (August 2021). "Channel models for WLAN sensing systems", IEEE 802.11-21/0782r3. <https://mentor.ieee.org/802.11/dcn/21/11-21-0782-03-00bf-channelmodels-for-wlan-sensing-systems.docx>
7. A. Kasher, Y. Sun. (2020). "WiFi-Sensing-Use-Cases" IEEE Std. IEEE 802.11-20-1712-02.
8. W. G. Newhall, and J. H. Reed. (2002). "A geometric air-to-ground radio channel model". MILCOM 2002. Proceedings. Vol. 1. IEEE.
9. R. Boulic, N. M. Thalmann, and D. Thalmann. (1990). "A global human walking model with real-time kinematic personification". *The visual computer*, vol. 6, pp. 344–358.
10. D. Lu et al. (2023). "CAROM Air-Vehicle Localization and Traffic Scene Reconstruction from Aerial Videos." *2023 IEEE International Conference on Robotics and Automation (ICRA)*, London, United Kingdom, pp. 10666-10673.
11. G. Zewu, Y. Zhang, D. Lu, and T. Wu. (2022). "Vision-Based Quadruped Pose Estimation and Gait Parameter Extraction Method". *Electronics* 11, no. 22: 3702.
12. J. Lambrecht, L. Kästner, J. Guhl and J. Krüger. (2021). "Towards commissioning, resilience and added value of Augmented Reality in robotics: Overcoming technical obstacles to industrial applicability". *Robotics and Computer-Integrated Manufacturing* 71: 102178.
13. J. Chang, R. Caromi, J. Senic, S. Berweger, N. Varshney, J. Wang, C. Lai, A. Bodi, W. Sloane, C. Gentile, and N. Golmie. (Feb 2024). "Quasi-Deterministic Channel Propagation Model for Human Sensing: Gesture Recognition Use Case," *IEEE Open Journal on Antennas and Propagation*.
14. A. Bayesteh et al. (2022). "Integrated sensing and communication (ISAC)—From concept to practice". *Communications of Huawei Research*: 4-25.
15. Skolnik, M. (2008). "Radar Handbook". Third Edition, McGraw Hill.
16. Ericsson. R1-2400530. (February 2024). "Discussion on ISAC Channel Modelling". Ericsson, 3GPP RAN1#116.

17. NGA. (May 2024). "NGA Vision for 6G". *3GPP Stage 1 Workshop on IMT 2030 Use Cases*. [http://www.3gpp.org/ftp/workshop/2024-05-08\\_3GPP\\_Stage1\\_IMT2030\\_UC\\_WS/Docs/SWS-240017.zip](http://www.3gpp.org/ftp/workshop/2024-05-08_3GPP_Stage1_IMT2030_UC_WS/Docs/SWS-240017.zip).
18. D. Chizhik et al. (October 2022). "Directional Measurements and Propagation Models at 28 GHz for Reliable Factory Coverage". *IEEE Transactions on Antennas and Propagation*, vol. 70, no. 10, pp. 9596-9606.
19. G. T. Ruck, D. E. Barrick, W. D. Stuart, C. K. Krichbaum, Radar Cross Section Handbook. Volumes 1 & 2, Plenum Press, January 1, 1970.
20. D. Chizhik, J. Du, R. Feick, M. Rodriguez, G. Castro, and R. A. Valenzuela. (Jun. 2020). "Path loss and directional gain measurements at 28 GHz for non-line-of-sight coverage of indoors with corridors". *IEEE Trans. Antennas Propag.*, vol. 68, no. 6, pp. 4820–4830.
21. N. Yamada, Y. Tanaka and K. Nishikawa. (2005). "Radar cross section for pedestrian in 76GHz band". *2005 European Microwave Conference*, Paris, France.
22. J. B. Andersen, J. O. Nielsen, G. F. Pedersen, G. Bauch and J. M. Herdin. (April 2007). "Room electromagnetics". *IEEE Antennas and Propagation Magazine*, vol. 49, no. 2, pp. 27-33
23. Steinböck, G., Pedersen, T., Fleury, B. H., Wang, W., & Raulefs, R. (May 2015). "Experimental Validation of the Reverberation Effect in Room Electromagnetics". *IEEE Trans. on Antennas and Propagation*, vol. 63, no. 5, pp. 2041-205.
24. Eravant. "Trihedral Corner Reflector". <https://www.eravant.com/2-4-edge-length-trihedral-corner-reflector>.
25. S. S. Zhekov, O. Franek and G. F. Pedersen. (Feb. 2020). "Dielectric Properties of Common Building Materials for Ultrawideband Propagation Studies". *IEEE Antennas and Propagation Magazine*, vol. 62, no. 1, pp. 72-81.
26. A. A. M. Saleh and R. Valenzuela. (February 1987). "A Statistical Model for Indoor Multipath Propagation". *IEEE Journal on Selected Areas in Communications*, vol. 5, no. 2, pp. 128-137.
27. L. Liu et al. (December 2012). "The COST 2100 MIMO channel model". *IEEE Wireless Communications*, vol. 19, no. 6, pp. 92-99.
28. NGA. (2023). "6G Roadmap for Vertical Industries". [https://www.nextgalliance.org/white\\_papers/6g-roadmap-vertical-industries/](https://www.nextgalliance.org/white_papers/6g-roadmap-vertical-industries/)
29. NGA. (2023). "Distributed Sensing and Communications". [https://nextgalliance.org/white\\_papers/distributed-sensing-and-communications/](https://nextgalliance.org/white_papers/distributed-sensing-and-communications/)
30. NGA. (2023). "6G Spectrum Considerations". [https://www.nextgalliance.org/white\\_papers/6g-spectrum-considerations/](https://www.nextgalliance.org/white_papers/6g-spectrum-considerations/).
31. V. Erceg et al. (July 1999). "An empirically based path loss model for wireless channels in suburban environments". *IEEE Journal on Selected Areas in Communications*, vol. 17, no. 7, pp. 1205-1211.

# NEXT G ALLIANCE REPORTS



Next G Alliance Report: 6G Technologies



Next G Alliance Report: 6G Applications and Use Cases



Next G Alliance Report: Roadmap to 6G



Green G: The Path Toward Sustainable 6G



6G Market Development: A North American Perspective



Next G Alliance Report: AI-Native Wireless Networks



Next G Alliance Report: Sustainable 6G Connectivity – A Powerful Means of Doing Good



Next G Alliance Report: 6G Distributed Cloud and Communications System



Next G Alliance Report: Trust, Security, and Resilience for 6G Systems



Next G Alliance Report: Digital World Experiences



Next G Alliance Report: Cost-Efficient Solutions



Next G Alliance Report: 6G Radio Technology Part I: Basic Radio Technologies



Next G Alliance Report: 6G Radio Technology Part II: Basic Radio Technologies



Next G Alliance Report: 6G Technologies for Wide-Area Cloud Evolution



6G Market Management and Orchestration



Next G Alliance Report: Beyond Speed: Promoting Social and Economic Opportunities through 6G and Beyond



Next G Alliance Report: 6G Roadmap for Vertical Industries



Next G Alliance Report: 6G Spectrum Considerations



Next G Alliance Report: Terminology for Frequency Ranges



Next G Alliance Report: Distributed Sensing and Communications



Next G Alliance Report: Network-Enabled Robotic and Autonomous Systems



Next G Alliance Report: Multi-Sensory Extended Reality (XR) in 6G



Next G Alliance Report: Shaping Tomorrow: The Evolution of Personalized Digital Experiences Through 6G Technologies



Next G Alliance Report: Evolution of Sustainability Indicators for Next-Generation Radio Network Technologies



Next G Alliance Report: 6G Sustainability KPI North American 6G Roadmap Priorities



Next G Alliance Report: 6G Sustainability KPI Assessment Introduction and Gap Analysis

COPYRIGHT  
AND  
DISCLAIMER

Published July 2024

Copyright © 2024 by Alliance for Telecommunications Industry Solutions

All rights reserved.

Alliance for Telecommunications Industry Solutions  
1200 G Street, NW, Suite 500  
Washington, DC 20005

No part of this publication may be reproduced in any form, in an electronic retrieval system or otherwise, without the prior written permission of the publisher. For information, contact ATIS at (202) 628-6380. ATIS is online at <http://www.atis.org>.

The information provided in this document is directed solely to professionals who have the appropriate degree of experience to understand and interpret its contents in accordance with generally accepted engineering or other professional standards and applicable regulations. No recommendation as to products or vendors is made or should be implied.

NO REPRESENTATION OR WARRANTY IS MADE THAT THE INFORMATION IS TECHNICALLY ACCURATE OR SUFFICIENT OR CONFORMS TO ANY STATUTE, GOVERNMENTAL RULE OR REGULATION, AND FURTHER, NO REPRESENTATION OR WARRANTY IS MADE OF MERCHANTABILITY OR FITNESS FOR ANY PARTICULAR PURPOSE OR AGAINST INFRINGEMENT OF INTELLECTUAL PROPERTY RIGHTS. ATIS SHALL NOT BE LIABLE, BEYOND THE AMOUNT OF ANY SUM RECEIVED IN PAYMENT BY ATIS FOR THIS DOCUMENT, AND IN NO EVENT SHALL ATIS BE LIABLE FOR LOST PROFITS OR OTHER INCIDENTAL OR CONSEQUENTIAL DAMAGES. ATIS EXPRESSLY ADVISES THAT ANY AND ALL USE OF OR RELIANCE UPON THE INFORMATION PROVIDED IN THIS DOCUMENT IS AT THE RISK OF THE USER.

NOTE - The user's attention is called to the possibility that compliance with this document may require use of an invention covered by patent rights. By publication of this document, no position is taken with respect to whether use of an invention covered by patent rights will be required, and if any such use is required no position is taken regarding the validity of this claim or any patent rights in connection therewith. Please refer to [www.atis.org/legal/patentinfo.asp](http://www.atis.org/legal/patentinfo.asp) to determine if any statement has been filed by a patent holder indicating a willingness to grant a license either without compensation or on reasonable and non-discriminatory terms and conditions to applicants desiring to obtain a license.

Building the foundation for  
North American leadership in  
6G and beyond.

[nextgalliance.org](https://nextgalliance.org)

